UC Irvine

UC Irvine Electronic Theses and Dissertations

Title

Field Enhancement and Helicity Maximization of Structured Light for Chirality Detection and SERS Applications

Permalink

https://escholarship.org/uc/item/8n1280qm

Author

Hanifeh, Mina

Publication Date

2021

Peer reviewed|Thesis/dissertation

eScholarship.org Powered by the California Digital Library
University of California

UNIVERSITY OF CALIFORNIA,
IRVINE

Field Enhancement and Helicity Maximization of Structured Light for Chirality Detection and SERS Applications

DISSERTATION

submitted in partial satisfaction of the requirements
for the degree of

DOCTOR OF PHILOSOPHY

in Electrical and Computer Engineering

by

Mina Hanifeh

Dissertation Committee:
Professor Filippo Capolino, Chair
Professor Eric Potma
Professor Regina Ragan

2021

Chapter 2 © ACS Photonics
Chapter 3 © Phyical Review B, ACS Photonics, and Proc. SPIE
Chapter 4 © ACS Photonics
Chapter 5 © Journal of Applied Physics
All other materials © 2021 Mina Hanifeh

DEDICATION

To my heroes, Mom and Dad

TABLE OF CONTENTS

Page

LIST OF FIGURES **v**

ACKNOWLEDGMENTS **xi**

VITA **xii**

ABSTRACT OF THE DISSERTATION **xiii**

1 Introduction **1**

2 Light-Matter Interaction **15**
2.1 Some Mechanical Properties of Electromagnetic Fields 16
2.2 Chiral Light-Matter Interaction 19
2.3 Helicity Maximization and Physical Significance of Optimally Chiral Fields 21

3 Optimally Chiral Electromagnetic Fields **28**
3.1 Gaussian Beams with Circular Polarization 29
3.2 Azimuthally Radially Polarized Beam 30
3.3 Optimally Chiral Nearfield 36
3.3.1 Dielectric NA Illuminated by an Optimally Chiral Field 39
3.3.2 Dielectric Nanoantenna under GB Illumination 43
3.3.3 Dielectric Nanoantenna under an ARPB Illumination 46
3.4 Conclusion 51

4 Chirality Characterization at Nanoscale **58**
4.1 Feasibility of the Proposed Platform for Chirality Characterization 63
4.2 Conclusion 71

5 Helicity Maximization in a Planar Array of Achiral High-density Dielectric Nanoparticles **74**
5.1 Helicity Analysis of Nearfield of a High-density Dielectric NA 75
5.1.1 Optimally Chiral Nearfield of an Array Element 79
5.2 Optimally Chiral Nearfield of a Planar Array of NAs 83
5.2.1 Helicity Density of an Array of NAs Illuminated by a Plane Wave with Circular Polarization 89

5.2.2 Effect of a Substrate on Helicity Density Generated by an Array of Si NA 93
5.3 conclusion 98

6 Rayleigh Anomaly in Surface Enhanced Raman Spectroscopy 101
6.1 Rayleigh Anomaly in an Array of Plasmonic Rods 102
6.2 Field Enhancement in an Assembly of gold NPs and Plamnonic Array of Rods 108
6.3 Conclusion 109

Appendix A Polarizabilities of a Chiral Spherical Particle 115

Appendix B Field Enhancement in an Array of Plasmonic Rods 119

LIST OF FIGURES

Page

1.1 Chiral spiral shape of a snail's shell and chiral orientation of petals in a flower. 3
1.2 The transmitted powers of right and left handed circularly polarized plane waves (RCP and LCP) through a chiral medium reveals its chirality parameter κ. 4

2.1 The general concept of helicity maximization. The red solid circle represents fields with constant energy density u_0, whereas the dashed and dotted lines represent fields with three constant helicity densities. The black solid straight line represents fields with $|h| = u/\omega$, that also defines maximum helicity density at a given energy density u_0. 23

3.1 (a) Electric field magnitude in the $x-z$ plane and, (b) propagation of the electric field vector along the z-direction for a Gaussian beam with circular polarization and $w_0 = \lambda$ propagating along the z direction. Helicity density h of the GB on the $z = 0$ transverse plane when (c) $w_0 = 2\lambda$, and (d) $w_0 = \lambda$, normalized to that of a GB with the same power and $w_0 = 3\lambda$. Note that the helicity density at the center of the coordinate system of the beam with $w_0 = \lambda$ is approximately four times stronger than that of the beam with $w_0 = 2\lambda$, confirming that the helicity density is enhanced when the beam parameter w_0 decreases i.e., for tighter focused beams. The quantity for circularly polarized GB with (e) $w_0 = 3\lambda$ and (f) $w_0 = 0.65\lambda$. 31
3.2 An optimally chiral ARPB with total power of 1 mW, beam parameter $w_0 = \lambda$, and amplitudes $V_{\mathrm{A}} = \pm iV_{\mathrm{R}}$ propagating along z direction, at wavelength $\lambda = 680$nm: (a) Three-dimensional plot of electric field's magnitude $\left|\mathbf{E}^{\mathrm{ARPB}}\right|$ in $x-y$ and $y-z$ planes. (b) Magnitudes of longitudinal and tangential components of electric and magnetic fields at the minimum waist plane $z = 0$. (c) Real part of the electric field vector represented by cones at various $z =$ constant planes. The results are obtained via FEM full-wave numerical analysis. 35
3.3 Nearfield of a NA is used to generate enhanced helicity density with respect to that of an incident beam. (a) An optical beam propagating along the $+z$ direction illuminates a NA located at the center of the coordinate system. (b) The dielectric NA is modeled by induced electric and magnetic dipole moments $\mathbf{p}_{\mathrm{NA}}$ and $\mathbf{m}_{\mathrm{NA}}$, respectively, and their scattered nearfields demonstrate high helicity density in the vicinity of the NA. 36

3.4 The polarizabilities of a spherical NA made of Si approximately satisfy the balance relation $\alpha_{\rm ee}^{\rm NA} = \epsilon_0 \alpha_{\rm mm}^{\rm NA}$. (a) Plot of the logarithm of $\left|\alpha_{\rm ee}^{\rm NA} - \epsilon_0 \alpha_{\rm mm}^{\rm NA}\right|$ (normalized to its maximum) which takes negative large value, around -2, where the balance relation $\alpha_{\rm ee}^{\rm NA} = \epsilon_0 \alpha_{\rm mm}^{\rm NA}$ is approximately satisfied, versus radius a of the NA and wavelength of the excitation field λ. (b) Magnitudes of and phase difference between electric and magnetic polarizabilities of a NA with radius $a = 78$ nm versus wavelength λ. The refractive index of Si is obtained from Ref. [22] and the polarizabilities are calculated using the Mie scattering coefficients [23]. 42

3.5 The scattering helicity enhancement distribution in the (a) $x - y$ plane, and (b) $y - z$ plane, around a Si NA with radius $a = 78$nm at the wavelength $\lambda = 680$nm. 45

3.6 Enhancement of (a) helicity and (b) energy densities of the scattered field on the surface of a Si NA, evaluated along the $+z$ direction, i.e., at $\mathbf{r} = a\hat{\mathbf{z}}$, when illuminated by an optimally chiral ARPB propagating along the positive z direction with beam's half-waist parameter $w_0 = \lambda$. They are normalized with respect to the analogous densities of the incident ARPB evaluated at the origin. The very bright region represents the area where scattered helicity density is 11 times larger than that of the incident ARPB beam at its axis. Helicity and energy enhancements occur in regions close to each other. Interference (c) and total (d) helicity densities, both normalized to that of the incident APRB beam, evaluated at $\mathbf{r} = a\hat{\mathbf{z}}$. The maximum of total helicity density enhancement $|h/h_{\rm inc}^{\rm o}|$ is approximately 20. The plots also show that the interference helicity density $|h_{\rm int}|$ in Eq.3.13 has a considerable contribution to the total helicity enhancement. That is why it is important that the interference term has the same sign of the scattered and incident helicities. 48

3.7 Radius of the dielectric NA that guarantees the maximum enhancement of energy density $u_{\rm max}$, maximum helicity density $h_{\rm max}$, and the "optimal chirality" condition $|h| = u/\omega$ to be satisfied, versus free space wavelength λ. In all cases the power of the incident field is kept constant. Note that for a chosen operating wavelength, the maximum of helicity enhancement, energy enhancement, and the condition $\alpha_{\rm ee}^{\rm NA} = \epsilon_0 \alpha_{\rm mm}^{\rm NA}$ (for optimal nearfield chirality) occur at different radii of the dielectric NA. Maximum helicity enhancement occurs at radial values between the other two. 49

3.8 Total helicity enhancement $h/h^{\mathrm{o}}_{\mathrm{inc}}$ around a spherical Si NA in the $x-z$ plane under optimally chiral ARPB illumination with half-waist $w_0 = \lambda$, obtained by free space Green's functions and Mie scattering calculations at λ = 680nm. At this wavelength, for a dielectric NA with radius a =78 nm (a), the optimal-chirality condition $|h| = u/\omega$ is satisfied in the nearfield, whereas for a=84 nm (b) and a=85 nm (c) maximum helicity and maximum energy enhancements are obtained, respectively. Maximum helicity enhancement occurs for a radius between that corresponding to the optimally chiral nearfield and that corresponding to maximum energy density. In (d) and (e) helicity enhancement and the quantity $h\omega/u$which takes the value of +1 for an optimally chiral ARPB with $V_{\mathrm{A}} = iV_{\mathrm{R}}$ around the Si NA with radius 78 nm obtained from FEM analysis are plotted. 52

4.1 The dissymmetry factor g reveals chirality of NP, when two optimally chiral electromagnetic fields with local helicity densities with opposite signs ($h^- = -h^+$) and equal time-averaged local electric and magnetic energy densities are employed. All these assumptions strongly simplify the expression of the g factor, that now depends only on the NP polarizability. This result is general to any structured light that satisfies the optimal chiral condition. 63
4.2 Real and imaginary parts of the chirality parameter κ of poly-L-glutamic acid (PGA). This data is used in the evaluation of the electromagnetic polarizability of a nanosphere made of such material in this chapter. 65
4.3 Real part of electromagnetic polarizability $\Re\{\alpha_{\mathrm{em}}\}$calculated for a spherical chiral NP composed of poly-L-glutamic acid (PGA) versus its radius a and wavelength λ. 67
4.4 Detectable and undetectable regions for a spherical chiral NPs with radius a composed of poly-L-glutamic acid (PGA). 68
4.5 Helicity density h of a Gaussian beam with circular polarization and beam parameter $w_0 = \lambda$, propagating along the z direction, (a) in the $x-y$ plane ($z = 0$) at the operational wavelength $\lambda = 210$nm, and (b) on the optical axis at $z = \rho = 0$ versus wavelength (still $w_0 = \lambda$) . The total power of the beam is 1 mW. 68
4.6 (a) Dissymmetry factor g for an individual spherical chiral NP made of poly-L-glutamic acid (PGA) with radius a. (b) Imaginary part of electric polarizability $\Im\{\alpha_{\mathrm{ee}}\}$. 70

5.1 (a) High-density dielectric nanoantenna (NA) with radius a located at the origin of a coordinate system and illuminated by a plane wave. (b) Scattering cross section σ_s of the NA versus operating wavelength λ for four distinct sphere's radii. In this example and in all the following ones the NA is made of Silicon. As it will be clear in the next figure, the peaks represent magnetic resonances. 77

5.2 (a) Magnitude and (b) normalized phase difference between of the electric α_{ee} and magnetic α_{mm} dipole polarizabilities of a single NA with radius a=85 nm made of Silicon. At λ = 730nm, the Kerker condition [6] is approximately satisfied, i.e., the balanced polarizabilities very closely satisfy $|\alpha_{ee}|/\epsilon_0 = |\alpha_{mm}|$ and $\Delta\varphi = 0$. 78
5.3 Term $\mathfrak{Re}\{\alpha_{ee}\alpha^*_{mm}\}/\epsilon_0$, which is proportional to h_{sca}/h_{inc}, for a single NA with radius a=85nm versus wavelength. This term takes its maximum around λ = 688nm, while it has a lower value at λ = 730 nm where polarizabilities are balanced. 81
5.4 Normalized helicity density to that of the incident field around a single NA with radius a =85 nm, irradiated by a plane wave with circular polarization at λ = 730nm, in $x-y$ plane, i.e., at $\theta = \pi/2$. Since illumination has circular polarization the distribution is symmetric in the azimuthal plane. 82
5.5 Plot of $\omega h/u$, i.e., of the product of the magnitude of helicity density and angular frequency normalized to the energy density, i.e., around a single NA with radius a=85 nm in the $x-y$ plane at wavelength λ = 730 nm. This quantity equals unity for optimally chiral fields and fields whose $\omega|h|/u$ values are close to unity are close to satisfying the required conditions to be optimally chiral. 83
5.6 Array of NAs with radius a arranged in the $x-y$ plane with period Λ, illuminated by a plane wave, propagating along the negative z direction. . . 84
5.7 88
5.8 (a) Effective polarizabilities of an array of spherical Si NAs with radius 85 nm and periodicity Λ = 220 nm deviate form optimally chiral condition $\alpha^{eff}_{ee}/\epsilon_0 = \alpha^{eff}_{mm}$. (b) The quantity $h\backslash omega/u$ in nearfield of the array illuminated by a left-handed circularly polarized plane wave at three different wavelengths: (i) at λ = 704 nm where $\Delta\varphi$ goes to zero; (ii), and at λ = 735 nm, where the minimum reflection from the array with periodicity Λ = 220 nm occurs; (iii) at λ = 752 nm where the relation $|\alpha^{eff}_{ee}|/\epsilon_0 = |\alpha^{eff}_{mm}|$ is satisfied. The relation $|h|\omega/u = 1$ is most nearly satisfied at λ = 735 nm. 90
5.9 Helicity enhancement, i.e., helicity density of an array of high-density NAs, with radius a = 85nm made of Si, normalized to that of the incident left-handed circularly polarized field at wavelength λ = 735 nm., evaluated at z = 0, and on the $y-z$ plane, respectively. Two arrays are considered with period of (a) Λ = 220nm, and (b) Λ = 190nm. Note the different scale, and the higher helicity for the case with period Λ = 190nm. 92
5.10 Helicity enhancement along the x axis and the diagonal line in a unit cell of an array of Si spheres with radius 85 nm and periodicity parameter Λ = 190nm, at the array plane z = 0. 93

5.11 Plot of $\omega h/u$, i.e., the product of helicity density and angular frequency normalized to the energy density, generated by an array of high-density NAs with radius a=85 nm illuminated by a left-handed circularly polarized plane wave. We show such quantity in the $x-y$ plane (at $z=0$) over a unit cell of the array with period (a) $\Lambda = 220$ nm, and (b)$\Lambda = 190$ nm. Note that $\omega\,|h|\,/u = 1$ for optimally chiral fields, and this plot shows that the field in the NA array is close to that limit. 94
5.12 (a) An array of high-density NAs with radius a =85 nm with periodicity Λ=270 nm located on a glass substrate with refractive index n =1.5 illuminated by left-handed circularly polarized plane wave propagating along the negative z direction, and (b) reflectivity r and transmittivity t of this array when the substrate has a finite thickness d=980 nm and also for the semi-infinite case when it occupies the region $z < a$. 96
5.13 Plot of $\omega h/u$, i.e., the product of helicity density and angular frequency normalized to the energy density, generated by an array of high-density NAs with radius a=85 nm and periodicity Λ=270 nm located on a glass substrate with refractive index n =1.5 illuminated by a left-handed circularly wave at wavelength $\lambda = 735$nm when (a) the substrate has an infinite thickness and it occupies the region z < a and (b) when it has a thickness d=980 nm. . . . 97

6.1 An array of infinite plasmonic rods and chains of gold NPs aligned perpendicular to the orientation of the rods located on a glass substrate may be fabricated by using dielectrophoresis. 102
6.2 (a) An array of rectangular plasmonic rods oriented parallel to the x axis, placed on top of a substrate and covered by a superstrate, is illuminated by a plane wane propagating anolg the $-z$ direction and polarized along the y axis. (b) Electromagnetic fields in the space below and above the array may be expanded into Floquet harmonics propagating along a discret set of directions. 103
6.3 (a) Nine probes $\mathrm{P}_1, ..., \mathrm{P}_9$ are located along the y axis in the $x-z$ plane of the optimized array to monitor the field enhancement. (b) A dimer is located in proximity of the plasmonic rod such that the middle of its gap is placed at the probe P_8.(c) A chain of nine NPs are arranged along the y axis and four probes $\mathrm{G}_1, .., \mathrm{G}_4$ are used to monitor the field enhancement in the Chain's hot spots. 105
6.4 The enhancement (a) in the magnitude FE and (b) in the y component FE_y of the electric field at probes $\mathrm{P}_1, ..., \mathrm{P}_9$ in the optimized array with periodicity $L_y = 500$nm, $H = W = 100$nm. 106
6.5 The enhancement (a) in the magnitude FE and (b) in the y componnet $FE_y$of the electric field at probes in the optimized array with parameters $L_y = 500$nm, $H = W = 100$nm and a semi-infinite glass substrate. 107
6.6 The field enhancement FE at probe P_1 in the middle of the gap of a dimer depicted in Figure 6.3(b) in the absence, marked as "Dimer", and presence, marked as "Dimer and rods", of the array of rods. Rods further enhance the electric field in the wavelength range from 780 to 850 nm marked by a red box. 109

6.7 The field enhancement FE at probes $G_1, ..., G_4$ in the hot spots of a chain depicted in Figure 6.3(c) in the absence, marked as "Chain", and presence, marked as "Chain and rods", of the array of rods. 110

ACKNOWLEDGMENTS

Foremost, I would like to express my deepest appreciation to Professor Filippo Capolino for his accompany on my PhD dissertation journey. His exemplary courage and enthusiasm for opening new horizons in research while preserving the scientific ethics, and his analytical intelligence have always been great sources of inspiration for me. I am particularly indebted to him for his invaluable lessons on how to fight for what I want. Moreover, I am extremely grateful to my collaborator and mentor Dr. Mohammad Albooyeh for his enthusiasm, moderation, and scientific professionalism during our insightful discussions on the materials presented in the first five chapters of this dissertation.

I would like to sincerely thank Professor Regina Ragan for her guidance on the last chapter of this dissertation, Rayleigh anomaly in surface enhanced Raman spectroscopy, which would not be accomplished without her support. This dissertation is partly associated to the research carried out at the W. M. Keck Structured Light Microscopy and Nanophotonics laboratory at UCI and I would like to thank the collaborators, Professor Eric Potma, Professor Kumar Wickramasinghe, and Dr. Jinwei Zeng for their great contributions. I am thankful to Dr. Mehdi Veysi and Dr. Caner Guclu for generously sharing their implementations of azimuthally and radially vector laser beams and Ewald Green's functions in MATLAB and CST Studio Suite which are used in some parts of this dissertation. I would like to thank Amy Pham, the graduate program coordinator at the department of electrical engineering and computer science at UCI, for her kind and sincere instructions. Furthermore, I thank my friends Hamidreza Kazemi and Robert Marosi for their sincere helps.

I gratefully acknowledge the funding I received towards my PhD from the W. M. Keck Foundation. I am also grateful to the funding I received through scholarships at UCI. I am thankful to DS SIMULIA for providing CST Studio Suite that was instrumental in this study.The text of this dissertation is a reprint of the materials as they appear in ACS Photonics, Physical Review B, the Journal of Applied Physics, and Proceedings SPIE.

VITA

Mina Hanifeh

EDUCATION

Doctor of Philosophy in electrical and computer engineering **2021**
University of California, Irvine *Irvine, CA*

Master's degree in electrical engineering - fields and waves **2014**
Universtity of Tehran *Tehran, Iran*

Bachelor's degree in electrical engineering - communications **2010**
Universtity of Tehran *Tehran, Iran*

SELECTED JOURNAL PUBLICATIONS

M. Hanifeh, M. Albooyeh, and F. Capolino, "Optimally chiral light: upper bound of helicity density of structured light for chirality detection of matter at nanoscale" **2020**
ACS Photonics

M. Hanifeh, M. Albooyeh, and F. Capolino, "Helicity maximization below the diffraction limit" **2020**
Physical Review B

M. Hanifeh and F. Capolino, "Helicity maximization in a planar array of achiral high density dielectric nanoparticles" **2020**
Journal of Applied Physics

SELECTED CONFERENCE PUBLICATIONS

M. Hanifeh, M. Albooyeh, and F. Capolino, "Empowering structured light to enhance chirality detection and characterization at nanoscale" **Feb 2018**
Complex Light and Optical Forces XIII conference

M. Albooyeh, M. Hanifeh, M. Kamandi, M. Rajaei, J. Zeng, H. K. Wickramasinghe, F. Capolino, "Photo-induced force vs power in chiral scatterers" **2017**
IEEE International Symposium on Antennas and Propagation & USNC/URSI National Radio Science Meeting

ABSTRACT OF THE DISSERTATION

Field Enhancement and Helicity Maximization of Structured Light for Chirality Detection and SERS Applications

By

Mina Hanifeh

Doctor of Philosophy in Electrical and Computer Engineering

University of California, Irvine, 2021

Professor Filippo Capolino, Chair

This dissertation is devoted to understanding the characteristics of an electromagnetic field associated to its interaction with matter and devising structured lights to innovate a platform for nanoscale circular dichroism and to extend the applications of surface enhanced Raman spectroscopy.

Circular dichroism is a spectroscopy technique used in characterization of the average of chirality in a sample by using circularly polarized plane waves. Here, we present a circular dichroism framework for characterization of chirality in nanoparticles instead of bulk of matter. To that end, similar to some previous studies, we employ Poynting theorem to analyze the interaction of electromagnetic fields with chiral matter and illustrate the significance of helicity density of the field in interaction with chital matter. We then proceed by introducing a universal upper bound for helicity density of electromagnetic fields which is linearly proportional to the energy density of the field divided to its angular frequency. We call electromagnetic fields reaching this upper bound optimally chiral and prove rigorously that an optimally chiral field possesses a pure spin angular momentum which is collinear with its linear momentum.

We also present some practical optimally chiral structured lights including optical laser beams

and the nearfield of a designed nanoantenna. The proposed optical laser beams include Gaussian beams with circular polarization and also a beam composed of a radially and an azimuthally polarized beam with specific phase shift and relative amplitudes. We also discuss in detail how to obtain an optimally chiral nearfield in the proximity of a nanoantenna which enables chirality characterization at nanoscale and below the diffraction limit. Indeed, we show that a nanoantenna with balanced electric and magnetic dipole moments generates optimally chiral scattered field which in combination with an optimally chiral incident field forms an optimally chiral total nearfield. Our investigations prove the importance of optimally chiral illumination when the nearfield of a nanoantenna is used in chirality characterization at the nanoscale. In particular, we explore helicity and energy densities in the nearfield of a spherical dielectric nanoantenna illuminated by an optimally chiral combination of azimuthally and radially polarized beams. This beam combination generates parallel induced electric and magnetic dipole moments in the nanoantenna that in turn generate optimally chiral scattered field with the same helicity sign of the incident field. The application of helicity maximization to nearfields results in helicity enhancement at nanoscale which is of great advantage in the detection of nanoscale chiral samples, microscopy, and optical manipulation of chiral nanoparticles.

Based upon the concept of helicity maximization, we devise a platform for chirality characterization of nanoparticles. The platform consists of measuring the extinction powers of a chiral nanoparticle in its interaction with two optimally chiral excitation in two separate experiments and employ the measured powers in dissymmetry factor g defined as the difference between the extinction powers divided to their arithmetic average. When the excitations possess equal electric and magnetic energy densities at the location of the chiral nanoparticle and helicity densities equal in magnitude and opposite signs, dissymmetry factor g is proportional to the chirality of the nanoparticle normalized to its electric polarizability. We further validate the feasibility of our proposed platform and showed that chiral nanoparticles made of PGA as small as 20 nm are detectable when utilizing

the instruments available in the market. We further demonstrate that using optimally chiral lights for determining the chirality of a nanoparticle using the dissymmetry factor g, eliminates the need of the specific knowledge of the values of field's energy and helicity densities. The helicity maximization concept generalizes the use of the dissymmetry factor for nanoparticle chirality detection to any chiral structured light illumination.

We also showed that the helicity maximization upgrades the conventional circular dichroism technique to chirality detection at the surface level instead of the bulk when the chiral sample is deposited on a substrate composed of an array of nanoantenna. We derived the required condition for an array of Silicon nanospheres to generates a planar distribution of optimally chiral nearfield, in terms of array effective electric and magnetic polarizabilities that satisfy the effective Kerker condition. Importantly the array would not contribute to the generated CD signal when used as a substrate for detecting chirality of a thin layer of chiral molecules. This eliminates the need to separate the CD signal generated by the array from that of the chiral sample.

Finally, we investigate the field enhancement in the hot spots of a chain of gold nanoparticles deposited on a substrate composed of an array of plasmonic rods on a glass slab. The proposed structure is fabricated by taking advantage of dielectrophoresis where the plasmonic rods on a glass substrate are used to apply an electric field to gold nanoparticles in a suspension to align them along a line perpendicular to the rods. We show that Rayleigh anomaly in the array of rods adds an extra factor to the field enhancement in the hot spot of the gold nanoparticles which in return enhances the Raman signal and improves the detection.

Chapter 1

Introduction

Spectroscopy is the science of quantifying materials' properties by measuring the interaction between electromagnetic fields and matter, and analysis of the derived spectra. Spectrometers examine interaction of electromagnetic fields with a sample to reveal its composition, physical and electronic structure, and optical properties and have applications in environmental analysis such as determination of metals in samples of water or soil, probing different water properties (such as acidity), and measuring the concentrations of certain compounds in the air mass. These instruments are also used in numerous biomedical diagnostic and therapeutic applications. They may assist certain therapeutic methods by supplying them with the data on the optical properties of tissues as well as providing non-invasive, label-free optical detection and measurement of specific molecules in human cells and tissues (such as hemoglobin protein). Spectrometers are also employed in space explorations to obtain information about the composition, density, temperature, and other principal physical processes of a certain astronomical object. An interesting example is the study of the spectral emission lines of distant galaxies which led to the discovery that the universe is expanding rapidly in all directions.

There are various spectroscopy techniques such as fluorescence spectroscopy[1], dielectric spectroscopy[2], and nuclear magnetic resonance spectroscopy [3] to name a few. Here, we focus our attention on circular dichroism (CD) [4] and surface enhanced Raman spectroscopy (SERS)[5, 6, 7] techniques. The former concerns with characterization of chirality in matter [8] while the latter is used to identify the molecules by observing their Raman signals[9].

Chirality, interpreted as lack of superimposable mirror images in an object [8], is an outspread geometrical property. For example, snails' shells and the arrangnement of petals in some flowers as depicted in Figure 1.1 are chiral. Chiral materials have building blocks, i.e., molecules, which take several topological forms while their chemical compositions stay the same. Each topological form of a chiral molecule is called an enantiomer. Most of the molecules of importance to living systems, e.g., amino acids, sugars, proteins, and nucleic acids, are chiral [8]. Chirality is a new concept in human sciences. In 1811, Arago observed that the plane of polarization of a linearly polarized wave rotates when it goes through quartz crystal, and later in 1820 Herschel discovered that the rotation occurs in opposite directions for crystals with mirrored structures. It was known that when quartz was melted or dissolved the rotation disappeared. Louis Pasteur attributed the phenomenon to the structure of the crystal and not the constituents and compared the structure of each crystal with a spiral stair which is not chiral when dismantled. Biot discovered that optical rotation occurs in natural liquids such as oils of lemon. In 1822, Fresnel explained that linearly polarized wave is a combination of fields rotating in opposite directions which move with different speeds when passing through the material and this results in the rotation of the plane of polarization of the field.

Enantiomers of a chiral material have similar chemical compositions but interact differently with other chiral substances such as various chemicals in our bodies. Therefore, different enantiomers may have conflicting impacts on our lives. For example, while one enantiomer of a chiral medicine is a cure, the other enantiomer may have negative impacts on our bodies.

Figure 1.1: Chiral spiral shape of a snail's shell and chiral orientation of petals in a flower.

One famous example of a chiral drug is Thalidomide where its S-isomer has the desired anti-nausea effect and its R-isomer is teratogenic and causes fetal abnormalities, such as severely underdeveloped limbs [8]. Most chiral artificial substances such as those used in the food and drug industries are produced in racemic mixtures which contain both enantiomers. Therefore many countries have restricted the marketing of racemic drugs (which contain both enantiomers) and have mounted regulatory pressures requiring pharmaceutical companies to provide bioactivity and biotoxicity data on individual enantiomeric drugs as well as on 50:50 or racemic mixtures. This results in applications of chirality spectroscopy methods such as circular dichroism in pharmaceutical chemistry, agriculture, and food science for quality control purposes to determine the enantiomeric pureness of chiral substances and produce safe and high-quality chiral medicines and foods without toxic enantiomers.

Circular dichroism is a spectroscopy technique to determine purity of a chiral sample where transmitted powers of circularly polarized plane waves with opposite handedness through a liquid solution of a sample are used to reveal its chirality. Similar to electric permittivity ϵ and magnetic permeability μ, a medium electromagnetic chirality is represented by κ in the material constitutive relations $\mathbf{D} = \epsilon\mathbf{E} + i\kappa\sqrt{\mu_0\epsilon_0}\mathbf{H}$ and $\mathbf{B} = \mu\mathbf{H} - i\kappa\sqrt{\mu_0\epsilon_0}\mathbf{E}$ that define the link between the electric and magnetic fields $\mathbf{E}$ and $\mathbf{H}$, and the electric displacement and magnetic induction vectors $\mathbf{D}$ and $\mathbf{B}$[10, 11]. Here, ϵ_0 and μ_0 are the vacuum permittivity and permeability, respectively, and we assume fields with time dependence $e^{-i\omega t}$, where ω is the angular frequency. Usually, chirality of a bulk material κ is detected and characterized

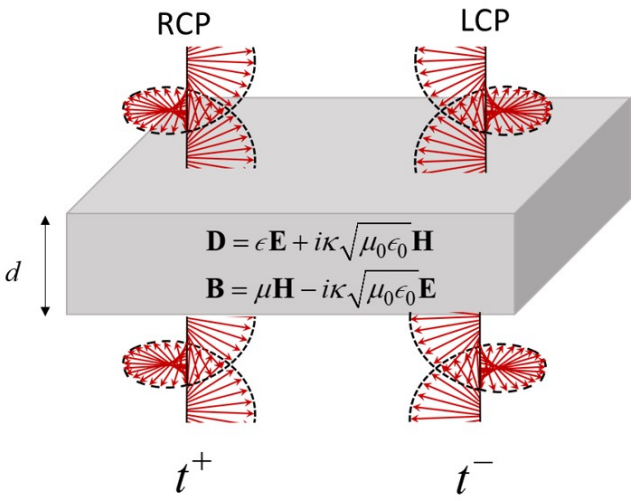

Figure 1.2: The transmitted powers of right and left handed circularly polarized plane waves (RCP and LCP) through a chiral medium reveals its chirality parameter κ.

through circular dichroism (CD) experiments[12]. For example, as illustrated in 1.2, exposing a film with thickness d to two distinct circularly polarized (CP) plane waves with polarization of opposite handedness, its chirality is characterized via

$$\Im\{\kappa\} = \frac{1}{2k_0 d}\tanh^{-1}\left(\frac{|t^-|^2 - |t^+|^2}{|t^+|^2 + |t^-|^2}\right), \tag{1.1}$$

where $t^{\pm}$ are the measured field-transmission coefficients in the two experiments, $\Im\{\cdot\}$ denotes for the imaginary part of a complex value, and k_0 is the wavenumber in vacuum.

In 1930, Kunh discussed a system of two coupled charged harmonic oscillators to describe chirality in a molecule by examining the interaction of this system with plane waves with right-handed and left-handed circular polarizations[13]. Indeed, he theoretically proved that the ratio of the difference between extinction powers in these interactions normalized to their arithmetic average, referred to dissymmetry factor g, reveals the chirality of a molecule. Recently, it has been proposed that employing two mirror-imaged electromagnetic fields, instead of circularly polarized plane waves, decomposes the dissymmetry factor g into a

product of molecule's chirality and a field term, containing the ratio of the helicity over energy density of the fields [14, 15]. This decomposition was an important step toward using structured light in chirality characterization of molecules and led to introduction of a quantitative measure, i.e., helicity density, for chirality of electromagnetic fields. Afterwards, several studies [16, 17, 18, 19, 20, 21, 22, 23, 24, 15] have been devoted to finding ways to enhance helicity density in order to improve the sensitivity of circular dichroism spectroscopy.

Although in CD experiments the interaction of light with the bulk of matter enables chirality detection by raising the measured difference of transmitted optical signals above the noise level, it may be unsatisfactory due to several reasons [25]. First, it requires a considerable amount of chiral sample to form a homogeneous layer where chirality is deducible from Eq. 3.1. Second, the chirality parameter provides only an homogenized average notion of the chirality of the material constituents forming a bulk (e.g. bulk mixture of molecules or engineered nanoparticles) [12]. Moreover, it is challenging to deduce chirality of individual constituents from the chirality of the bulk [26], for example when the absorption bands of the host and chiral inclusions overlap [27]. Considering these limitations and the need for expanding our understanding of physics of chiral nanoscale matter demanded by the growing field of nanotechnology, it is of utmost importance to move toward direct optical chirality characterization of individual NP. However, in the process of determining chirality properties of a small amount of molecules, it is yet remained unsolved how to factor out the "field term" from the dissymmetry factor g. In this dissertation, we introduce a universal upper bound for helicity density of electromagnetic fields and use electromagnetic fields reaching this upper bound to develop a novel platform for chirality characterization of individual nanoparticles which removes the field term from dissymmetry factor g.

Any spectroscopy technique is established based upon two facts: the material property which is to be determined and the quantity which measures the interaction between the electromagnetic field and matter. Matter interacting with an electromagnetic field may

absorb a portion of the excitation energy and scatter the rest at the same or different wavelength. We consider classical electromagnetic fields and employ the Poynting theorem [28] to study light-matter interaction. Poynting theorem states the conservation of energy in a closed system of interacting electromagnetic field and matter and enables us to quantify the interaction based on absorption power, scattered power, or the summation of these two known as the extinction power. All these measurable quantities may be used in a spectroscopy technique to model the light-matter interaction and their choice depends on the convenience in revealing the desired material property. For example, as we discussed in Chapter 4 in this dissertation, extinction power enables to reveal the chirality of a particle while scattered or absorption powers are not an appropriate candidates in circular dichroism spectroscopy. Poyting theorem also enables to define linear momentum as well as spin and orbital angular momentum mechanical properties for classical electromagnetic fields. Besides linear and angular momentum, helicity of electromagnetic fields has recently attracted a considerable attention due to its importance in studying chirality of matter. These quantities are not measurable, however they enable us to explain the characteristics of light-matter interactions. For example, helicity density of an electromagnetic field plays a significant role in its interaction with matter. Therefore, we devote Chapter 2 of this dissertation to briefly review Poyting theorem and mechanical characteritics of electromagnetic fields which form the foundation for the discussions presented in the proceeding chapters. We also introduce an upper bound for helicity density of electromagnetic fields and show that this upper bound is linearly linked to energy density through a universal constant which solely depends on the angular frequency of the field. We call electromagnetic fields reaching the upper bound of their helicity densities, optimally chiral and proved that optimally chiral fields possess pure spin angular momenta, meaning that their orbital angular momentum vanish.

In Cpater 3, we present several optimally chiral fields. We first investigate the helicity density in Gaussian beams with circular polarization. Moreover, we show that the superposition of an azimuthally polarized beam (APB) [29, 30, 31, 32, 33] and a radially polarized beam

(RPB) [33, 34, 35], called ARPB, with appropriate relative amplitudes and phase difference [36] is optimally chiral. Furthermore, we show how to generate optimally chiral nearfield and helicity enhancement at nanoscale by employing an achiral dielectric nanoantenna (NA). To that end, we show that helicity density of the nearfield of a NA is divided into three parts: helicity densities of the incident and scattered fields and a part related to interference between these two. We prove that to have an optimally chiral total nearfield (the superposition of incident and scattered fields) it is required to excite the NA by an optimally chiral incident field. We also derive the required conditions a NA needs to satisfy in terms of induced electric and magnetic dipole moments, and hence of its dipolar polarizabilities, to generate optimally chiral scattered nearfield whose helicity is constructive with the one of the incident field and the "interference" helicity term. We investigate helicity density of the nearfield of a spherical dielectric NA illuminated by an optimally chiral ARPB and a circularly polarized Gassian beam.

In Chapter 4, we establish a theoretical platform to characterize chirality of NPs when general electromagnetic fields, including any structured light, are utilized. Our general optimization scheme is based on the linear relation between energy and helicity densities and aims at simplifying the dissymmetry factor g. We show the general principle that the use of optimally chiral light simplifies the expression of the dissymmetry factor g and it eliminates the need of the specific knowledge of the "field term", i.e., the knowledge of the value of the ration of energy and helicity densities of the two fields used in the two experiments. Our numerical analysis show that when the proposed platform is implemented by using technologies available in the market, it can reveal chirality of a nanoparticle as small as a few nanometers. Our findings prove that any optimally chiral structured light such as nearfields of nanoantennas can replace circularly polarized plane waves in chiral spectroscopy.

Although helicity density is enhanced in vicinity of a single designed nanoantenna, it drops

very quickly moving away from its surface. This prevents a considerable amount of the chiral sample interacts with the field and a strong circular dichroism signal is not generated. In Chapter 5, we design an array of nanoantennas to generate a planar distribution of enhanced maximized helicity density over a surface where the chiral sample is deposited. We design a high-density dielectric spherical nanoantenna to have balanced electric and magnetic polarizabilities which generates symmetric distribution of maximized helicity density in its equatorial plane when excited by a circularly polarized plane wave. Our numerical simulations show that arranging these elements in an array prevents the drop in helicity density of each element and provides a planar distribution of maximized helicity density in their mutual equatorial plane. We rigorously prove how helicity maximization is related to the effective Kerker condition of effective polarizabilities of the array and this is affected by the array periodicity. Moreover, we show that adding a glass substrate to the array, which is essential for practical reasons, does not affect its helicity distribution and enhancement. One advantage of using our proposed array is that it is not chiral and does not generate a circular dichroism signal by itself and the detected signal is only attributed to the chirality of the matter deposited on it. In conclusion, using this array as a substrate for chiral samples helps to enhance precision of existing circular dichroism spectrometers without a need for any modifications to spectrometers and at no cost.

In Chapter 6, we investigate the field enhancement in surface enhanced Raman spectroscopy (or scattering), abbreviated as SERS, where plasmonic structures are used to enhance the Raman signal emitted by molecules in their proximity. The high sensitivity provided by SERS in detection of molecules has made it a popular spectroscopy technique with a broad range of applications in biotechnology and biology[37, 38], analytical chemistry[39, 40], pharmaceutical field [41, 42], and forensic sciences [43]. It is shown that the SERS enhancement factor is proportional to the fourth power of the enhancement in the magnitude of the electric field with respect to that of the excitation [44]. Here, we design a plasmonic substrate for SERS applications which provides an enhancement factor of ...^4 in the

wavelength range 780 to 850 nm by combining the field enhancement provided by the Rayleigh anomaly and that in the hot spots of a chain of gold nanoparticles.

Bibliography

[1] J. R. Lakowicz, *Principles of Fluorescence Spectroscopy.* Springer, Boston, MA, 1983.

[2] F. Kremer and A. Schönhals, *Broadband Dielectric Spectroscopy.* Springer-Verlag Berlin Heidelberg, 2003.

[3] R. J. Abraham, J. Fisher, and P. Loftus, *Introduction to NMR Spectroscopy.* John Wiley & Sons, 1988.

[4] A. Rodger and B. Norden, *Circular dichroism and linear dichroism.* Oxford University Press, 1977.

[5] J. A. Dieringer, A. D. McFarland, N. C. Shah, D. A. Stuart, A. V. Whitney, C. R. Yonzon, M. A. Young, X. Zhang, and R. P. Van Duyne, "Introductory lecture surface enhanced raman spectroscopy: new materials, concepts, characterization tools, and applications," *Faraday Discuss.*, vol. 132, pp. 9–26, 2006.

[6] E. Le Ru and P. Etchegoin, *Principles of Surface-Enhanced Raman Spectroscopy.* Elsevier Science, 2008.

[7] K. Kneipp, M. Moskovits, and H. Kneipp, *Surface-Enhanced Raman Scattering, Physics and Applications.* Springer-Verlag Berlin Heidelberg, 2006.

[8] J. P. Riehl, *Mirror-Image Asymmetry: An Introduction to the Origin and Consequences of Chirality.* John Wiley & Sons, Hoboken, New Jersey, 2011.

[9] D. A. Long, *Raman Spectroscopy.* McGraw-Hill, New York, 1977.

[10] Jin Au Kong, "Theorems of bianisotropic media," *Proceedings of the IEEE*, vol. 60, no. 9, pp. 1036–1046, 1972.

[11] A. Serdiukov, I. Semchenko, S. Tretyakov, and A. Sihvola, *Electromagnetics of Bi-Anisotropic Materials - Theory and Application.* Gordon and Breach Science Publishers, 2001.

[12] I. Lindell, A. Sihvola, S. Tretyakov, and A. Viitanen, *Electromagnetic Waves in Chiral and Bi-Isotropic Media.* Artech House, 1994.

[13] W. Kuhn, "The physical significance of optical rotatory power," *Z. physik. Chem.*, 1930.

[14] Y. Tang and A. E. Cohen, "Optical chirality and its interaction with matter," *Phys. Rev. Lett.*, vol. 104, p. 163901, Apr 2010.

[15] Y. Tang and A. E. Cohen, "Enhanced enantioselectivity in excitation of chiral molecules by superchiral light," *Science*, vol. 332, no. 6027, pp. 333–336, 2011.

[16] J. Shao and P. Hänggi, "Control of molecular chirality," *The Journal of Chemical Physics*, vol. 107, no. 23, pp. 9935–9941, 1997.

[17] M. Schäferling, D. Dregely, M. Hentschel, and H. Giessen, "Tailoring enhanced optical chirality: Design principles for chiral plasmonic nanostructures," *Phys. Rev. X*, vol. 2, p. 031010, Aug 2012.

[18] M. Hentschel, M. Schäferling, X. Duan, H. Giessen, and N. Liu, "Chiral plasmonics," *Science Advances*, vol. 3, no. 5, 2017.

[19] A. O. Govorov, Z. Fan, P. Hernandez, J. M. Slocik, and R. R. Naik, "Theory of circular dichroism of nanomaterials comprising chiral molecules and nanocrystals: Plasmon enhancement, dipole interactions, and dielectric effects," *Nano Letters*, vol. 10, no. 4, pp. 1374–1382, 2010. PMID: 20184381.

[20] M. Nieto-Vesperinas, "Chiral optical fields: a unified formulation of helicity scattered from particles and dichroism enhancement," *Philosophical Transactions of the Royal Society A: Mathematical, Physical and Engineering Sciences*, vol. 375, no. 2090, p. 20160314, 2017.

[21] V. K. Valev, J. J. Baumberg, C. Sibilia, and T. Verbiest, "Chirality and chiroptical effects in plasmonic nanostructures: Fundamentals, recent progress, and outlook," *Advanced Materials*, vol. 25, no. 18, pp. 2517–2534, 2013.

[22] A. García-Etxarri and J. A. Dionne, "Surface-enhanced circular dichroism spectroscopy mediated by nonchiral nanoantennas," *Phys. Rev. B*, vol. 87, p. 235409, Jun 2013.

[23] C.-S. Ho, A. Garcia-Etxarri, Y. Zhao, and J. Dionne, "Enhancing enantioselective absorption using dielectric nanospheres," *ACS Photonics*, vol. 4, no. 2, pp. 197–203, 2017.

[24] M. L. Solomon, J. Hu, M. Lawrence, A. García-Etxarri, and J. A. Dionne, "Enantiospecific optical enhancement of chiral sensing and separation with dielectric metasurfaces," *ACS Photonics*, vol. 6, no. 1, pp. 43–49, 2019.

[25] J. O. Arroyo and P. Kukura, "Non-fluorescent schemes for single-molecule detection, imaging and spectroscopy," *Nature Photonics*, vol. 10, 2016.

[26] A. H. Sihvola and I. V. Lindell, "Analysis on chiral mixtures," *Journal of Electromagnetic Waves and Applications*, vol. 6, no. 5-6, pp. 553–572, 1992.

[27] E. Condon, *Theories of Optical Rotatory Power*. Springer, New York, NY, 1991.

[28] J. D. Jackson, *Classical Electrodynamics*. John Wiley & Sons, New York, 1998.

[29] M. Veysi, C. Guclu, and F. Capolino, "Focused azimuthally polarized vector beam and spatial magnetic resolution below the diffraction limit," *J. Opt. Soc. Am. B*, vol. 33, pp. 2265–2277, Nov 2016.

[30] J. Zeng, F. Huang, C. Guclu, M. Veysi, M. Albooyeh, H. K. Wickramasinghe, and F. Capolino, "Sharply focused azimuthally polarized beams with magnetic dominance: Near-field characterization at nanoscale by photoinduced force microscopy," *ACS Photonics*, vol. 5, no. 2, pp. 390–397, 2018.

[31] C. Guclu, M. Veysi, and F. Capolino, "Photoinduced magnetic nanoprobe excited by an azimuthally polarized vector beam," *ACS Photonics*, vol. 3, no. 11, pp. 2049–2058, 2016.

[32] M. Darvishzadeh-Varcheie, C. Guclu, and F. Capolino, "Magnetic nanoantennas made of plasmonic nanoclusters for photoinduced magnetic field enhancement," *Phys. Rev. Applied*, vol. 8, p. 024033, Aug 2017.

[33] A. Holleczek, A. Aiello, C. Gabriel, C. Marquardt, and G. Leuchs, "Classical and quantum properties of cylindrically polarized states of light," *Opt. Express*, vol. 19, pp. 9714–9736, May 2011.

[34] R. Oron, S. Blit, N. Davidson, A. A. Friesem, Z. Bomzon, and E. Hasman, "The formation of laser beams with pure azimuthal or radial polarization," *Applied Physics Letters*, vol. 77, no. 21, pp. 3322–3324, 2000.

[35] H. Rubinsztein-Dunlop, A. Forbes, M. V. Berry, M. R. Dennis, D. L. Andrews, M. Mansuripur, C. Denz, C. Alpmann, P. Banzer, T. Bauer, E. Karimi, L. Marrucci, M. Padgett, M. Ritsch-Marte, N. M. Litchinitser, N. P. Bigelow, C. Rosales-Guzmán, A. Belmonte, J. P. Torres, T. W. Neely, M. Baker, R. Gordon, A. B. Stilgoe, J. Romero, A. G. White, R. Fickler, A. E. Willner, G. Xie, B. McMorran, and A. M. Weiner, "Roadmap on structured light," *Journal of Optics*, vol. 19, p. 013001, nov 2016.

[36] M. Kamandi, M. Albooyeh, M. Veysi, M. Rajaei, J. Zeng, H. K. Wickramasinghe, and F. Capolino, "Unscrambling structured chirality with structured light at the nanoscale using photoinduced force," *ACS Photonics*, vol. 5, no. 11, pp. 4360–4370, 2018.

[37] T. M. Cotton, J.-H. Kim, and G. D. Chumanov, "Application of surface-enhanced raman spectroscopy to biological systems," *Journal of Raman Spectroscopy*, vol. 22, no. 12, pp. 729–742, 1991.

[38] D. Cialla-May, X. S. Zheng, K. Weber, and J. Popp, "Recent progress in surface-enhanced raman spectroscopy for biological and biomedical applications: from cells to clinics," *The Royal Society of Chemistry*, vol. 46, pp. 3945–3961, 2017.

[39] G. McNay, D. Eustace, W. E. Smith, K. Faulds, and D. Graham, "Surface-enhanced raman scattering (sers) and surface-enhanced resonance raman scattering (serrs): A review of applications," *Appl. Spectrosc.*, vol. 65, pp. 825–837, Aug 2011.

[40] S. Schlücker, "Surface-enhanced raman spectroscopy: Concepts and chemical applications," *Angewandte Chemie International Edition*, vol. 53, no. 19, pp. 4756–4795, 2014.

[41] J. Cailletaud, C. De Bleye, E. Dumont, P. Y. Sacré, L. Netchacovitch, Y. Gut, M. Boiret, Y. M. Ginot, P. Hubert, and E. Ziemons, "Critical review of surface-enhanced raman spectroscopy applications in the pharmaceutical field," *Journal of Pharmaceutical and Biomedical Analysis*, vol. 147, pp. 458–472, 2018. Review issue 2017.

[42] M. T. Alula, Z. T. Mengesha, and E. Mwenesongole, "Advances in surface-enhanced raman spectroscopy for analysis of pharmaceuticals: A review," *Vibrational Spectroscopy*, vol. 98, pp. 50–63, 2018.

[43] C. Muehlethaler, M. Leona, and J. R. Lombardi, "Review of surface enhanced raman scattering applications in forensic science," *Analytical Chemistry*, vol. 88, no. 1, pp. 152–169, 2016. PMID: 26638887.

[44] S.-Y. Ding, E.-M. You, Z.-Q. Tian, and M. Moskovits, "Electromagnetic theories of surface-enhanced raman spectroscopy," *Chem. Soc. Rev.*, vol. 46, pp. 4042–4076, 2017.

Chapter 2

Light-Matter Interaction

The Poynting theorem is concerned with the conservation of energy of electromagnetic fields and is one of the fundamental laws in electromagnetism which leads us to define momentum and angular momentum for classical electromagnetic fields [1]. While the electromagnetic power flow is the quantity usually measured in experimental setups, the mechanical properties attributed to electromagnetic fields are not directly observable and their nature is yet to be understood. However, these auxiliary quantities enable us to explain our observations of interactions between electromagnetic fields and matter. Particularly, the exchange of energy between a chiral medium and an electromagnetic field is determined by the spin angular momentum and helicity of the field.

In this chapter, we briefly discuss the Poynting theorem and mechanical properties of electromagnetic fields. In particular, we introduce a universal upper bound of helicity density that is the maximum helicity light can have at a given light energy density. Helicity maximization as discussed here is applicable to any structured light and defines optimally chiral fields used in chirality characterization of nanoparticles disscussed in proceeding chapters. Finally, we provide some properties of spin, angular momentum (AM) and

momentum of a monochromatic (time-harmonic) optimally chiral field. The time dependence $e^{-i\omega t}$, where ω is the angular frequency, is implicitly assumed and SI units are employed.

2.1 Some Mechanical Properties of Electromagnetic Fields

According to the Poynting Theorem [1] in phasor terms, the power of an electromagnetic field generated by an electric current density $\mathbf{j}_{\text{elec}}$ in a volume V satisfies

$$-\frac{1}{2}\int_V \mathbf{j}_{\text{elec}} \cdot \mathbf{E}^* dv = 2\omega i \int_V (u_{\text{e}} - u_{\text{m}}) dv + \int_V \nabla \cdot \mathbf{S}_{\text{power}} dv. \tag{2.1}$$

Here, $u_{\text{e}} = \mathbf{E} \cdot \mathbf{D}^*/4$ and $u_{\text{m}} = \mathbf{B} \cdot \mathbf{H}^*/4$ are, respectively, the electric and magnetic energy densities, and $\mathbf{S}_{\text{power}} = (\mathbf{E} \times \mathbf{H}^*)/2$ is the energy flux density of the field. The time-averaged physical values are obtained by taking the real part. Moreover, for simplicity we assume that electromagnetic fields are in vacuum.

Conservation of linear and angular momenta of charged particles interacting with electromagnetic fields has led us to also define these mechanical quantities for classical electromagnetic fields [1]. In phasor terms, density of momentum and AM of an electromagnetic field are, respectively, defined as $\boldsymbol{p} = \epsilon_0(\mathbf{E} \times \mathbf{B}^*)/2$ and $\boldsymbol{j} = \mathbf{r} \times \boldsymbol{p}$ which satisfy conservation rules [1, 2]. The total AM of the electromagnetic field in the volume V, given by $\mathcal{J} = \int_V \boldsymbol{j} dv$ is decomposed into three parts [3]:

$$\mathcal{J} = \mathcal{L} + \mathcal{S} + \Omega \tag{2.2}$$

where $\mathcal{L} = \int_V \boldsymbol{l} dv$ and $\mathcal{S} = \int_V \boldsymbol{l}\, dv$ are, respectively, the total orbital AM (OAM) and the total spin AM (SAM) of the field. The densities of orbital $\boldsymbol{l}$ and spin $\boldsymbol{s}$ AM of the field are obtained as [4, 3, 5, 6, 7]

$$\begin{aligned} \boldsymbol{l} &= \tfrac{\epsilon_0}{4}\mathbf{r} \times \left(\sum_{j=x,y,z} E_j \nabla A_j^* - \sum_{j=x,y,z} B_j \nabla F_j^* \right) \\ s &= \tfrac{\epsilon_0}{4} \left(\mathbf{E} \times \mathbf{A}^* + \mathbf{F} \times \mathbf{B}^* \right) \end{aligned} \tag{2.3}$$

where $\mathbf{F}$ and $\mathbf{A}$ are auxiliary magnetic and electric vector potentials that give $\mathbf{E} = \nabla \times \mathbf{E}$ and $\mathbf{B} = \nabla \times \mathbf{A}$. Note that Coulomb gauge $\nabla \cdot \mathbf{A} = 0$ and $\nabla \cdot \mathbf{F} = 0$ is used [8], and the Heaviside-Larmor symmetry in Maxwell's equation in free space is considered by employing both of electric and magnetic vector potentials [4, 2, 6, 7, 3]. Moreover, following the same method in Ref. [3] for both auxiliary electric and magnetic vector potentials (only the part with the electric vector potential $\mathbf{F}$ is given in Ref. [3]), the third term in the right hand side of Eq. 2.2 in this chapter reads

$$\Omega = \frac{\epsilon_0}{4} \int\limits_{\partial V} \left[\mathbf{B} \left(\mathbf{r} \times \mathbf{F}^* \right) - \mathbf{E} \left(\mathbf{r} \times \mathbf{A}^* \right) \right] \cdot d\mathbf{s}. \tag{2.4}$$

In contrast to linear and angular momenta of electromagnetic fields which are defined based on conservation of these quantities in interaction between an electromagnetic field and matter, helicity as one of the conserved quantities for classical electromagnetic fields has been defined based on mathematical concepts rather than mechanical ones, in terms of quantified knottedness or curlieness of a vector field [9]. In this regard, helicity density for time harmonic electromagnetic fields reads [9, 10, 4] (when using the International System

of Units)

$$h = \frac{1}{4c_0}(\epsilon_0 \mathbf{F}^* \cdot \nabla \times \mathbf{F} + \mu_0^{-1} \mathbf{A}^* \cdot \nabla \times \mathbf{A}), \tag{2.5}$$

where $c_0 = 1/\sqrt{\mu_0 \epsilon_0}$ is the speed of light in vacuum. Further investigation has clarified the physical significance of helicity, and it was shown that the mathematical integration of h defined in Eq. 2.5 over the whole space is indeed related to the classical limit of the difference between the number of right-handed and left-handed photons in the field [10]. Helicity is also closely related to optical chirality, whose time-averaged expression is defined as [11, 12]

$$C = \frac{1}{4}(\epsilon_0 \mathbf{E}^* \cdot \nabla \times \mathbf{E} + \mu_0^{-1} \mathbf{B}^* \cdot \nabla \times \mathbf{B}) \tag{2.6}$$

which is a quantitative measure of handedness of electromagnetic fields to represent the strength of field for detection of chirality of matter [12, 13]. For time-harmonic electromagnetic fields, the time-averaged helicity density reduces to [9, 10, 4, 2, 14]

$$h = \frac{\Im\{\mathbf{E} \cdot \mathbf{H}^*\}}{2\omega c_0}, \tag{2.7}$$

where $\Im\{\cdot\}$ denotes for the imaginary part of a complex value, and indeed the time-averaged optical chirality and helicity densities are proportional: $C = \omega^2 c_0^{-1} h$ [4]. In this dissertation, we adopt helicity as a measure to quantify fields' chirality.

2.2 Chiral Light-Matter Interaction

To illustrate the importance of helicity density in a chiral light-matter interaction, we discuss the power flow in chiral media using the Poynting theorem. Let us assume a lossy and dispersionless chiral medium occupies a volume V enclosed by a surface S and we assume there is no electromagnetic source inside it. According to Eq. 2.1, the total net time-averaged power flowing out of the surface S reads

$$\int_S \Re\left\{\mathbf{S}_{\text{power}}\right\} \cdot d\mathbf{s} = 2\omega \int_V \Im\left\{u_{\text{e}} - u_{\text{m}}\right\} dv. \tag{2.8}$$

Substituting the constitutive relations $\mathbf{D} = \epsilon\mathbf{E} + i\kappa\sqrt{\mu_0\epsilon_0}\mathbf{H}$ and $\mathbf{B} = \mu\mathbf{H} - i\kappa\sqrt{\mu_0\epsilon_0}\mathbf{E}$ into the right hand side of Eq. 2.8, the integrand $\Im\left\{u_{\text{e}} - u_{\text{m}}\right\}$ reads

$$\Im\left\{u_{\text{e}} - u_{\text{m}}\right\} = -\frac{\Im\left\{\epsilon\right\}}{4}\left|\mathbf{E}\right|^2 - \frac{\Im\left\{\mu\right\}}{4}\left|\mathbf{H}\right|^2 - \frac{\sqrt{\mu_0\epsilon_0}\Im\left\{\kappa\right\}}{2}\Im\left\{\mathbf{E}\cdot\mathbf{H}^*\right\}. \tag{2.9}$$

Therefore the power conservation law is rewritten as

$$-\int_S \Re\left\{\mathbf{S}_{\text{power}}\right\}\cdot d\mathbf{s} = 2\omega \int_V \left(\frac{\Im\left\{\epsilon\right\}}{4}\left|\mathbf{E}\right|^2 + \frac{\Im\left\{\mu\right\}}{4}\left|\mathbf{H}\right|^2 + \frac{\sqrt{\mu_0\epsilon_0}\Im\left\{\kappa\right\}}{2}\Im\left\{\mathbf{E}\cdot\mathbf{H}^*\right\}\right) dv \tag{2.10}$$

This equation shows the net time-averaged power entering the volume V (the left hand side) is equal to the the power dissipated inside such volume represented by the three terms on the right hand side: the first two are familiar terms, whereas the third one is proportional to the imaginary part of the chirality parameter κ; moreover, the sign of the dissipation of the chiral term with $\Im\left\{\kappa\right\}$ depends also on the sign of $\Im\left\{\mathbf{E}\cdot\mathbf{H}^*\right\}$. The fundamental constraints

the constitutive parameters have to satisfy in a lossy medium are $\Im\{\epsilon\} > 0$, $\Im\{\mu\} > 0$, and $(\Im\{\kappa\})^2 < \Im\{\epsilon\}\Im\{\mu\}/(\epsilon_0\mu_0)$ as discussed in Ch. 2 of Ref. [15]. In lossless medium, κ is purely real.

Now, we consider a nanoparticle (NP) whose optical response is well approximated by the fundamental electric and magnetic dipole moments, and higher order multipoles are considered negligible, which is a judicious and common assumption for optically small NPs. Moreover, we assume that the NP is isotropic, reciprocal, and is surrounded by an isotropic non-dispersive medium and hence induced electric $\mathbf{p}$ and magnetic $\mathbf{m}$ dipole moments are linearly related to local electric and magnetic fields via polarizabilities through relations [16]

$$\begin{aligned} \mathbf{p} &= \alpha_{\mathrm{ee}}\mathbf{E} + \alpha_{\mathrm{em}}\mathrm{H} \\ \mathbf{m} &= -\mu_0^{-1}\alpha_{\mathrm{em}}\mathbf{E} + \alpha_{\mathrm{mm}}\mathbf{H}. \end{aligned} \tag{2.11}$$

Here α_{ee} and α_{mm} are the electric and magnetic polarizabilities of the NP, respectively, and the magnetoelectric polarizability α_{em} describes the NP's optical chirality. The magnetic dipole moment is defined as $\mathbf{m} = \frac{1}{2}\int_{\mathrm{V}} \mathbf{r} \times \mathbf{J}(\mathbf{r})\, dv$ where $\mathbf{J}(\mathbf{r})$ is displacement current density in the NP. Employing Eq. 2.11 in the Poynting theorem 2.1, the time-averaged extinction power P_{ext}, which is a convenient representative of the NP's interaction with light, is obtained as [17]

$$P_{\mathrm{ext}} = 2\epsilon_0^{-1}\omega\Im\{\alpha_{\mathrm{ee}}\}\, u_{\mathrm{e}} + 2\omega\Im\{\alpha_{\mathrm{mm}}\}\, u_{\mathrm{m}} - 2c_0\omega^2\Re\{\alpha_{\mathrm{em}}\}\, h. \tag{2.12}$$

Here, $u_{\mathrm{e}} = \epsilon_0|\mathbf{E}|^2/4$ and $u_{\mathrm{m}} = \mu_0|\mathbf{H}|^2/4$ are, respectively, the time-averaged electric and magnetic energy densities of the local field. Equations 2.10 and 2.12 show that interaction

between an electromagnetic field and a chiral medium is influenced by helicity density of the field. Next, we present an upper bound for helicity density of electromagnetic fields.

2.3 Helicity Maximization and Physical Significance of Optimally Chiral Fields

Let us denote the electric and magnetic fields by $\mathbf{E} = |\mathbf{E}|\hat{\mathbf{e}}$ and $\mathbf{H} = |\mathbf{H}|\hat{\mathbf{h}}$, where $\hat{\mathbf{e}}$ and $\hat{\mathbf{h}}$ are complex dimensionless unit vectors. Therefore, averaged time-harmonic helicity density in Eq. 2.7 reads

$$h = |\mathbf{E}||\mathbf{H}|\frac{\Im\{\hat{\mathbf{e}}\cdot\hat{\mathbf{h}}^*\}}{2\omega c_0}. \tag{2.13}$$

This means that the two components $\Im\{\hat{\mathbf{e}}\cdot\hat{\mathbf{h}}^*\}$ and $|\mathbf{E}||\mathbf{H}|$ which are linked to the polarization and the amplitude of the field, must be simultaneously maximized in order to maximize helicity density h. While the maximum value of $\left|\Im\{\hat{\mathbf{e}}\cdot\hat{\mathbf{h}}^*\}\right|$ is unity, that of the term $|\mathbf{E}||\mathbf{H}|$ requires some elaboration since field amplitudes can be unconditionally increased. We consider here general structured light, and in the discussion, we keep its total time-averaged energy density $u = u_\mathrm{e} + u_\mathrm{m}$ constant. Employing the method of Lagrange multipliers [18] the maximum of $|\mathbf{E}||\mathbf{H}|$, under the constraint of constant energy density u, occurs when $|\mathbf{E}| = \eta_0|\mathbf{H}|$, where $\eta_0 = \sqrt{\mu_0/\epsilon_0}$ is the free space wave impedance.

Despite the above rigorous proof, because of the generality and importance of this concept, it may be useful to provide an easy visualization of the maximization procedure. Hence, we employ an alternative, simple, graphic proof. Let us consider fields that locally have constant time-averaged energy density denoted by u_0. These local fields are represented

with the constant energy-density circle (red solid curve) in the $|\mathbf{E}|$, $|\eta_0\mathbf{H}|$ plane in Figure 2.1 defined by $|\mathbf{E}|^2 + |\eta_0\mathbf{H}|^2 = 4\epsilon_0^{-1}u_0$. Moreover, in such plane let us consider three distinct local field configurations that have three distinct values of helicity density amplitude $|h| = |\mathbf{E}||\mathbf{H}|/(2\omega c_0)$; each curve has a hyperbolic shape in the $|\mathbf{E}|$, $|\eta_0\mathbf{H}|$ plane (dashed and dot-ted lines). We assume that all these three distinct field scenarios already satisfy the maximum condition pertaining to the unit vectors (i.e., the polarization). We assume that all these three distinct field scenarios already satisfy the maximum condition pertaining to the unit vectors (i.e., the polarization) $\Im\{\hat{\mathbf{e}}\cdot\hat{\mathbf{h}}^*\} = \pm 1$. It is then obvious that for a given field energy density (e.g., $u = u_0$) the maximum $|h|$ achieved by field is represented by the tangent point between the $u = u_0$ circle and the hyperbolic curve, and such maximum helicity takes the value of $|h_0| = u_0/\omega$. Because of the symmetry of these curves, the maximum of $|h|$ occurs when $|\mathbf{E}| = \eta_0|\mathbf{H}|$. Concluding, we claim that any structured light that locally satisfies the two conditions

$$\begin{aligned} &\Im\{\mathbf{E}\cdot\mathbf{H}^*\} = \pm\,|\mathbf{E}|\,|\mathbf{H}| \\ &|\mathbf{E}| = \eta_0\,|\mathbf{H}| \end{aligned} \tag{2.14}$$

possesses the maximum available local helicity density attributed to its given energy density. We call fields satisfying conditions 2.14 optimally chiral, since this is an universal law that shows that no higher chirality is achievable at a given total time-averaged energy density. We stress again that this result is general, and applicable to any structured light, in the near and in the far field regions.

In summary, the concept of optimally chiral light indicates that for any structured light, at any given point, the maximum helicity density is $|h| = u/\omega$, where $u = u_\mathrm{e} + u_\mathrm{m}$. Therefore, if the optimal chirality condition is not met, light has because is the helicity upper bound. Another collateral but important result is inferred from Figure 2.1: helicity at a given electric

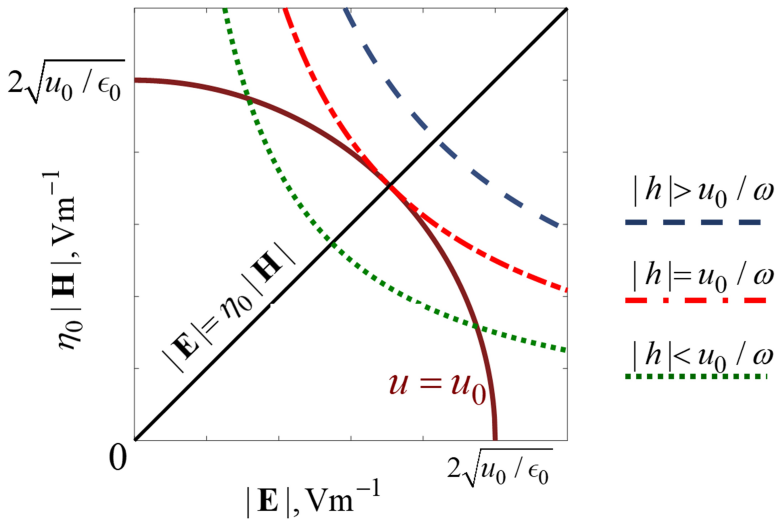

Figure 2.1: The general concept of helicity maximization. The red solid circle represents fields with constant energy density u_0, whereas the dashed and dotted lines represent fields with three constant helicity densities. The black solid straight line represents fields with $|h| = u/\omega$, that also defines maximum helicity density at a given energy density u_0.

field energy density u_e could be enhanced by locally increasing only the magnetic field (i.e., enhancing u_m), stating that structured light with enhanced magnetic field could be rather important for enhancing helicity. However, this latter case does not constitute chiral light and would have some consequences on the determination of the dissymmetry factor g described later on in this dissertation. In several cases, instead, electric field enhancement (i.e., enhancement of u_e) is generated and this also may enhance helicity. However, in any case helicity is subject to the bound $|h| \leq (u_\mathrm{e} + u_\mathrm{m})/\omega$.

The physical significance of optimally chiral fields becomes clear when we consider angular and linear momenta of electromagnetic fields. In an optimally chiral field, the electric and magnetic fields are linked via the relation

$$\mathbf{E} = \pm i\eta_0\mathbf{H}. \tag{2.15}$$

Therefore, the densities of linear momentum, orbital AM, and spin AM of an optimally chiral

field are obtained as

$$
\begin{aligned}
\boldsymbol{p}^{\pm} &= \tfrac{\mp i}{2c_0^2\eta_0}(\mathbf{E}\times\mathbf{E}^*) = \tfrac{\mp i\eta_0}{2c_0^2}(\mathbf{H}\times\mathbf{H}^*) = \tfrac{\mp i}{4c_0^2\eta_0}(\mathbf{E}\times\mathbf{E}^* + \eta_0^2\mathbf{H}\times\mathbf{H}^*) \\
\boldsymbol{s}^{\pm} &= -\tfrac{\epsilon_0}{4i\omega}\,(\mathbf{E}\times\mathbf{E}^* + \eta_0^2\mathbf{H}\times\mathbf{H}^*) \\
\boldsymbol{l}^{\pm} &= \tfrac{\epsilon_0}{4i\omega}\mathbf{r}\times\left(\sum_{j=x,y,z} E_j\nabla E_j^* - \sum_{j=x,y,z} E_j\nabla E_j^*\right) = 0.
\end{aligned}
\tag{2.16}
$$

In these equations the super script $\pm$ refers to the $\pm$ sign used in the relation $\mathbf{E} = \pm i\eta_0\mathbf{H}$. Note also that the integral in Eq. 2.4 vanishes, i.e., $\Omega = 0$ for optimally chiral fields. Equation 2.16 shows that the orbital AM $\boldsymbol{l}$ of an optimally chiral field vanishes and therefore, in an optimally chiral field, the total AM consists purely of the SAM. Moreover, the above relations show that the spin AM $\boldsymbol{s}^{\pm}$ and the linear momentum $\boldsymbol{p}^{\pm}$ densities in an optimally chiral field are collinear.

Bibliography

[1] J. D. Jackson, *Classical Electrodynamics*. John Wiley & Sons, New York, 1998.

[2] K. Y. Bliokh, A. Y. Bekshaev, and F. Nori, "Dual electromagnetism: helicity, spin, momentum and angular momentum," *New Journal of Physics*, vol. 15, p. 033026, mar 2013.

[3] A. M. Stewart, "Angular momentum of the electromagnetic field: the plane wave paradox resolved," *European Journal of Physics*, vol. 26, pp. 635–641, may 2005.

[4] R. P. Cameron, S. M. Barnett, and A. M. Yao, "Optical helicity, optical spin and related quantities in electromagnetic theory," *New Journal of Physics*, vol. 14, p. 053050, may 2012.

[5] H. C. Ohanian, "What is spin?," *American Journal of Physics*, vol. 54, no. 6, pp. 500–505, 1986.

[6] S. M. Barnett and L. Allen, "Orbital angular momentum and nonparaxial light beams," *Optics Communications*, vol. 110, no. 5, pp. 670–678, 1994.

[7] S. M. Barnett, "Rotation of electromagnetic fields and the nature of optical angular momentum," *Journal of Modern Optics*, vol. 57, no. 14-15, pp. 1339–1343, 2010. PMID: 24808629.

[8] S. M. Barnett, R. P. Cameron, and A. M. Yao, "Duplex symmetry and its relation to the conservation of optical helicity," *Phys. Rev. A*, vol. 86, p. 013845, Jul 2012.

[9] A. F. Ranada, "On the magnetic helicity," *European Journal of Physics*, vol. 13, pp. 70–76, mar 1992.

[10] J. L. Trueba and A. F. Rañada, "The electromagnetic helicity," *European Journal of Physics*, vol. 17, pp. 141–144, may 1996.

[11] J. E. Vázquez-Lozano and A. Martínez, "Optical chirality in dispersive and lossy media," *Phys. Rev. Lett.*, vol. 121, p. 043901, Jul 2018.

[12] Y. Tang and A. E. Cohen, "Optical chirality and its interaction with matter," *Phys. Rev. Lett.*, vol. 104, p. 163901, Apr 2010.

[13] Y. Tang and A. E. Cohen, "Enhanced enantioselectivity in excitation of chiral molecules by superchiral light," *Science*, vol. 332, no. 6027, pp. 333–336, 2011.

[14] I. Fernandez-Corbaton, X. Zambrana-Puyalto, N. Tischler, X. Vidal, M. L. Juan, and G. Molina-Terriza, "Electromagnetic duality symmetry and helicity conservation for the macroscopic maxwell's equations," *Phys. Rev. Lett.*, vol. 111, p. 060401, Aug 2013.

[15] I. Lindell, A. Sihvola, S. Tretyakov, and A. Viitanen, *Electromagnetic Waves in Chiral and Bi-Isotropic Media*. Artech House, 1994.

[16] A. Serdiukov, I. Semchenko, S. Tretyakov, and A. Sihvola, *Electromagnetics of Bi-Anisotropic Materials - Theory and Application*. Gordon and Breach Science Publishers, 2001.

[17] M. Hanifeh, M. Albooyeh, and F. Capolino, "Empowering structured light to enhance chirality detection and characterization at nanoscale," in *Complex Light and Optical Forces XIII* (J. Glückstad, D. L. Andrews, and E. J. Galvez, eds.), vol. 10935, pp. 8 – 19, International Society for Optics and Photonics, SPIE, 2019.

[18] R. A. Adams, *A Complete Course Calculus*. Addison-Wesley Publishers Limited, 1995.

Chapter 3

Optimally Chiral Electromagnetic Fields

In this chapter, we study in detail the properties of two illustrative examples of structured lights, i.e., an optical beam and the nearfield of a nanoantenna, both with maximized helicity density. First, we investigate the helicity densities of Guassian beams with circular polarization, and a combination of azimuthally and radially polarized beams, and demonstrate how they offer the possibility of enhancing helicity densities by manipulating their field profiles and polarizations. Moreover, we demonstrate how to engineer a nanoantenna to locally maximize helicity in its nearfield when illuminated by optimally chiral beams. The proposed electromagnetic fields provide a strong theoretical foundation in the study of nanoscale chirality detection and characterization of nanoparticles (NPs) using structured lights.

3.1 Gaussian Beams with Circular Polarization

We first consider a Gaussian beam (GB) with circular polarization. Suppressing the time dependence $e^{-i\omega t}$, the electric field vector of a GB which travels in the z direction under the paraxial approximation reads [1]

$$\mathbf{E} = \frac{V_G}{w} e^{-(\rho/w)^2} e^{ik\rho^2/(2R)} e^{-i\tan^{-1}(z/z_{\mathrm{R}})} e^{ikz} (\hat{\mathbf{x}} \pm i\hat{\mathbf{y}}), \tag{3.1}$$

where $-/+$ sign, represents right/left-handed circular polarization, and $\hat{\mathbf{x}}$ and $\hat{\mathbf{y}}$ are the unit vectors in the Cartesian coordinate system. Here, $z_R = \pi w_0^2/\lambda$, $w = w_0\sqrt{1+(z/z_R)^2}$, $\zeta = 1 - iz/z_R$, and $R = z\,[1+(z_R/z)^2]$, where w_0 and λ are, respectively, the beam parameter and the excitation wavelength. The beam parameter w_0 represents half a beam waist when the beam is not tightly focused [2]. Moreover, ρ and V_G are, respectively, the radial distance from the beam axis (here the z-axis of the Cartesian coordinate system) and the complex amplitude of the beam (with the unit of Volt). The magnitude of the electric field of a typical GB with $w_0 = \lambda$ in the $x-z$ plane and the electric field vectors along the propagation direction (here the z-axis) are depicted in Figure 3.1 (a) and (b), respectively.

The z component of the magnetic field of a circularly polarized GB with electric field defined in Eq. 3.1 is obtained by applying Maxwell's equation $\mathbf{H} = (i\omega\mu_0)^{-1}\nabla \times \mathbf{E}$ leading to

$$H_z = \frac{-2V_G}{\omega\mu_0} \left(\frac{ik}{2R} - \frac{1}{w^2}\right) \left(\frac{\rho}{w}\right) e^{i\Phi}, \tag{3.2}$$

with $\Phi = i(\rho/w)^2 + k\rho^2/(2R) - \tan^{-1}(z/z_R) + kz - \varphi$. This component is negligible when $\rho \ll w$ or in other words when $\rho \ll w_0$. Therefore, when $\rho \ll w_0$ the field of a chiral GB

locally resembles that of a plane wave with circular polarization.

Next, we illustrate the helicity densities of two circularly polarized GBs with equal total power and different beam parameters $w_0 = \lambda$ and $w_0 = 2\lambda$ normalized to the helicity density of a GB with the same power and $w_0 = 3\lambda$, all evaluated at the $z = 0$ plane in Figure 3.1 (c) and (d), respectively. We recall that by increasing the beam parameter w_0 the GB looks more like a plane wave. As it is clear from these figures, reducing the beam parameter w_0 results in an enhancement in the helicity density of the beam around its optical axis. This is due to the localization of the energy density at these points. It is noteworthy that the GB in Eq. 3.1 is obtained under paraxial approximation and it optimally chiral, i.e., satisfies condition $|h| = u/\omega$, only when $\rho << w_0$, which is a restricted area in space, since under these conditions the fields of a GB look more like those of a plane wave. The quantity $|h|\omega/u$, which takes the value of 1 when the condition $|h| = u/\omega$ are satisfied, is depicted in Figure 3.1 (e) and (f) for circularly polarized GBs with different values of beam parameters. The deviation of this quantity from unity by moving away from the beam axis means that tightly focused GBs are not the best candidate for chirality characterization since condition $|h| = u/\omega$ are not precisely satisfied everywhere in space. Therefore, in the next step we propose to use an engineered structured light beam with the interesting property of satisfying condition $|h| = u/\omega$ every-where in space.

3.2 Azimuthally Radially Polarized Beam

Azimuthally polarized beam (APB) and radially polarized beam (RPB) are obtained by superposing Laguerre Gaussian beams with opposite angular momenta [2, 3, 4, 5]. The electric field vector (in phasor terms) in an APB propagating along the $+z$ direction (optical axis of the beam) is polarized along the azimuthal direction $\hat{\varphi}$ in the transverse plane that,

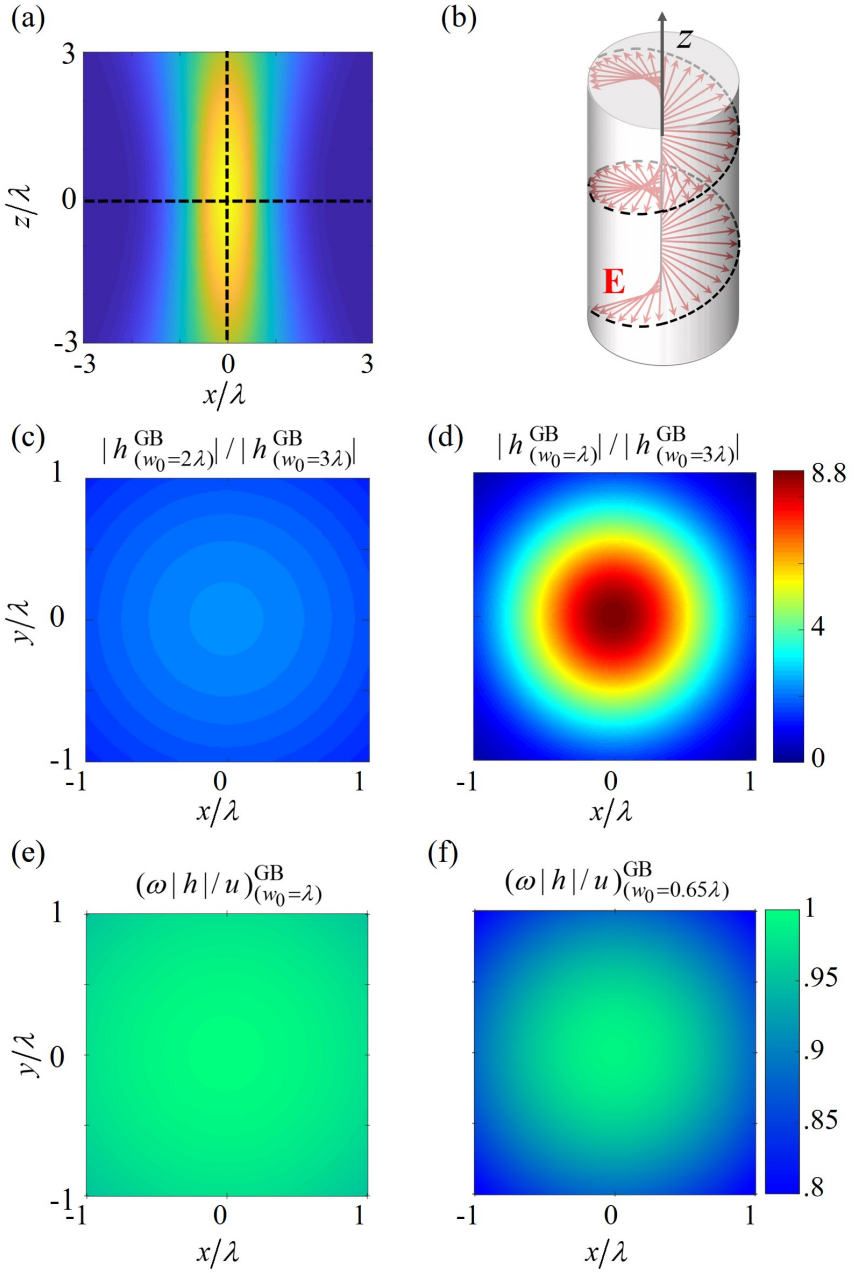

Figure 3.1: (a) Electric field magnitude in the $x-z$ plane and, (b) propagation of the electric field vector along the z-direction for a Gaussian beam with circular polarization and $w_0 = \lambda$ propagating along the z direction. Helicity density h of the GB on the $z = 0$ transverse plane when (c) $w_0 = 2\lambda$, and (d) $w_0 = \lambda$, normalized to that of a GB with the same power and $w_0 = 3\lambda$. Note that the helicity density at the center of the coordinate system of the beam with $w_0 = \lambda$ is approximately four times stronger than that of the beam with $w_0 = 2\lambda$, confirming that the helicity density is enhanced when the beam parameter w_0 decreases i.e., for tighter focused beams. The quantity for circularly polarized GB with (e) $w_0 = 3\lambda$ and (f) $w_0 = 0.65\lambda$.

after suppressing the time dependence $e^{-i\omega t}$, reads [2]

$$\mathbf{E}^{\mathrm{APB}} = \frac{2V_A\rho}{\sqrt{\pi}w^2} e^{-(\rho/w)^2\zeta} e^{-2i\tan^{-1}(z/z_{\mathrm{R}})} e^{ikz}\hat{\varphi}, \tag{3.3}$$

where V_A (with the unit of Volt) is the complex amplitude of the beam. The beam parameter w_0 represents half of the minimum beam waist when the beam is not tightly focused [2]. Moreover, ρ is the radial distance from the beam axis (the z-axis). Components of magnetic field vector in an APB are obtained from source-free Maxwell's curl equation $\nabla \times \mathbf{E}^{\mathrm{APB}} = i\omega\mu_0\mathbf{H}^{\mathrm{APB}}$ and read

$$\begin{aligned} H_\rho^{\mathrm{APB}} &= -\frac{E_\varphi^{\mathrm{APB}}}{\eta_0}\left(1 + \frac{1}{kz_R}\frac{\rho^2-2w_0^2}{w^2} - \frac{4i}{w^2}\frac{z}{z_R}\frac{1}{k^2}\left(1-\frac{\rho^2\varsigma}{w^2}\right)\right) \\ H_z^{\mathrm{APB}} &= \frac{2E_\varphi^{\mathrm{APB}}}{i\omega\mu_0\rho}\left(1-\frac{\rho^2}{w^2}\varsigma\right). \end{aligned} \tag{3.4}$$

It is important to note that such a beam has vanishing electric field and vanishing transverse magnetic fields at its optical axis. Moreover, the longitudinal magnetic field component takes the value $\lim_{\rho\to 0} H_z^{\mathrm{APB}} = 4V_A\left(i\omega\mu_0\sqrt{\pi}w^2\right)^{-1} e^{-2i\tan^{-1}(z/z_{\mathrm{R}})} e^{ikz}$ along its optical axis. In summary, around the beam's optical axis a magnetic dominant region exists. Dual to the APB, the RPB has magnetic field vectors which are polarized along the azimuthal direction and read

$$\mathbf{H}^{\mathrm{RPB}} = \frac{2V_R\rho}{\eta_0\sqrt{\pi}w^2} e^{-(\rho/w)^2\zeta} e^{-2i\tan^{-1}(z/z_{\mathrm{R}})} e^{ikz}\hat{\varphi}, \tag{3.5}$$

with a complex amplitude V_{R} (with the unit of Volt). Components of electric field in an

RPB are obtained via source-free Maxwell's curl equation $\nabla \times \mathbf{H}^{\mathrm{RPB}} = -i\omega\epsilon_0 \mathbf{E}^{\mathrm{RPB}}$ and read

$$\begin{aligned} E_{\rho}^{\mathrm{RPB}} &= \eta_0 H_{\varphi}^{\mathrm{RPB}} \left(1 + \tfrac{1}{kz_R} \tfrac{\rho^2 - 2w_0^2}{w^2} - \tfrac{4i}{w^2} \tfrac{z}{z_R} \tfrac{1}{k^2} \left(1 - \tfrac{\rho^2 \varsigma}{w^2}\right)\right) \\ E_{z}^{\mathrm{RPB}} &= -\tfrac{2H_{\varphi}^{\mathrm{RPB}}}{i\omega\epsilon_0 \rho} \left(1 - \tfrac{\rho^2}{w^2}\varsigma\right) \end{aligned} \tag{3.6}$$

Note, an RPB has a nonzero longitudinal electric field component $\lim_{\rho \to 0} E_z^{\mathrm{RPB}} = ic_0 4V_{\mathrm{R}} \left(\omega\sqrt{\pi}w^2\right)^{-1} e^{-2i\tan^{-1}(z/z_{\mathrm{R}})} e^{ikz}$ along its axis [1, 2, 5], where the magnetic field $\mathbf{H}^{\mathrm{RPB}}$ and the transverse component of the electric field E_{ρ}^{RPB} vanish.

The azimuthally-radially polarized beam (ARPB) is the superposition of these two vortex beams, i.e.,

$$\begin{aligned} \mathbf{E}^{\mathrm{ARPB}} &= \mathbf{E}^{\mathrm{APB}} + \mathbf{E}^{\mathrm{RPB}}, \\ \mathbf{H}^{\mathrm{ARPB}} &= \mathbf{H}^{\mathrm{APB}} + \mathbf{H}^{\mathrm{RPB}}, \end{aligned} \tag{3.7}$$

with the same beam parameters. Indeed, it is easy to deduce that an ARPB possesses both electric and magnetic field components along the azimuth direction $\hat{\varphi}$ as well as along the radial and longitudinal directions $\hat{\rho}$ and $\hat{\mathbf{z}}$. Moreover, since $\mathbf{E}^{\mathrm{APB}} = \eta_0 V_A V_R^{-1} \mathbf{H}^{\mathrm{RPB}}$, Eq. 3.7 simplifies to

$$\begin{aligned} \mathbf{E}^{\mathrm{ARPB}} &= \eta_0 V_A V_R^{-1} \mathbf{H}^{\mathrm{RPB}} + \mathbf{E}^{\mathrm{RPB}}, \\ \mathbf{H}^{\mathrm{ARPB}} &= \mathbf{H}^{\mathrm{RPB}} + \eta_0^{-1} V_A^{-1} V_R \mathbf{E}^{\mathrm{RPB}}, \end{aligned} \tag{3.8}$$

which shows that electric and magnetic field components of an ARPB are linked through $\mathbf{E}^{\mathrm{ARPB}} = \eta_0 V_A V_R^{-1} \mathbf{H}^{\mathrm{ARPB}}$. Therefore, when the amplitudes satisfy $V_A = \pm i V_R$, the ARPB

constitutes an optimally chiral optical beam that satisfies condition (2-14) everywhere in space (under paraxial approximation) because $V_A V_R^{-1} = \pm i$.

In Figure 3.2 (a) the electric field magnitude $|\mathbf{E}^{\mathrm{ARPB}}|$ of an optimally chiral ARPB with $V_{\mathrm{A}} = \pm i V_{\mathrm{R}}$ propagating along the z direction with total power of 1 mW and beam parameter $w_0 = \lambda$, is depicted. The plot is obtained by a full-wave simulation using the finite element method (FEM) implemented in CST Studio Suite at wavelength $\lambda = 680$nm. One interesting feature of an ARPB is that it has exclusively longitudinal electric E_z^{ARPB} and magnetic H_z^{ARPB} fields on the beam axis. In Figure 3.2 (b), the magnitude of longitudinal and transverse components of electric and magnetic fields in the same ARPB in Figure 3.2 (a), are depicted at the minimum waist plane of the beam (here the $z = 0$ plane). Moreover, the real part of the electric field vector component of the same beam at various $z =$ constant planes, is illustrated in Figure 3.2 (c). In summary, the electric and magnetic fields have a phase shift of $\pm\pi/2$, everywhere, in their longitudinal and transverse components. In particular, we stress that the purely-longitudinal field components on the beam axis are phase shifted by $\pm\pi/2$ and form an optimally chiral field. Indeed, helicity density on the axis of an ARPB illuminations, and at its minimum waist, reads

$$h^{\mathrm{ARPB}} = \frac{\mu_0}{2\omega}\left|\mathrm{H}^{\mathrm{ARPB}}\right|^2 \Im\left\{V_{\mathrm{A}} V_{\mathrm{R}}^{-1}\right\} = \frac{2u_{\mathrm{m}}^{\mathrm{ARPB}}}{\omega}\Im\left\{V_{\mathrm{A}} V_{\mathrm{R}}^{-1}\right\} \tag{3.9}$$

or equivalently

$$h^{\mathrm{ARPB}} = -\frac{\epsilon_0}{2\omega}\left|\mathbf{E}^{\mathrm{ARPB}}\right|^2 \Im\left\{V_{\mathrm{R}} V_{\mathrm{A}}^{-1}\right\} = \frac{-2u_{\mathrm{e}}^{\mathrm{ARPB}}}{\omega}\Im\left\{V_{\mathrm{A}}^{-1} V_{\mathrm{R}}\right\} \tag{3.10}$$

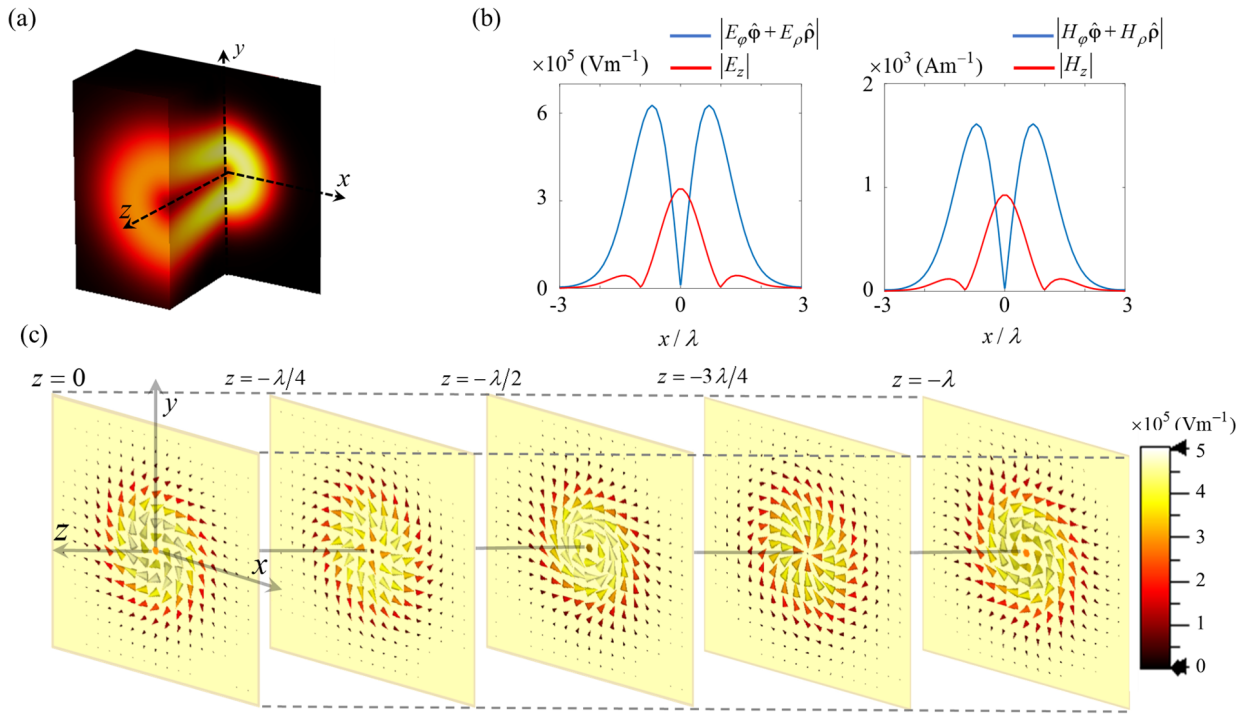

Figure 3.2: An optimally chiral ARPB with total power of 1 mW, beam parameter $w_0 = \lambda$, and amplitudes $V_\mathrm{A} = \pm iV_\mathrm{R}$ propagating along z direction, at wavelength $\lambda = 680$nm: (a) Three-dimensional plot of electric field's magnitude $\left|\mathbf{E}^{\mathrm{ARPB}}\right|$ in $x-y$ and $y-z$ planes. (b) Magnitudes of longitudinal and tangential components of electric and magnetic fields at the minimum waist plane $z = 0$. (c) Real part of the electric field vector represented by cones at various $z =$ constant planes. The results are obtained via FEM full-wave numerical analysis.

which shows that

$$h^{\mathrm{ARPB}} = \pm\frac{2u_\mathrm{e}^{\mathrm{ARPB}}}{\omega} = \pm\frac{2u_\mathrm{m}^{\mathrm{ARPB}}}{\omega} = \pm\frac{u^{\mathrm{ARPB}}}{\omega} \tag{3.11}$$

when $V_\mathrm{A} = \pm iV_\mathrm{R}$. Here, $u_\mathrm{m}^{\mathrm{ARPB}}$, $u_\mathrm{e}^{\mathrm{ARPB}}$, and u^{ARPB} are, respectively, electric, magnetic, and total energy densities of the incident ARPB.

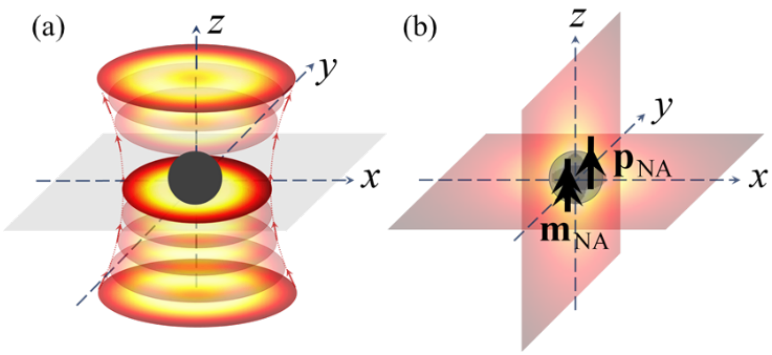

Figure 3.3: Nearfield of a NA is used to generate enhanced helicity density with respect to that of an incident beam. (a) An optical beam propagating along the $+z$ direction illuminates a NA located at the center of the coordinate system. (b) The dielectric NA is modeled by induced electric and magnetic dipole moments $\mathbf{p}_{\mathrm{NA}}$ and $\mathbf{m}_{\mathrm{NA}}$, respectively, and their scattered nearfields demonstrate high helicity density in the vicinity of the NA.

3.3 Optimally Chiral Nearfield

Nearfields of NAs overcome the diffraction limit and provide high spatial resolution in microscopy and spectroscopy. In the quest for chiral spectroscopy and microscopy at nanoscale, we found it essential to investigate how to design a NA that generates maximized helicity density, with spatial focusing below the diffraction limit. To that end, we assume that a NA is located at the center of a Cartesian coordinate system and it is illuminated by an optical beam propagating along the $+z$ direction as in Figure 3.3 (a).

The total nearfield of a NA includes contributions from both the incident optical beam and its scattered nearfield, denoted respectively by subscripts "inc" and "sca",

$$\begin{aligned} \mathbf{E} &= \mathbf{E}_{\mathrm{sca}} + \mathbf{E}_{\mathrm{inc}}, \\ \mathbf{H} &= \mathbf{H}_{\mathrm{sca}} + \mathbf{H}_{\mathrm{inc}}. \end{aligned} \tag{3.12}$$

Substituting Eq. 3.12 into $h = \Im\{\mathbf{E}\cdot\mathbf{H}^*\}/(2\omega c_0)$, the helicity density of the nearfield around

a NA reads

$$h = h_{\text{inc}} + h_{\text{sca}} + h_{\text{int}}, \tag{3.13}$$

where $h_{\text{sca}} = \Im\{\mathbf{E}_{\text{sca}} \cdot \mathbf{H}^*_{\text{sca}}\}/(2\omega c_0)$ and $h_{\text{inc}} = \Im\{\mathbf{E}_{\text{inc}} \cdot \mathbf{H}^*_{inc}\}/(2\omega c_0)$ are, respectively, the helicity densities of the scattered and incident fields. Moreover, h_{int}, which we call interference helicity density, reads

$$h_{\text{int}} = \frac{1}{2\omega c_0}\Im\left\{\mathbf{E}_{\text{sca}} \cdot \mathbf{H}^*_{\text{inc}} + \mathbf{E}_{\text{inc}} \cdot \mathbf{H}^*_{\text{sca}}\right\}. \tag{3.14}$$

Equation 3.14 suggests that for an improvement of helicity density we need to boost some of the helicity densities h_{int} and h_{sca}. Moreover, we require to manipulate incident and scattered fields so that all terms in Eq. 3.14 interfere constructively. Indeed, the helicity contributions from both incident and scattered fields as well as interference one should have similar signs to sum up constructively.

When both incident and scattered fields are optimally chiral, i.e., $\mathbf{E}_{\text{inc}} = \pm i\eta_0\mathbf{H}_{\text{inc}}$ and $\mathbf{E}_{\text{sca}} = \pm i\eta_0\mathbf{H}_{\text{sca}}$, the total nearfield is optimally chiral as well, i.e., $\mathbf{E} = \mathbf{E}_{\text{sca}} + \mathbf{E}_{\text{inc}} = \pm i\eta_0\left(\mathbf{H}_{\text{sca}} + \mathbf{H}_{\text{inc}}\right) = \pm i\eta_0\mathbf{H}$ in phasor terms. Therefore, we illuminate the NA by an optimally chiral beam and devote the rest of this section to investigate helicity density of the scattered nearfield h_{sca} and to the study of how the interference between the incident and scattered fields influences the helicity density of the total nearfield. Later, we discuss the importance of helicity density of the interference between incident and scattered fields.

Without loss of generality, we assume that the NA is isotropic operating in its dipolar regime, and model it by the induced electric and magnetic dipole moments $\mathbf{p}_{\text{NA}}$ and $\mathbf{m}_{\text{NA}}$,

respectively, located at the origin of the coordinate system (see Figure 3.3 (b)). Therefore, scattered electric and magnetic fields at position $\mathbf{r} = r\hat{\mathbf{r}}$, where the hat denotes a unit vector, read

$$\begin{aligned}\mathbf{E}_{\text{sca}} = &\left\{(\hat{\mathbf{r}} \times \mathbf{p}_{\text{NA}}) \times \hat{\mathbf{r}} - c_0^{-1}\left(1 + \tfrac{i}{kr}\right)(\hat{\mathbf{r}} \times \mathbf{m}_{\text{NA}}) + \right. \\ &\left. (\tfrac{1}{k^2r^2} - \tfrac{i}{kr})\left[3\hat{\mathbf{r}}(\hat{\mathbf{r}} \cdot \mathbf{p}_{\text{NA}}) - \mathbf{p}_{\text{NA}}\right]\right\}\end{aligned} \tag{3.15}$$

and

$$\begin{aligned}\mathbf{H}_{\text{sca}} = &\left\{(\hat{\mathbf{r}} \times \mathbf{m}_{\text{NA}}) \times \hat{\mathbf{r}} + c_0\left(1 + \tfrac{i}{kr}\right)(\hat{\mathbf{r}} \times \mathbf{p}_{\text{NA}}) + \right. \\ &\left. + \left(\tfrac{1}{r^2k^2} - \tfrac{i}{rk}\right)\left[3\hat{\mathbf{r}}(\hat{\mathbf{r}} \cdot \mathbf{m}_{\text{NA}}) - \mathbf{m}_{\text{NA}}\right]\right\} \tfrac{k^2 e^{ikr}}{4\pi r},\end{aligned} \tag{3.16}$$

, respectively, with k_0 being the wavenumber in vacuum. These two equations imply that the scattered field of the proposed NA is optimally chiral everywhere in space i.e., $\mathbf{E}_{\text{sca}} = \pm i\eta_0 \mathbf{H}_{\text{sca}}$, hence not only in the near-field zone of the NA, when $\mathbf{m}_{\text{NA}} = \mp i c_0 \mathbf{p}_{\text{NA}}$.

Therefore, the dominant contribution of the helicity density of scattered field in the near-zone of the NA at the radial positions $\mathbf{r} = r\hat{\mathbf{r}}$ reads

$$h_{\text{sca}} \approx \frac{\eta_0}{32\pi^2\omega r^6} \Im\left\{3\left(\hat{\mathbf{r}} \cdot \mathbf{p}_{\text{NA}}\right)\left(\hat{\mathbf{r}} \cdot \mathbf{m}_{\text{NA}}^*\right) + \mathbf{p}_{\text{NA}} \cdot \mathbf{m}_{\text{NA}}^*\right\}. \tag{3.17}$$

Note that in evaluating Eq. 3.17 for the nearfield of a NA, we have only considered the dominant terms with dependence r^{-3}. The term $\Im\{\mathbf{p}_{\text{NA}} \cdot \mathbf{m}_{\text{NA}}^*\}$ in Eq. 3.17 not only relates helicity to the strength of induced electric and magnetic dipole moments in a NA but also implies that the dipoles relative spatial orientation and phase should be controlled to

maximize helicity density of the scattered nearfield. Note that when the vector $\mathbf{r}$ is parallel to both dipole moments, the term $\Im\{3(\hat{\mathbf{r}}\cdot\mathbf{p}_{\mathrm{NA}})(\hat{\mathbf{r}}\cdot\mathbf{m}^{*}_{\mathrm{NA}})\}$ has a constructive contribution to the enhancement of the helicity density h_{sca}. In other words, the location vector $\mathbf{r}$ that satisfy this parallel property defines the regions where helicity around a NA is the strongest. Electric and magnetic dipole moments induced in a NA are obtained by employing a dielectric NA with high refractive index. In what follows, we examine thoroughly how to obtain optimally chiral scattered field when an achiral dielectric NA which does not possess electromagnetic polarizability is irradiated by an optimally chiral beam.

3.3.1 Dielectric NA Illuminated by an Optimally Chiral Field

The dipole moments $\mathbf{p}_{\mathrm{NA}}$ and $\mathbf{m}_{\mathrm{NA}}$ are, respectively, related to the incident electric $\mathbf{E}^{\mathrm{o}}_{\mathrm{inc}}$ and magnetic $\mathbf{H}^{\mathrm{o}}_{\mathrm{inc}}$ fields and at the position of the NA through the electric $\alpha^{\mathrm{NA}}_{\mathrm{ee}}$ and magnetic $\alpha^{\mathrm{NA}}_{\mathrm{mm}}$ polarizabilities and of the NA as

$$\begin{aligned}\mathbf{p}_{\mathrm{NA}} &= \alpha^{\mathrm{NA}}_{\mathrm{ee}}\mathbf{E}^{\mathrm{o}}_{\mathrm{inc}}\\ \mathbf{m}_{\mathrm{NA}} &= \alpha^{\mathrm{NA}}_{\mathrm{mm}}\mathbf{H}^{\mathrm{o}}_{\mathrm{inc}}.\end{aligned} \tag{3.18}$$

The superscript "o" denotes the NA's position which is the origin of the Coordinate system in our example. Since we consider an optimally chiral incident field, i.e., $\mathbf{E}^{\mathrm{o}}_{\mathrm{inc}} = \pm i\eta_0\mathbf{H}^{\mathrm{o}}_{\mathrm{inc}}$, according to Eq. 3.18, the relation $\mathbf{m}_{\mathrm{NA}} = \mp ic_0\mathbf{p}_{\mathrm{NA}}$ holds when the balance relation between the polarizabilities of the NA

$$\alpha^{\mathrm{NA}}_{\mathrm{ee}} = \epsilon_0\alpha^{\mathrm{NA}}_{\mathrm{mm}} \tag{3.19}$$

known as the first Kerker condition [6], is satisfied. Therefore, based on our previous discussion on Eqs. 3.15 and 3.16, the scattered field of the proposed NA (and not only in the near-field zone) is optimally chiral. In other words, the condition in Eq. 3.19 establishes the occurrence of the best possible scattered nearfield everywhere, in terms of optimal chirality of light, since the scattered field carries the same helicity of the incident field. In case the NA has a chiral component (i.e., it has an electromagnetic polarizability), the satisfaction of condition 3.19 still results in an optimally chiral scattered nearfield when the incident field is optimally chiral. However, a chiral NA unfavorably contributes to the circular dichroism signal in the chirality characterization of a nanoparticle sample [7]. Therefore, in this work we focus on describing achiral NAs.

Therefore, the problem of obtaining the maximum achievable helicity density of the scattered nearfield at a given energy density is reduced to acquiring a NA that satisfies the balance polarizability relation 3.19. Such a balance relation implies that the NA simultaneously possesses both electric and magnetic polarizabilities. Though materials with significant magnetic properties are not available at optical frequencies [8], "resonant magnetism" is possible for example with plasmonic clusters [9, 10, 11, 12, 13, 14, 15, 16, 17] or dielectric nanostructures [18, 19, 20, 21] that supports magnetic-like Mie resonances. In the next step, to illustrate in a simple way the proposed concepts, we analyze an isotropic achiral dielectric NA with spherical shape made of high refractive index material and investigate the possibility of generating optimally chiral total nearfield around this structure. Moreover, we analyze helicity enhancement due to the scattered and interreference fields and demonstrate that they have almost equal importance in enhancing helicity density with respect to that of the excitation beam. Furthermore, we investigate the relation between enhancement in energy and helicity densities in the nearfield of this NA.

As an example, we assume the spherical NA with radius a to be made of silicon (Si), and in Figure 3.4 (a) we plot the logarithm of normalized $|\alpha_{\mathrm{ee}}^{\mathrm{NA}} - \epsilon_0 \alpha_{\mathrm{mm}}^{\mathrm{NA}}|$ versus wavelength λ and

radius a. The quantity $|\alpha_{\mathrm{ee}}^{\mathrm{NA}} - \epsilon_0 \alpha_{\mathrm{mm}}^{\mathrm{NA}}|$ is normalized to its maximum in the shown wavelength-radius range, and it vanishes when the balance relation 3.19 is satisfied, which approximately corresponds to negative large values of its logarithm base 10. Note that polarizabilities take complex values, and the balance relation $\alpha_{\mathrm{ee}}^{\mathrm{NA}} = \epsilon_0 \alpha_{\mathrm{mm}}^{\mathrm{NA}}$ is satisfied when both magnitudes and phases of $\alpha_{\mathrm{ee}}^{\mathrm{NA}}$ and $\epsilon_0 \alpha_{\mathrm{mm}}^{\mathrm{NA}}$ are equal. The difference $|\alpha_{\mathrm{ee}}^{\mathrm{NA}} - \epsilon_0 \alpha_{\mathrm{mm}}^{\mathrm{NA}}|$ vanishes when the simultaneous satisfaction of equal magnitudes and phases of $\alpha_{\mathrm{ee}}^{\mathrm{NA}}$ and $\epsilon_0 \alpha_{\mathrm{mm}}^{\mathrm{NA}}$ is satisfied. Also note that for an efficient NA, low losses are desired and here, we assume the dielectric NA to be made of crystalline Si with dielectric permittivity taken from Ref. [83].

Note that when condition 3.19 approximately holds for a dielectric NA (e.g. on the dark regions in Figure 3.4(a)), the scattered nearfield, and consequently, the total field is optimally chiral. Moreover, although the spatial distribution of helicity density of the scattered nearfield is non-uniform around the NA, the relation $|h| = u/\omega$ holds everywhere in space as long as $\alpha_{\mathrm{ee}}^{\mathrm{NA}} = \epsilon_0 \alpha_{\mathrm{mm}}^{\mathrm{NA}}$ is valid for the proposed NA. We note quadrupoles for the considered parameters λ and a are negligible since $a/\lambda << 1$. In Figure 3.4 (b) we depict the magnitudes of the electric and magnetic polarizabilities, and their normalized phase difference $\Delta\varphi/\pi$ of a spherical NA made of Si with radius $a = 78$ nm. At wavelength $\lambda = 680$nm both relations $\left|\alpha_{\mathrm{ee}}^{\mathrm{NA}}\right| = \left|\epsilon_0 \alpha_{\mathrm{mm}}^{\mathrm{NA}}\right|$ and $\Delta\varphi = 0$ are approximately satisfied. This corresponds to dark region with value of -2 shown in Figure 3.4 (a).

For the sake of completeness, let us briefly examine optimal chirality condition for a reciprocal chiral NA where the dipole moments $\mathbf{p}_{\mathrm{NA}}$ and $\mathbf{m}_{\mathrm{NA}}$ are related to the incident electric and magnetic fields $\mathbf{E}_{\mathrm{inc}}^{\mathrm{o}}$ and $\mathbf{H}_{\mathrm{inc}}^{\mathrm{o}}$ at the position of the NA as

$$\begin{aligned} \mathbf{p}_{\mathrm{NA}} &= \alpha_{\mathrm{ee}}^{\mathrm{NA}} \mathbf{E}_{\mathrm{inc}}^{\mathrm{o}} + \alpha_{\mathrm{em}}^{\mathrm{NA}} \mathbf{H}_{\mathrm{inc}}^{\mathrm{o}}, \\ \mathbf{m}_{\mathrm{NA}} &= \alpha_{\mathrm{mm}}^{\mathrm{NA}} \mathbf{H}_{\mathrm{inc}}^{\mathrm{o}} - \mu_0^{-1} \alpha_{\mathrm{em}}^{\mathrm{NA}} \mathbf{E}_{\mathrm{inc}}^{\mathrm{o}} \end{aligned} \tag{3.20}$$

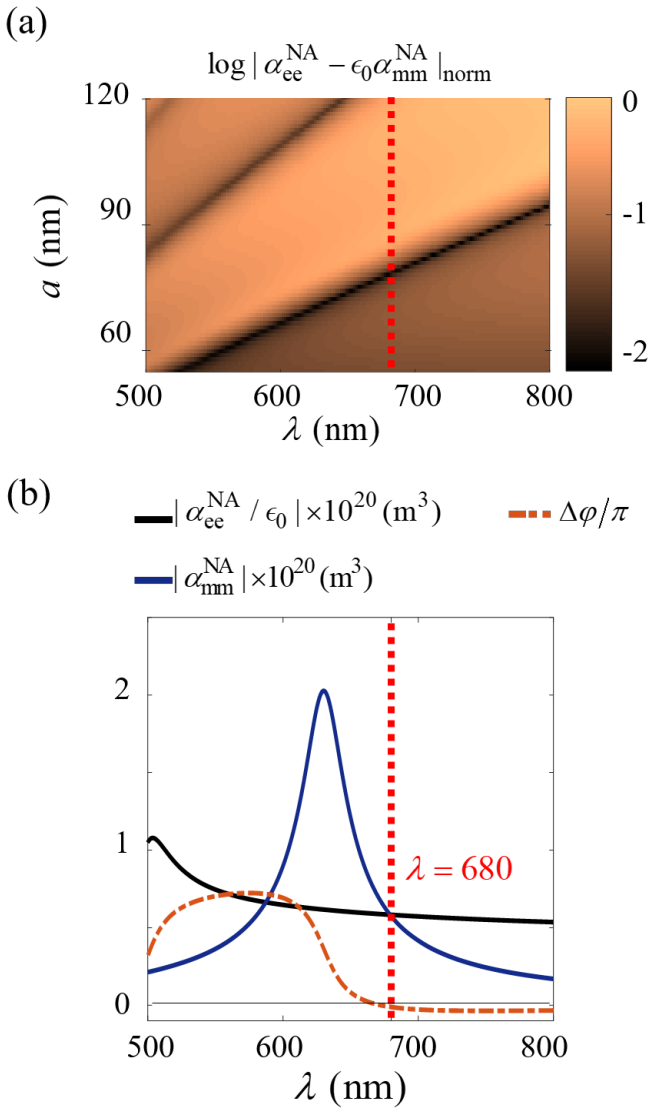

Figure 3.4: The polarizabilities of a spherical NA made of Si approximately satisfy the balance relation $\alpha_{ee}^{NA} = \epsilon_0\alpha_{mm}^{NA}$. (a) Plot of the logarithm of $\left|\alpha_{ee}^{NA} - \epsilon_0\alpha_{mm}^{NA}\right|$ (normalized to its maximum) which takes negative large value, around -2, where the balance relation $\alpha_{ee}^{NA} = \epsilon_0\alpha_{mm}^{NA}$ is approximately satisfied, versus radius a of the NA and wavelength of the excitation field λ. (b) Magnitudes of and phase difference between electric and magnetic polarizabilities of a NA with radius $a = 78$ nm versus wavelength λ. The refractive index of Si is obtained from Ref. [22] and the polarizabilities are calculated using the Mie scattering coefficients [23].

where is the electromagnetic polarizability $\alpha_{\rm em}^{\rm NA}$ of the NA and represents its chirality. The relation $\mathbf{m}_{\rm NA} = \pm ic_0 \mathbf{p}_{\rm NA}$ holds when

$$\alpha_{\rm mm}^{\rm NA} \mathbf{H}_{\rm inc}^{\rm o} - \mu_0^{-1} \alpha_{\rm em}^{\rm NA} \mathbf{E}_{\rm inc}^{\rm o} = \mp ic_0 \left(\alpha_{\rm ee}^{\rm NA} \mathbf{E}_{\rm inc}^{\rm o} + \alpha_{\rm em}^{\rm NA} \mathbf{H}_{\rm inc}^{\rm o} \right). \tag{3.21}$$

When the NA is illuminated by an optimally chiral incident field, i.e., when $\mathbf{E}_{\rm inc}^{\rm o} = \pm i\eta_0 \mathbf{H}_{\rm inc}^{\rm o}$, after some algebraic calculations, Eq. 3.21 simplifies to

$$\left(\alpha_{\rm mm}^{\rm NA} \mp ic_0 \alpha_{\rm em}^{\rm NA} \right) \mathbf{H}_{\rm inc}^{\rm o} = \left(\epsilon_0 \alpha_{\rm ee}^{\rm NA} \mp ic_0 \alpha_{\rm em}^{\rm NA} \right) \mathbf{H}_{\rm inc}^{\rm o}. \tag{3.22}$$

This is then reduced to $\alpha_{\rm mm}^{\rm NA} \mathbf{H}_{\rm inc}^{\rm o} = \epsilon_0 \alpha_{\rm ee}^{\rm NA} \mathbf{H}_{\rm inc}^{\rm o}$, which is satisfied when $\alpha_{\rm ee}^{\rm NA} = \epsilon_0 \alpha_{\rm mm}^{\rm NA}$. This means that dipole moments of a chiral NA satisfy $\mathbf{m}_{\rm NA} = \mp ic_0 \mathbf{p}_{\rm NA}$ when (i) $\alpha_{\rm ee}^{\rm NA} = \epsilon_0 \alpha_{\rm mm}^{\rm NA}$, and (ii) an optimally chiral field is used to illuminate the NA. Therefore the nearfield of a chiral NA is optimally chiral under these two conditions which are similar to conditions that an achiral NA should satisfy to generate an optically chiral scattered nearfield and far field.

So far, we have shown how to generate optimally chiral nearfields: it is required to illuminate a NA by an optimally chiral beam and that the NA has balanced electric and magnetic polarizabilities. Now, we discuss some scenarios when a dielectric NA is exposed to an external optimally chiral beam.

3.3.2 Dielectric Nanoantenna under GB Illumination

A trivial example of an optimally chiral field is a Gaussian beam (GB) with circular polarization. Under this illumination, induced electric and magnetic dipole moments in

a NA with balanced polarizabilities $\alpha_{\rm ee}^{\rm NA} = \epsilon_0 \alpha_{\rm mm}^{\rm NA}$ are transverse to the beam propagation direction and their components are related through

$$\begin{aligned} m_{{\rm NA},x} &= -c_0 p_{{\rm NA},y}, \\ m_{{\rm NA},y} &= c_0 p_{{\rm NA},x}, \\ p_{{\rm NA},y} &= i p_{{\rm NA},x} \end{aligned} \tag{3.23}$$

Equation 3.23 shows that NA is operating like a combination of two Huygens sources with a phase difference of $\pi/2$. According to Figure 3.4(b), a Si NA with radius $a = 78$nm possesses balanced polarizabilities at wavelength $\lambda = 680$nm. Now we define the helicity enhancement factor $^{|h_{\rm sca}|}/_{|h_{\rm inc}^{\rm o}|}$, which is the ratio of scattered nearfield helicity density $h_{\rm sca}$ to the helicity density of the incident field at the origin, where the NA is located. Note that normalizing scattered helicity density to that of the incident field at the position of the NA, $h_{\rm inc}^{\rm o}$, eliminates the influence of the incident field intensity from the enhancement factor $^{|h_{\rm sca}|}/_{|h_{\rm inc}^{\rm o}|}$. Since the electric $\mathbf{E}_{\rm inc}$and magnetic $\mathbf{H}_{\rm inc}$ components of the incident field satisfy $\mathbf{E}_{\rm inc} = \pm i\eta_0 \mathbf{H}_{\rm inc}$, the magnitude of helicity density of the incident field at the position of the NA reads $|h_{\rm inc}^{\rm o}| = |\mathbf{E}_{\rm inc}^{\rm o}||\mathbf{H}_{\rm inc}^{\rm o}|/(2\omega c_0)$. In Figure 3.5 (a) and (b) we show maps of scattering helicity density enhancement $|h_{\rm sca}/h_{\rm inc}^{\rm o}|$ for such Si NA in the $x-y$ and $y-z$ planes, respectively. As observed in these figures, an enhancement of an order of magnitude is achieved around the sphere at points with $\theta = \pi/2$. This figure shows that scattering helicity is evenly distributed, i.e., is azimuthally uniform around the around Si NA over 360 degrees.

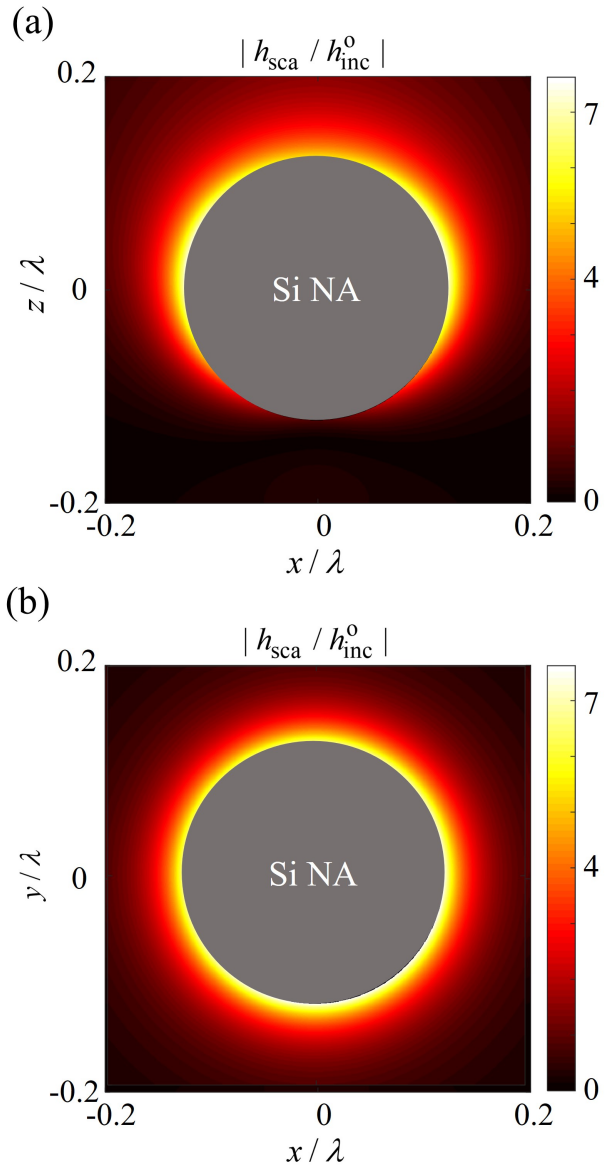

Figure 3.5: The scattering helicity enhancement distribution in the (a) $x-y$ plane, and (b) $y-z$ plane, around a Si NA with radius $a = 78$nm at the wavelength $\lambda = 680$nm.

3.3.3 Dielectric Nanoantenna under an ARPB Illumination

Here, we analyze helicity density in the nearfield of a dielectric NA when it is irradiated by an optimally chiral ARPB and induced dipole moments are oriented along the optical axis of the beam which leads to a localized helicity density along this axis. The localized helicity density may be used as a nanoprobe to detect chirality at nanoscale using circular dichroism applied to nanoparticles [7] or using photo-induced chiral force microscopy [4, 5].

We consider a situation when a spherical Si NA with polarizabilities which satisfy condition 3.19, is illuminated by an optimally chiral ARPB propagating in the $+z$ direction with half-beam waist parameter $w_0 = \lambda$. The optical axis of the beam coincides with the z-axis, and on this axis its electric and magnetic fields vectors are purely longitudinal, i.e., parallel to each other (in phasor terms), and form an optimally chiral incident field. Hence, the induced electric and magnetic dipole moments $\mathbf{p}_{\mathrm{NA}}$ and $\mathbf{m}_{\mathrm{NA}}$ in the dielectric NA are parallel to the z-axis under such an illumination, and the helicity density of the scattered nearfield, introduced in Eq. 3.17, at location (r, θ, φ) near the NA reads

$$h_{sca} \approx \frac{|E^{\mathrm{o}}_{\mathrm{inc}}|^2}{32\pi^2\omega r^6} \left(3\cos^2\theta + 1\right) \Re\left\{\alpha^{\mathrm{NA}}_{\mathrm{ee}} \left(\alpha^{\mathrm{NA}}_{\mathrm{mm}}\right)^*\right\}. \tag{3.24}$$

Consequently, the helicity enhancement due to scattered nearfield of the NA is approximated as

$$\frac{|h_{\mathrm{sca}}|}{|h^{\mathrm{o}}_{\mathrm{inc}}|} \approx \frac{1}{16\epsilon_0\pi^2 r^6}(3\cos^2\theta + 1) \left|\Re\{\alpha^{\mathrm{NA}}_{\mathrm{ee}}(\alpha^{\mathrm{NA}}_{\mathrm{mm}})^*\}\right|. \tag{3.25}$$

It is clear from Eq. 3.25 that the maximum helicity density occurs at $\theta = 0, \pi$, i.e., along

the z direction, since both moments $\mathbf{p}_{\mathrm{NA}}$and $\mathbf{m}_{\mathrm{NA}}$ are oriented along the z direction.

To investigate the influence of satisfaction of condition 3.19 and the relation between energy and helicity density enhancements in an optimally chiral nearfield around a spherical Si NA, we also define the energy enhancement ratio $u_{\mathrm{sca}}/u_{\mathrm{inc}}^{\mathrm{o}}$ as the time-averaged energy density of the scattered nearfield at a desired location with respect to that of the incident field at the origin, i.e., at the center of of the NA. Figure 3.6 (a) and (b) depict energy and helicity density enhancements. These plots show that helicity and energy density enhancements in the scattered field around the Si NA follow the same trends. Note that in Eq. 3.24 we only considered the dominant terms of the nearfield of the NA, generated by the superposition of an electric and a magnetic dipole, to provide a simple analytical formula. However the values demonstrated in Figure 3.6 (a) and (b), include all the term of the dynamic Greens function for completeness, and we note that these values are very close to those provided by the approximate formula given in Eq. 3.24.

To investigate further, using the evaluated time-averaged helicity and energy densities at the surface of the NA at $\mathbf{r} = a\hat{\mathbf{z}}$, in Figure 3.7 we plot the required radius of the NA versus excitation wavelength λ to enforce: (a) that the balance relation 3.19 leading to an optimally chiral field is satisfied [which is equivalent to having scattered nearfield satisfying the condition $|h_{\mathrm{sca}}| = u_{\mathrm{sca}}/\omega$]; (b) maximum helicity enhancement h_{max}; and (c) maximum energy density enhancement u_{max}. In all the cases the power of the incident ARPB is kept constant.

As it is clear from this figure, at each wavelength the maximum helicity and energy densities h_{max} and u_{max} do not occur at the same NA radius. Indeed, the concept of optimal chirality refers to $|h| = u/\omega$, since we know that at given frequency, $|h|$ cannot be larger than $|h| = u/\omega$. On the other hand, for other radius values, the energy density is locally increased, whereas at a given radius $|h|$ is maximum (though with $|h| < u/\omega$). This is why the two curves of maximum $|h|$ and maximum $|u|$ are close to each other. In the case of a spherical

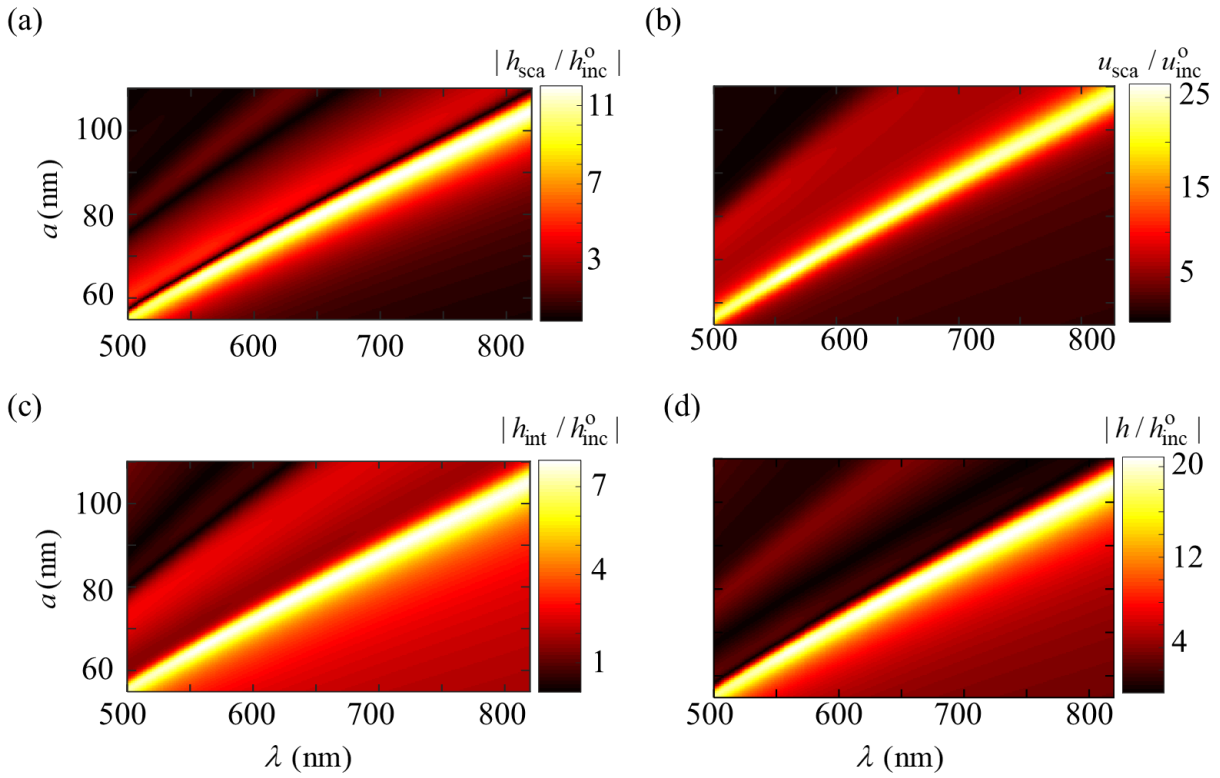

Figure 3.6: Enhancement of (a) helicity and (b) energy densities of the scattered field on the surface of a Si NA, evaluated along the $+z$ direction, i.e., at $\mathbf{r} = a\hat{\mathbf{z}}$, when illuminated by an optimally chiral ARPB propagating along the positive z direction with beam's half-waist parameter $w_0 = \lambda$. They are normalized with respect to the analogous densities of the incident ARPB evaluated at the origin. The very bright region represents the area where scattered helicity density is 11 times larger than that of the incident ARPB beam at its axis. Helicity and energy enhancements occur in regions close to each other. Interference (c) and total (d) helicity densities, both normalized to that of the incident APRB beam, evaluated at $\mathbf{r} = a\hat{\mathbf{z}}$. The maximum of total helicity density enhancement $|h/h^{o}_{inc}|$ is approximately 20. The plots also show that the interference helicity density $|h_{int}|$ in Eq.3.13 has a considerable contribution to the total helicity enhancement. That is why it is important that the interference term has the same sign of the scattered and incident helicities.

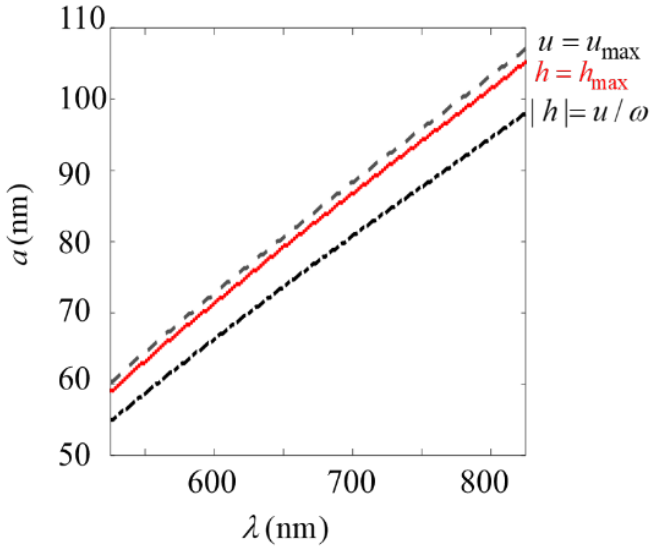

Figure 3.7: Radius of the dielectric NA that guarantees the maximum enhancement of energy density $u_{\max}$, maximum helicity density $h_{\max}$, and the "optimal chirality" condition $|h| = u/\omega$ to be satisfied, versus free space wavelength λ. In all cases the power of the incident field is kept constant. Note that for a chosen operating wavelength, the maximum of helicity enhancement, energy enhancement, and the condition $\alpha_{\text{ee}}^{\text{NA}} = \epsilon_0 \alpha_{\text{mm}}^{\text{NA}}$ (for optimal nearfield chirality) occur at different radii of the dielectric NA. Maximum helicity enhancement occurs at radial values between the other two.

dielectric NA, at the radius where the maximum of energy density enhancement occurs, condition $|h| = u/\omega$ is not precisely satisfied, which means that although the energy density of the field is enhanced considerably, helicity density does not reach its upper bound $|h| = u/\omega$. (Again, the upper bound denotes the "optimal chirality" of light). Note that the maximum helicity density $h_{\max}$ curve locates between the curve of $u_{\max}$ and that corresponding to the optimal chirality condition $|h| = u/\omega$. Moreover, the curve corresponding to optimally chiral field, i.e., $|h| = u/\omega$, does not cross the curve associated to $h_{\max}$. So far, we have discussed about helicity enhancement due to the scattering nearfield of the NA. However, the overall helicity density of the field around the NA is determined by Eq. 3.13. In the following, we discuss the importance of the interference term h_{int} [see Eq. 3.14] to total helicity enhancement. Under the balance relation $\alpha_{\text{ee}}^{\text{NA}} = \epsilon_0 \alpha_{\text{mm}}^{\text{NA}}$ for NAs and considering the optimally chiral ARPB excitation, interference helicity density in Eq. 3.14 reduces to

$$h_{\text{int}} = \frac{1}{4\pi\omega r^3} \Re \left\{ e^{ikr} \alpha_{\text{ee}}^{\text{NA}} \left[3 \left(\hat{\mathbf{r}} \cdot \mathbf{E}_{\text{inc}}^{*} \right) \left(\hat{\mathbf{r}} \cdot \mathbf{E}_{\text{inc}}^{\text{o}} \right) - \mathbf{E}_{\text{inc}}^{\text{o}} \cdot \mathbf{E}_{\text{inc}}^{*} \right] \right\}. \tag{3.26}$$

We recall that here $\mathbf{E}_{\text{inc}}$ is the incident field at location where helicity is evaluated, while $\mathbf{E}_{\text{inc}}^{\text{o}}$ is the incident field at the center of the NA.

Total helicity enhancement is given by

$$\left| \frac{h}{h_{\text{inc}}} \right| = \left| 1 + \frac{h_{\text{sca}}}{h_{\text{inc}}} + \frac{h_{\text{int}}}{h_{\text{inc}}} \right|. \tag{3.27}$$

Enhancement of both interference helicity density $|h_{\text{int}}/h_{\text{inc}}^{\text{o}}|$ and total helicity density $|h/h_{\text{inc}}^{\text{o}}|$, evaluated at the surface of the NA along the +z direction, i.e., at $\mathbf{r} = a\hat{\mathbf{z}}$, is illustrated in Figure 3.6 (c) and (d). As it is obvious from this figure, although the

enhancement contribution due to interference helicity h_{int} is weaker than that associated to the scattering field in Figure 3.6 (a) and (b), its contribution is not negligible in the total helicity enhancement and must be considered in computations and in NA engineering. It is also important to say that to maximize helicity density it is convenient to have the sign of the interference helicity density term equal to the one of the scattered and incident helicities.

Finally, three illustrative NAs with three NA radii of a =78 nm, 84, and 85 nm are considered in Figure 3.8, at the operational wavelength of $\lambda = 680$nm. These three values are chosen from Figure 3.7 because at this wavelength they, respectively, generate: (a) the optimum-chirality condition $|h| = u/\omega$, (b) the maximum enhanced total helicity $|h/h^{\text{o}}_{\text{inc}}|$, and (c) the maximum enhanced energy $u_{\text{max}}/u^{\text{o}}_{\text{inc}}$. The figure shows the distribution of the helicity densities around the dielectric NA. As it is clear, an enhancement of 20-fold in helicity density, localized at $\mathbf{r} = a\hat{\mathbf{z}}$ is achieved with a spherical dielectric NA with a radius of $a = 84$nm. Note that this value is larger than the enhancement of 10-fold obtained with the optimum-chirality condition ($|h| = u/\omega$), because at this radius $a = 84$nm one has larger energy density u, though satisfying the condition $|h| < u/\omega$. Maximum helicity enhancement occurs for a radius between that corresponding to the optimally chiral nearfield and that corresponding to maximum energy density. The radii generating maximum helicity and maximum energy density are very close to each other. Moreover, in parts (d) and (e) in Figure 3.8 we plot the helicity enhancement and the quantity hu/ω, which takes +1 for an optimally chiral ARPB with $V_{\text{A}} = iV_{\text{R}}$, around a spherical Si NA with radius a =78 nm obtained by FEM analysis in CST Studio Suite at wavelength $\lambda = 680$nm.

3.4 Conclusion

In this chapter, we investigated the helicity maximization in Guassian beams with circular polarization and azimuthally-radially polarized beams. Moreover, we presented an analysis

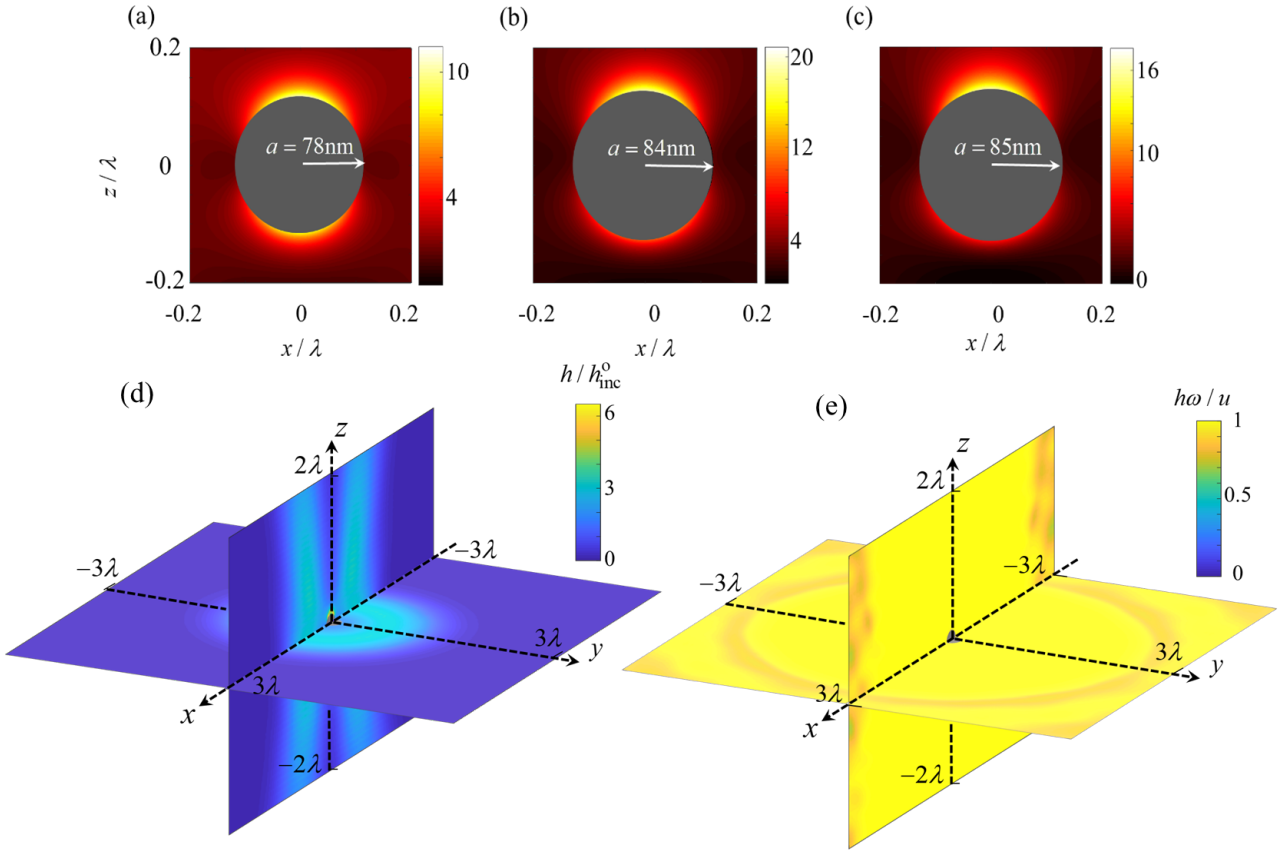

Figure 3.8: Total helicity enhancement $h/h^{\mathrm{o}}_{\mathrm{inc}}$ around a spherical Si NA in the $x-z$ plane under optimally chiral ARPB illumination with half-waist $w_0 = \lambda$, obtained by free space Green's functions and Mie scattering calculations at $\lambda = 680$nm. At this wavelength, for a dielectric NA with radius a =78 nm (a), the optimal-chirality condition $|h| = u/\omega$ is satisfied in the nearfield, whereas for a=84 nm (b) and a=85 nm (c) maximum helicity and maximum energy enhancements are obtained, respectively. Maximum helicity enhancement occurs for a radius between that corresponding to the optimally chiral nearfield and that corresponding to maximum energy density. In (d) and (e) helicity enhancement and the quantity $h\omega/u$which takes the value of +1 for an optimally chiral ARPB with $V_{\mathrm{A}} = iV_{\mathrm{R}}$ around the Si NA with radius 78 nm obtained from FEM analysis are plotted.

of helicity density in the nearfield of a dielectric achiral NA and proved that a NA with balanced electric and magnetic dipole moments, i.e., $\mathbf{m}_{\mathrm{NA}} = \pm ic_0\mathbf{p}_{\mathrm{NA}}$, generates optimally chiral scattered nearfield everywhere. To have an optimally chiral nearfield we have used an optimally chiral excitation, and under this condition, balanced electric and magnetic polarizabilities $\alpha_{\mathrm{ee}}^{\mathrm{NA}} = \epsilon_0\alpha_{\mathrm{mm}}^{\mathrm{NA}}$ guarantee that $\mathbf{m}_{\mathrm{NA}} = \pm ic_0\mathbf{p}_{\mathrm{NA}}$. The dipolar polarizabilities of a spherical high-density dielectric NA mainly satisfy this requirement when the NA's radius is chosen appropriately. Furthermore, upon illumination of a dielectric NA by an optimally chiral ARPB, which is a combination of azimuthally and radially polarized vortex beams with electric and magnetic fields with a 90 degrees phase difference and appropriate relative amplitudes, we have demonstrated that the NA's nearfield is optimally chiral, i.e., it satisfies $\mathbf{E} = \pm i\eta_0\mathbf{H}$ everywhere in space. The optimally chiral longitudinal fields of the APRB generate parallel magnetic and electric dipoles that generate optimally chiral scattered fields. We have shown that the NA's nearfield localizes helicity density below the diffraction limit and that helicity is enhanced by more than an order of magnitude compared to that of the illuminating chiral field. These findings enable possible realizations of efficient NAs for chirality characterization at nanoscale. We have observed that helicity can be enhanced even more than what is possible with the constraint of having optimally chiral field but at the expense of having higher energy density. Optimally chiral fields are important when one desires to obtain the maximum possible helicity while keeping a low electric field that could alter the specimen to be detected or even the detection scheme.

Bibliography

[1] M. Veysi, C. Guclu, and F. Capolino, "Vortex beams with strong longitudinally polarized magnetic field and their generation by using metasurfaces," *J. Opt. Soc. Am. B*, vol. 32, pp. 345–354, Feb 2015.

[2] M. Veysi, C. Guclu, and F. Capolino, "Focused azimuthally polarized vector beam and spatial magnetic resolution below the diffraction limit," *J. Opt. Soc. Am. B*, vol. 33, pp. 2265–2277, Nov 2016.

[3] J. Zeng, F. Huang, C. Guclu, M. Veysi, M. Albooyeh, H. K. Wickramasinghe, and F. Capolino, "Sharply focused azimuthally polarized beams with magnetic dominance: Near-field characterization at nanoscale by photoinduced force microscopy," *ACS Photonics*, vol. 5, no. 2, pp. 390–397, 2018.

[4] Zeng, Jinwei, Kamandi, Mohammad, Darvishzadeh-Varcheie, Mahsa, Albooyeh, Mohammad, Veysi, Mehdi, Guclu, Caner, Hanifeh, Mina, Rajaei, Mohsen, Potma, Eric O., Wickramasinghe, H.Kumar, and Capolino, Filippo, "In pursuit of photo-induced magnetic and chiral microscopy," *EPJ Appl. Metamat.*, vol. 5, p. 7, 2018.

[5] M. Kamandi, M. Albooyeh, M. Veysi, M. Rajaei, J. Zeng, H. K. Wickramasinghe, and F. Capolino, "Unscrambling structured chirality with structured light at the nanoscale using photoinduced force," *ACS Photonics*, vol. 5, no. 11, pp. 4360–4370, 2018.

[6] M. Kerker, D.-S. Wang, and C. L. Giles, "Electromagnetic scattering by magnetic spheres," *J. Opt. Soc. Am.*, vol. 73, pp. 765–767, Jun 1983.

[7] M. Hanifeh, M. Albooyeh, and F. Capolino, "Optimally chiral light: Upper bound of helicity density of structured light for chirality detection of matter at nanoscale," *ACS Photonics*, vol. 7, no. 10, pp. 2682–2691, 2020.

[8] L. D. Landau, J. S. Bell, M. J. Kearsley, L. P. Pitaevskii, E. M. Lifshitz, and J. B. Sykes, *Electrodynamics of Continuous Media*. Elsevier, 2013.

[9] A. Alù and N. Engheta, "The quest for magnetic plasmons at optical frequencies," *Opt. Express*, vol. 17, pp. 5723–5730, Mar 2009.

[10] S. Campione, C. Guclu, R. Ragan, and F. Capolino, "Enhanced magnetic and electric fields via fano resonances in metasurfaces of circular clusters of plasmonic nanoparticles," *ACS Photonics*, vol. 1, no. 3, pp. 254–260, 2014.

[11] M. Darvishzadeh-Varcheie, C. Guclu, and F. Capolino, "Magnetic nanoantennas made of plasmonic nanoclusters for photoinduced magnetic field enhancement," *Phys. Rev. Applied*, vol. 8, p. 024033, Aug 2017.

[12] C. Guclu, M. Veysi, and F. Capolino, "Photoinduced magnetic nanoprobe excited by an azimuthally polarized vector beam," *ACS Photonics*, vol. 3, no. 11, pp. 2049–2058, 2016.

[13] M. Rahmani, E. Yoxall, B. Hopkins, Y. Sonnefraud, Y. Kivshar, M. Hong, C. Phillips, S. A. Maier, and A. E. Miroshnichenko, "Plasmonic nanoclusters with rotational symmetry: Polarization-invariant far-field response vs changing near-field distribution," *ACS Nano*, vol. 7, no. 12, pp. 11138–11146, 2013. PMID: 24187975.

[14] V. Ponsinet, P. Barois, S. M. Gali, P. Richetti, J. B. Salmon, A. Vallecchi, M. Albani, A. Le Beulze, S. Gomez-Grana, E. Duguet, S. Mornet, and M. Treguer-Delapierre,

"Resonant isotropic optical magnetism of plasmonic nanoclusters in visible light," *Phys. Rev. B*, vol. 92, p. 220414, Dec 2015.

[15] S. Mühlig, A. Cunningham, S. Scheeler, C. Pacholski, T. Bürgi, C. Rockstuhl, and F. Lederer, "Self-assembled plasmonic core-shell clusters with an isotropic magnetic dipole response in the visible range," *ACS Nano*, vol. 5, no. 8, pp. 6586–6592, 2011. PMID: 21714523.

[16] C. R. Simovski and S. A. Tretyakov, "Model of isotropic resonant magnetism in the visible range based on coreshell clusters," *Phys. Rev. B*, vol. 79, p. 045111, Jan 2009.

[17] A. Vallecchi, M. Albani, and F. Capolino, "Collective electric and magnetic plasmonic resonances in spherical nanoclusters," *Opt. Express*, vol. 19, pp. 2754–2772, Jan 2011.

[18] A. García-Etxarri and J. A. Dionne, "Surface-enhanced circular dichroism spectroscopy mediated by nonchiral nanoantennas," *Phys. Rev. B*, vol. 87, p. 235409, Jun 2013.

[19] C.-S. Ho, A. Garcia-Etxarri, Y. Zhao, and J. Dionne, "Enhancing enantioselective absorption using dielectric nanospheres," *ACS Photonics*, vol. 4, no. 2, pp. 197–203, 2017.

[20] K. D. and G. P., *Dielectric Resonators*. Artech House, Norwood, MA, 1986.

[21] D. Permyakov, I. Sinev, D. Markovich, P. Ginzburg, A. Samusev, P. Belov, V. Valuckas, A. I. Kuznetsov, B. S. Luk'yanchuk, A. E. Miroshnichenko, D. N. Neshev, and Y. S. Kivshar, "Probing magnetic and electric optical responses of silicon nanoparticles," *Applied Physics Letters*, vol. 106, no. 17, p. 171110, 2015.

[22] D. E. Aspnes and A. A. Studna, "Dielectric functions and optical parameters of si, ge, gap, gaas, gasb, inp, inas, and insb from 1.5 to 6.0 ev," *Phys. Rev. B*, vol. 27, pp. 985–1009, Jan 1983.

[23] C. F. Bohren and D. R. Huffman, *Absorption and Scattering of Light by Small Particles*. 1998.

Chapter 4

Chirality Characterization at Nanoscale

Based upon the helicity maximization concept introduced in Chapter 2, here we present a platform for the detection of chirality of an individual nanoparticle (NP). We present in details a theoretical platform to characterize, i.e., to determine, the exact strength of optical chirality of an individual NP by utilizing the dissymmetry factor g [1], assuming the chiral NP interacts with an electromagnetic field not necessarily made of circularly polarized light. We consider monochromatic fields with time dependence $e^{-i\omega t}$ where ω is the angular frequency.

It has been shown that it is possible to determine chirality of an individual NP by probing two extinction powers when the NP interacts, in two different experiments, with two circularly polarized plane waves with opposite handedness, and utilize them to calculate

the dissymmetry factor defined as [2, 1]

$$g = \frac{\Delta P_{\text{ext}}}{\bar{P}_{\text{ext}}}. \tag{4.1}$$

Here, $\bar{P}_{\text{ext}} = (P^{+}_{\text{ext}} + P^{-}_{\text{ext}})/2$ and $\Delta P_{\text{ext}} = P^{+}_{\text{ext}} - P^{-}_{\text{ext}}$ are, respectively, the arithmetic average and difference of the two extinction powers in the two experiments.

Plane waves with circular polarization are the simplest example of optimally chiral fields. However, it is convenient to broaden available tools for chirality detection when dealing with NPs with weak chirality by using structured light of both beams and nanoantennas (NAs). Therefore, with the goal of enhancing the possibility of chirality detection of NPs, we propose optimally chiral structured light configurations with localized energy and helicity. We prove that helicity maximization enables the generalization of the applicability of the dissymmetry factor g to general structured light illumination for the characterizing of chirality of NPs. In general terms, we consider a NP interacting with two different excitations (not necessarily CP) with electric $\mathbf{E}^{\pm}$ and magnetic $\mathbf{H}^{\pm}$ fields denoted by superscripts + and −. The notation with the + and signs is convenient since the two experiments have to be conducted with structured lights having helicity with opposite signs. Indeed, the power dissipated in a chiral medium depends on the sign of helicity density (see Chapter 2 in this dissertation for more detail).

Without loss of generality, the NP is assumed to be isotropic and is modeled by the induced electric and magnetic dipole moments $\mathbf{p}$ and $\mathbf{m}$, related to local electric and magnetic local fields through the linear relations $\mathbf{p} = \alpha_{\text{ee}}\mathbf{E} + \alpha_{\text{em}}\mathbf{H}$ and $\mathbf{m} = \alpha_{\text{me}}\mathbf{E} + \alpha_{\text{mm}}\mathbf{H}$ (see Ref. [3]). Here α_{ee}, α_{mm}, and α_{me}, are, respectively, the electric, magnetic, and magnetoelectric polarizabilities. The term α_{em} indicates the NP's chirality, and due to reciprocity $\alpha_{\text{me}} = -\mu_0^{-1}\alpha_{\text{em}}$. The extinction powers in the two experiments are given

by [4] $P_{\text{ext}}^{\pm} = \omega\Im\left\{\mathbf{p}^{\pm}\cdot(\mathbf{E}^{\pm})^{*} + \mu_0\mathbf{m}^{\pm}\cdot(\mathbf{H}^{\pm})^{*}\right\}/2$. By using the time-averaged electric energy $u_{\text{e}}^{\pm} = \epsilon_0|\mathbf{E}^{\pm}|^2/4$, magnetic energy $u_{\text{m}}^{\pm} = \mu_0|\mathbf{H}^{\pm}|^2/4$, and helicity densities $h^{\pm} = \Im\{\mathbf{E}^{\pm}\cdot(\mathbf{H}^{\pm})^{*}\}/(2\omega c_0)$ for the fields in the two experiments, the extinction power expressions reduce to $P_{\text{ext}}^{\pm} = 2\epsilon_0^{-1}\omega\Im\left\{\alpha_{\text{ee}}\right\}u_{\text{e}}^{\pm} + 2\omega\Im\left\{\alpha_{\text{mm}}\right\}u_{\text{m}}^{\pm} - 2c_0\omega^2\Re\left\{\alpha_{\text{em}}\right\}h^{\pm}$. We recall that our goal is to determine the chirality parameter $\Re\left\{\alpha_{\text{em}}\right\}$.

Now, by defining the differences $\Delta u_{\text{e}} = u_{\text{e}}^{+} - u_{\text{e}}^{-}$, $\Delta u_{\text{m}} = u_{\text{m}}^{+} - u_{\text{m}}^{-}$, and $\Delta h = h^{+} - h^{-}$, the differential extinction ΔP_{ext} reads

$$\Delta P_{\text{ext}} = 2\omega\epsilon_0^{-1}\Im\left\{\alpha_{\text{ee}}\right\}\Delta u_{\text{e}} + 2\omega\Im\left\{\alpha_{\text{mm}}\right\}\Delta u_{\text{m}} - 2c_0\omega^2\Re\left\{\alpha_{\text{em}}\right\}\Delta h. \tag{4.2}$$

Equation 4.2 shows that to detect the electromagnetic polarizability $\Re\left\{\alpha_{\text{em}}\right\}$, the electric and magnetic polarizabilities α_{ee} and α_{mm} should be removed from the numerator of the dissymmetry factor g in Eq. 4.1. This requires the two energy densities of fields at the NP location, in the two experiments, to be identical, i.e., they shall fulfill the condition

$$\Delta u_{\text{e}} = \Delta u_{\text{m}} = 0, \tag{4.3}$$

which means that electric and magnetic fields at the NP location are such that $|\mathbf{H}^{+}| = |\mathbf{H}^{-}|$ and $|\mathbf{E}^{+}| = |\mathbf{E}^{-}|$. Applying condition 4.3 into Eq. 4.2 leads to a concise relation between the differential extinction and the helicity density of the fields and the chirality of the NP,

and the expression reduces to

$$\Delta P_{\text{ext}} = -2c_0\omega^2 \Re\left\{\alpha_{\text{em}}\right\} \Delta h. \tag{4.4}$$

Moreover, to make the dissymmetry factor g linearly linked to the magnetoelectric polarizability α_{em}, we require to remove this polarizability from the denominator $\bar{P}_{\text{ext}}$ in Eq. 4.1 which further implies that

$$h^+ = -h^- = h. \tag{4.5}$$

Condition 4.5 also serves the goal to enhance the detection of chirality by maximizing the differential helicity density Δh, since the two fields' helicity have opposite sign. We recall that the two fields satisfy condition 4.3. For a reliable detection of chirality of a NP, the magnitude of differential extinction should be higher than the noise level measured by a measuring device in each of the two experiments. Indeed it is clear from Eq. 4.4 that for a given minimum value of measurable differential extinction $|\Delta P_{\text{ext}}|$, a higher differential helicity density implies higher sensitivity to a NP's chirality. After conditions 4.3 and 4.5 are satisfied, the dissymmetry factor g reduces to [5]

$$g = -2\eta_0^{-1} \frac{\omega\, h}{u_{\text{e}}} \frac{\Re\left\{\alpha_{\text{em}}\right\}}{\Im\left\{\alpha_{\text{ee}}\right\}}. \tag{4.6}$$

for NPs with negligible magnetic properties, i.e., with $\alpha_{\text{mm}} \approx 0$, where $u_{\text{e}} = u_{\text{e}}^+ = u_{\text{e}}^-$. Now, assuming the two electromagnetic fields with opposite helicities are also "optimally chiral",

i.e., they reach that upper helicity bound $|h| = 2u_{\mathrm{e}}/\omega$, in Eq.4.6 the term $\omega h/u_{\mathrm{e}} = 2$, and the dissymmetry factor g reduces to $g = -(4/\eta_0)\,\Re\{\alpha_{\mathrm{em}}\}/\Im\{\alpha_{\mathrm{ee}}\}$. This means that the detection of the NP's normalized chirality is simply given by

$$\Re\{\alpha_{\mathrm{em}}\}/\Im\{\alpha_{\mathrm{ee}}\} = -g\eta_0/4. \tag{4.7}$$

Therefore one direct consequence of the introduction of concept of helicity maximization (see Chapter 2 for more detail) is that it eliminates the need of the specific knowledge of the values of energy and helicity densities of the two fields used in the determination of a NP's chirality. (We stress one more time that this is a generalization to any structured light, and the result does not pertain only to circularly polarized light.) Since the dissymmetry factor g is obtained from conducting two experiments, Eq. 4.7 exclusively reveals the chirality of matter at nanoscale α_{em} normalized to the electric polarizability α_{ee}. The schematic description of the proposed platform is summarized in Figure 4.1. We note that according to the upper bound of helicity density introduced in this paper, the term $\omega h/u_{\mathrm{e}}$ in Eq. 4.6, takes the maximum value of ± 2. Therefore, the maximum value of dissymmetry factor g for a certain nanoparticle is equal to $-4\Re\{\alpha_{\mathrm{em}}\}/(\eta_0\Im\{\alpha_{\mathrm{ee}}\})$.

The generality of condition $|h| = u/\omega$ paves the way to conceive a variety of optimally chiral fields for chirality detection. For example, in Chapter 2 we have demonstrated that a nontrivial optimally chiral field is generated by the ARPB with $V_{\mathrm{A}} = iV_{\mathrm{R}}$, which provides intriguing applications in microscopy and spectroscopy since on its axis chiral light has both electric and magnetic fields polarized only along the z direction [6]. We note that the technique proposed in this work is designed specifically to study chirality of nanoparticles in an experimental setup and employing structured lights. Theoretical approaches have been proposed (see for example Ref. [7]) to numerically derive polarizabilities of a scatterer.

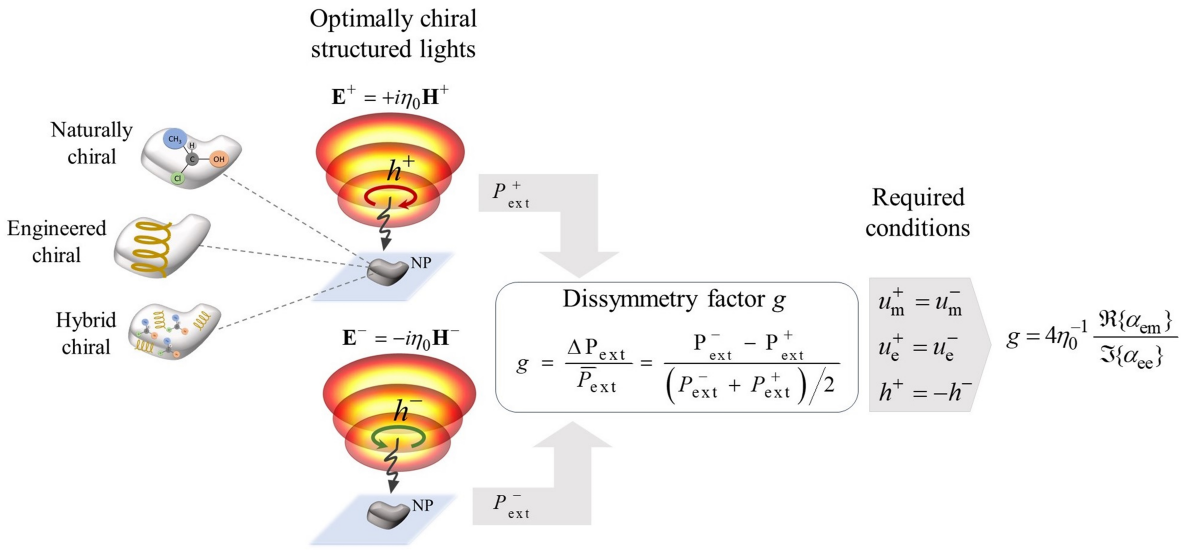

Figure 4.1: The dissymmetry factor g reveals chirality of NP, when two optimally chiral electromagnetic fields with local helicity densities with opposite signs ($h^- = -h^+$) and equal time-averaged local electric and magnetic energy densities are employed. All these assumptions strongly simplify the expression of the g factor, that now depends only on the NP polarizability. This result is general to any structured light that satisfies the optimal chiral condition.

4.1 Feasibility of the Proposed Platform for Chirality Characterization

We have presented a platform for chirality characterization of NPs by employing structured light and the dissymmetry factor g. The feasibility of the proposed platform is restricted by the minimum detectable power of detectors, since obtaining the dissymmetry factor g requires measuring extinction powers of the NP in two experiments and acquiring their difference. Indeed, considering excitations which satisfy conditions 4.3 and 4.5, the differential extinction ΔP_{ext} reads

$$\Delta P_{\text{ext}} = -4\omega^2 c_0 h \Re\{\alpha_{\text{em}}\}, \tag{4.8}$$

where $h^+ = h$and $h^- = -h$ are the helicity densities of the two excitations. For a reliable chirality characterization, the differential extinction ΔP_{ext} should exceed the minimum detectable power of the detector P_{min}, i.e., $|\Delta P_{\text{ext}}| > P_{\text{min}}$. Weak chirality of NPs and helicity density of electromagnetic fields, and limited detectability of detectors make chirality characterization of NPs challenging. Considerable efforts made to improve sensitivity of detectors to sense even a single photon [8], and highly sensitive detectors can be conveniently used for the characterization of weak electromagnetic polarizability.

Here, we investigate the role of sensitivity of detectors in chirality characterization of NPs. To that end, from Eq. 4.8 we define a minimum detectable electromagnetic polarizability $|\Re\{\alpha_{\text{em}}\}|_{\text{min}}$ as

$$|\Re\{\alpha_{\text{em}}\}|_{\text{min}} = \frac{P_{\text{min}}}{4\omega^2 c_0 h f} \tag{4.9}$$

in an experiment where a typical detector with a minimum detectable power P_{min} and an NP's excitation with helicity density h are employed. Here, $0 < f < 1$ represents the portion of the extinction power of the NP which reaches the detector and is truly measured by the detector and indicates experimental challenges. Chirality of a NP is detectable when $|\Re\{\alpha_{\text{em}}\}| > |\Re\{\alpha_{\text{em}}\}|_{\text{min}}$. Note that the ability to have higher helicity of the illuminating fields decreases the minimum amount of electromagnetic polarizability that can be detected. To provide an insight on the values of electromagnetic polarizability of NPs, we consider a spherical NP with radius a and composed of an isotropic chiral material, i.e., poly-L-glutamic acid (PGA). The real and imaginary parts of the chirality parameter κ used in the calculation of the polarizabilities of Poly-L-Glutamatic acid spherical particles are obtained from Appendix B of Ref. [9] (Figure 4.2). The rotatory strength and linewidth of the absorption bands in the Drude models assumed for $n = (n_+ + n_-)/2$ and $\Delta n = n_+ - n_-$ are

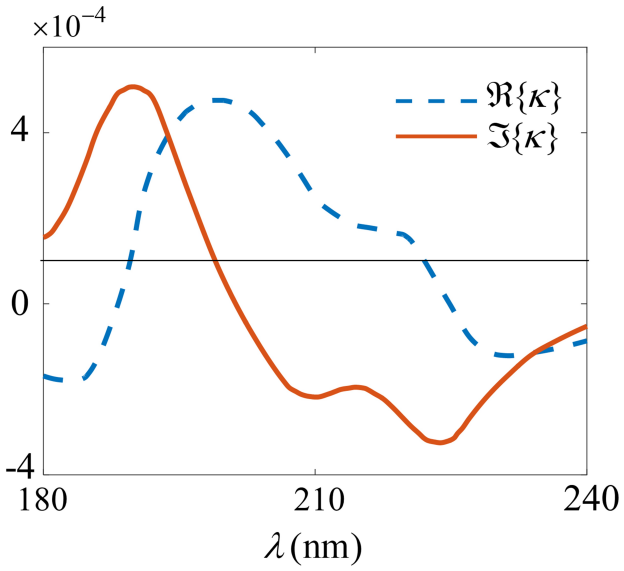

Figure 4.2: Real and imaginary parts of the chirality parameter κ of poly-L-glutamic acid (PGA). This data is used in the evaluation of the electromagnetic polarizability of a nanosphere made of such material in this chapter.

calculated to fit the experimental data of n_- and n_+ in Ref. [10]. Note that n_- and n_+ are the two refractive indices of circularly polarized (CP) light in a PGA medium corresponding to right and left handed circular polarizations. The chirality parameter κ in the constitutive relations $\mathbf{D} = \epsilon\mathbf{E} + i\kappa\sqrt{\mu_0\epsilon_0}\mathbf{H}$ and $\mathbf{B} = \mu\mathbf{H} - i\kappa\sqrt{\mu_0\epsilon_0}\mathbf{E}$ describes the bulk material made of PGA [11]. The chirality parameter κ and the refractive index $\sqrt{\epsilon\mu/\epsilon_0\mu_0}$ are related to the CP refractive indices as

$$\begin{aligned} \kappa &= \tfrac{n_+ - n_-}{2} \\ \sqrt{\tfrac{\epsilon\,\mu}{\epsilon_0\mu_0}} &= \tfrac{n_+ + n_-}{2}. \end{aligned} \tag{4.10}$$

The electric, magnetic, and electromagnetic polarizabilities α_{ee}, α_{mm}, and α_{em} for a spherical chiral nanoparticle made of PGA are calculated (see Appendix A for more detail) using the formulas for the b_1, a_1, and c_1 coefficients at page 15 in Chapter III of Bohren's PhD Thesis

[9], as

$$\begin{aligned} \alpha_{\mathrm{ee}} &= -\tfrac{6\pi i}{k^3}\epsilon_0 b_1, \\ \alpha_{\mathrm{mm}} &= -\tfrac{6\pi i}{k^3} a_1, \\ \alpha_{\mathrm{em}} &= -\tfrac{6\pi i}{k^3} c_0 c_1, \end{aligned} \tag{4.11}$$

where c_0 is the speed of light in vacuum and $k = \omega/c_0$. (Note that contrarily to a common notation, following Bohern's Thesis one has $\alpha_{\mathrm{ee}} \propto b_1$ and not $\alpha_{\mathrm{ee}} \propto a_1$, i.e., the role of the coefficients is inverted with respect to what used in several other works.) As discussed in Ref.[9], we assume that $\mu \approx \mu_0$ in the evaluation of the polarizabilities, since dissipation losses due to the magnetic permeability are smaller than the other dissipation losses, hence it is assumed that $\sqrt{\epsilon/\epsilon_0} \approx (n_+ + n_-)/2$. Alternatively, the coefficients a_1, b_1, and c_1 could also be obtained using formulas at page 18 of Bohren's PhD Thesis [9]based on Riccati-Bessel functions.

The values of the real part of Mie electromagnetic polarizability $\Re\{\alpha_{\mathrm{em}}\}$ of the spherical NP versus its radius a and wavelength λ is illustrated in Figure 4.3. This figure shows that the real part of electrozmagnetic polarizability $\Re\{\alpha_{\mathrm{em}}\}$ takes higher values for larger nanoparticles, and it takes very small values for nanoparticles with radius smaller than 8 nm. Therefore, one may infer that chirality is difficult to be detected in NPs with radii smaller than 8 nm.

Next, in Figure 4.4 we determine the range of radii of the spherical chiral NP and at each wavelength its electromagnetic polarizability is detectable, i.e, when $|\Re\{\alpha_{\mathrm{em}}\}| > |\Re\{\alpha_{\mathrm{em}}\}|_{\mathrm{min}}$. In our calculations, we assume ten percent of the extinction of NP truly reaches the detector i.e., $f = 0.1$. In Figure 4.4, detectable and undetectable spherical NPs made of PGA are marked with distinct colors varying the NPs radius and the wavelength of light,

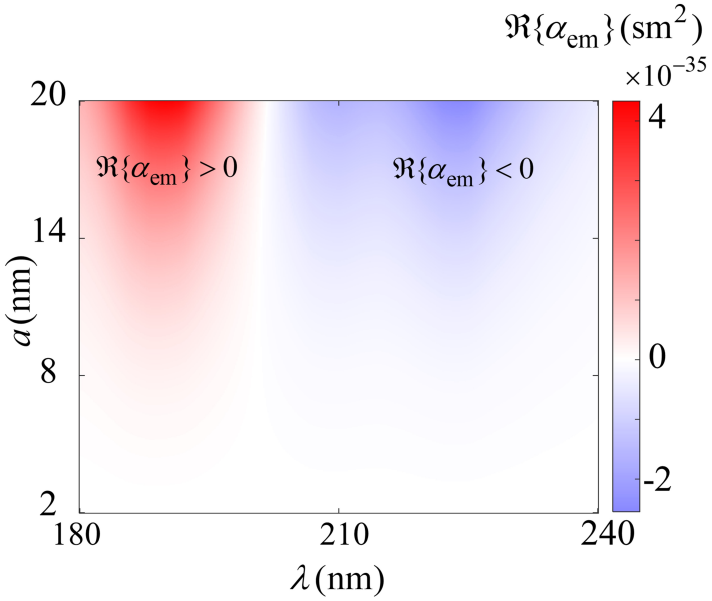

Figure 4.3: Real part of electromagnetic polarizability $\Re\{\alpha_{\text{em}}\}$calculated for a spherical chiral NP composed of poly-L-glutamic acid (PGA) versus its radius a and wavelength λ.

and it reflects the trend shown in Figure 4.3. This figure shows that practical optimally chiral fields and available detectors may reveal chirality of spherical PGA NPs with a radius as small as 7 nm when the proposed platform is used.

Note that excitation is assumed to be a circularly polarized Gaussian beam with beam parameter $w_0 = \lambda$ and total power of 1 mW, and a minimum detectable power equal to 1 fW is assumed. In Figure 4.5 (a), we illustrate the helicity density of a circularly polarized GB with total power of 1mW and beam parameter $w_0 = \lambda = 210$nm evaluated at the plane $z = 0$. This figure shows that the maximum value of the helicity density occurs on the beam's optical axis $\rho = 0$. In Figure 4.5 (b), the helicity density of the described GB at $z = \rho = 0$ is depicted for various wavelengths.

Furthermore, in part (a) of Figure 4.6, the values of the dissymmetry factor g defined in Eq. 4.1 are shown. In calculation of dissymmetry factor g all the chiral nanosphere polarizabilities α_{ee}, α_{mm}, and α_{em} are considered, thoughα_{mm} has a negligible effect. The plot of the g factor shows that the difference between the extinction powers ΔP_{ext} is a few percent of their average

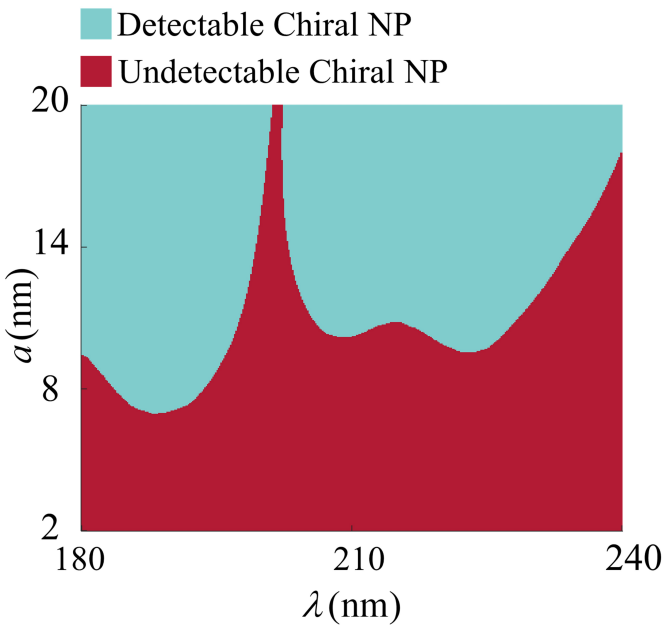

Figure 4.4: Detectable and undetectable regions for a spherical chiral NPs with radius a composed of poly-L-glutamic acid (PGA).

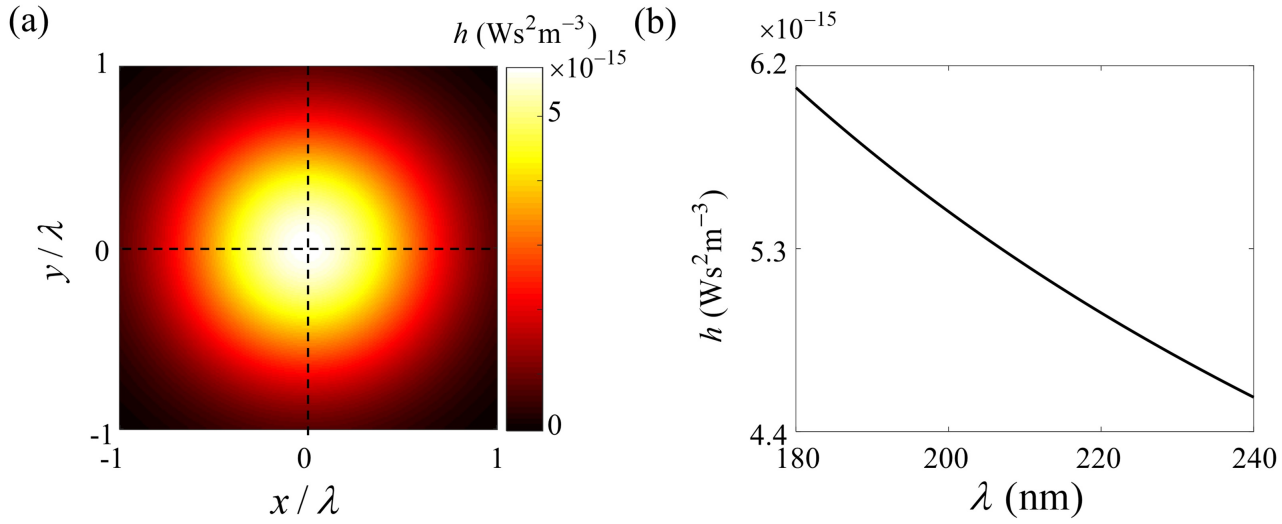

Figure 4.5: Helicity density h of a Gaussian beam with circular polarization and beam parameter $w_0 = \lambda$, propagating along the z direction, (a) in the $x - y$ plane ($z = 0$) at the operational wavelength $\lambda = 210$nm, and (b) on the optical axis at $z = \rho = 0$ versus wavelength (still $w_0 = \lambda$) . The total power of the beam is 1 mW.

which is favorable for a reliable NP's chirality detection.

We note that since light excitation considered in this calculations is optimally chiral, the dissymmetry factor g does not depend on the values of helicity and energy densities of the excitation. In other words, the use of optimally chiral light eliminates the need of the specific knowledge of the values of field's energy and helicity densities, because their values are removed from the numerator and denominator of g, i.e., $\omega h/u_{\mathrm{e}} = 2$. We recall that under these conditions, according to Eq. 4.6, the dissymmetry factor g is proportional to the real part of the electromagnetic polarizability $\Re\{\alpha_{\mathrm{em}}\}$, shown in Figure 4.3, normalized to the imaginary part of the electric polarizability of the nanoparticle. Therefore, higher values of dissymmetry factor g indicates either higher values of the real part of electromagnetic polarizability $\Re\{\alpha_{\mathrm{em}}\}$ or lower values of the imaginary part of electric polarizability $\Im\{\alpha_{\mathrm{ee}}\}$. The latter term is depicted in part (b) of Figure 4.6.

To summarize, the analysis presented here is a manifestation of feasibility of the proposed theoretical platform for chirality characterization at nanoscale. We note that our proposed technique can be extended to chirality characterization of bi-anisotropic nanoparticles with complex shape. However, a nanoparticle with a complex shape responds differently to the various components of the local field and its electric and electromagnetic polarizabilities are tensors. Therefore, special electromagnetic fields could be required for the characterization of various components of electric polarizability tensors, and this is beyond the scope of this work. We just mention that the use of an ARPB is ideal for the case of anisotropic particles because it tests the polarizability properties along one direction only (the z direction) [6], while the use of circularly polarized light senses the particle's polarizabilities in two directions (x and y) and therefore it would generate different responses based on azimuthal anisotropy. The extension of the platform presented here to the spectroscopy of anisotropic chiral nanoparticles is a good subject for future investigations.

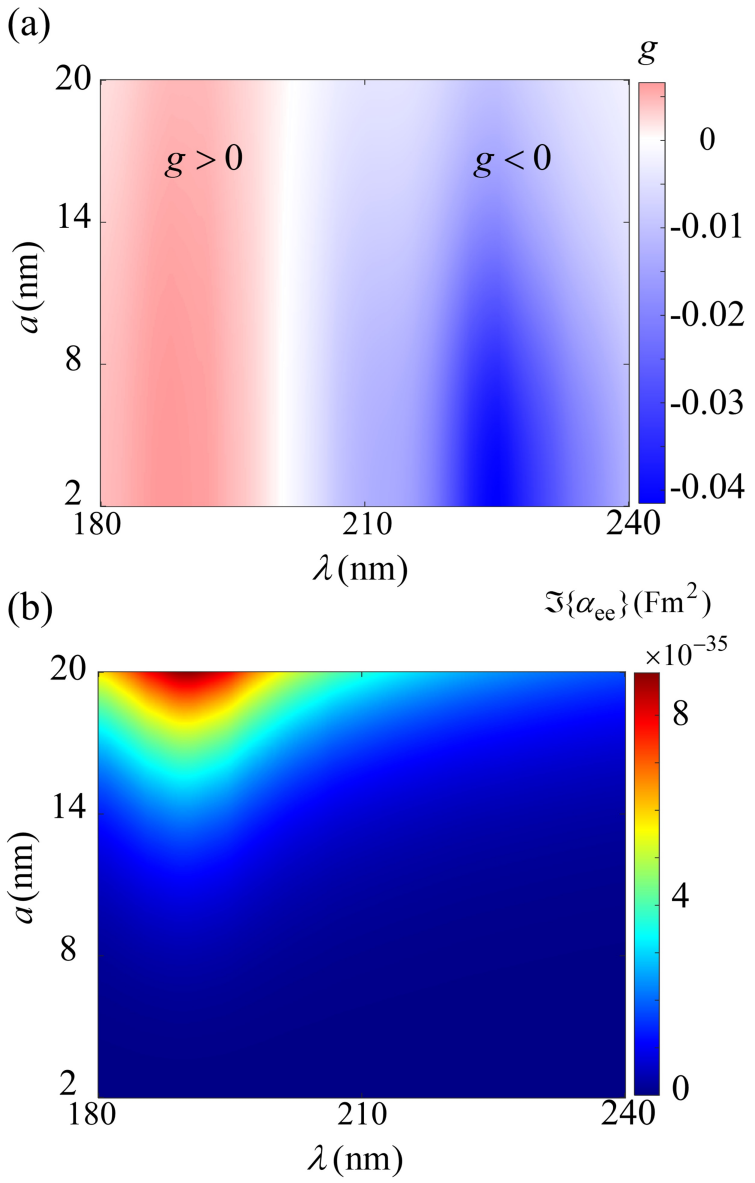

Figure 4.6: (a) Dissymmetry factor g for an individual spherical chiral NP made of poly-L-glutamic acid (PGA) with radius a. (b) Imaginary part of electric polarizability $\Im\{\alpha_{ee}\}$.

4.2 Conclusion

We have introduced the concept of helicity maximization applicable to general structured light, that defines the upper bound of helicity of light at a given local energy density. In magnitude, helicity cannot be larger than $|h| = u/\omega$. Optimally chiral light has helicity equal to its bound. It is obtainable in optical beams and from the nearfield of nanoantennas. The use of nanoantennas is particularly convenient to enhance helicity at nanoscale. Among the many choices of structured light that maximizes helicity density (CP is one of them), we have proposed the ARPB, i.e., the superposition of two special focused beams, i.e., the azimuthally polarized beam and the radially polarized beam, with a specific field ratio and a $\pm\pi/2$ phase shift. Spherical dielectric nanoantennas can generate a nearfield with maximized helicity density with helicity enhancement of about an order of magnitude. We have also discussed how to enhance helicity by just increasing the magnetic energy density while keeping the electric energy density constant (or vice versa), though this would not constitute optimal chiral light and would still be subject to the bound $|h| \leq (u_\mathrm{e} + u_\mathrm{m})/\omega$. Based on the optimal chirality concept, we have proposed a platform for the detection of chirality of nanoparticles based on any structured light, without knowing the precise values of energy and helicity densities, by measuring only two extinction powers to construct the dissymmetry factor g. We stress that the findings shown in this paper are general to any structured light, and indeed also nanoantennas can be used to enhance helicity by keeping nearfield light optimally chiral, leading to decreased minimum value of detectable chirality. In summary these findings have the capability to empower characterization of chirality at nanoscale by taking the advantage of field localization, structured light, and helicity enhancement with optimal chirality.

Bibliography

[1] W. Kuhn, "The physical significance of optical rotatory power," *Z. physik. Chem.*, 1930.

[2] Y. Tang and A. E. Cohen, "Optical chirality and its interaction with matter," *Phys. Rev. Lett.*, vol. 104, p. 163901, Apr 2010.

[3] A. Serdiukov, I. Semchenko, S. Tretyakov, and A. Sihvola, *Electromagnetics of Bi-Anisotropic Materials - Theory and Application*. Gordon and Breach Science Publishers, 2001.

[4] C. F. Bohren and D. R. Huffman, *Absorption and Scattering of Light by Small Particles*. 1998.

[5] Y. Tang and A. E. Cohen, "Enhanced enantioselectivity in excitation of chiral molecules by superchiral light," *Science*, vol. 332, no. 6027, pp. 333–336, 2011.

[6] M. Kamandi, M. Albooyeh, M. Veysi, M. Rajaei, J. Zeng, H. K. Wickramasinghe, and F. Capolino, "Unscrambling structured chirality with structured light at the nanoscale using photoinduced force," *ACS Photonics*, vol. 5, no. 11, pp. 4360–4370, 2018.

[7] M. Yazdi and N. Komjani, "Polarizability calculation of arbitrary individual scatterers, scatterers in arrays, and substrated scatterers," *J. Opt. Soc. Am. B*, vol. 33, pp. 491–500, Mar 2016.

[8] R. H. Hadfield, "Single-photon detectors for optical quantum information applications," *Nature Photonics*, vol. 3, 2009.

[9] C. F. Bohren, *Light Scattering by Optically Active Particles.* PhD thesis, THE UNIVERSITY OF ARIZONA., Aug. 1975.

[10] D. W. Urry and J. Krivacic, "Differential scatter of left and right circularlay polarized light by optically active particulate systems," *Proceedings of the National Academy of Sciences*, vol. 65, no. 4, pp. 845–852, 1970.

[11] I. Lindell, A. Sihvola, S. Tretyakov, and A. Viitanen, *Electromagnetic Waves in Chiral and Bi-Isotropic Media.* Artech House, 1994.

Chapter 5

Helicity Maximization in a Planar Array of Achiral High-density Dielectric Nanoparticles

In this chapter, we derive the required condition by an array of nanoantennas (NAs) to generate optimally chiral nearfield which represents the upper bound of obtainable helicity density with a given field energy density. We prove that to have optimally chiral nearfield in an array of nanoparticles (NPs), all array elements are required to generate optimally chiral nearfield. This condition reduces to satisfying the Kerker condition by the effective electric and magnetic polarizabilities, which we call "effective" Kerker condition, when an array of achiral nanoparticles is considered. We rigorously analyze helicity density enhancement and distribution of nearfield of an array of spherical high-density dielectric NAs (made for example of Silicon or TiO2). Importantly, each NA is isotropic and achiral and the array does not contribute to circular dichroism (CD) signal when utilized as a substrate for chiral samples. To that end, optical properties and helicity density of nearfields are, respectively, investigated in proximity of both an individual and an array of high-density NAs.

5.1 Helicity Analysis of Nearfield of a High-density Dielectric NA

As a determinant factor in the electromagnetic response of an array, we devote this section to investigate the interaction of a spherical high-density NA with electromagnetic fields. Let us assume that a spherical NA with radius a is located at the origin of the coordinate system and is irradiated by an incident field with electric and magnetic components $\mathbf{E}_{\text{inc}}$ and $\mathbf{H}_{\text{inc}}$, respectively, propagating along the $+z$ direction in free space (Figure. 5.1(a)). As a quantitative measure of the interaction between the NA and the incident field, we employ the scattering cross section of the NA denoted by σ_s, defined as the total scattered power normalized to the incident field irradiance [1]. First, we employ a full wave simulation analysis based on the finite element method (FEM) implemented in CST Microwave Studio [2] to obtain the NA's σ_s, shown in Figure. 5.1 (b), when it is irradiated by a plane wave with electric field $\mathbf{E}_{\text{inc}} = E_0 e^{ik_0 z}\hat{\mathbf{y}}$ versus wavelength within the interval of 600 nm to 800 nm, for various radii a. Here, E_0 is the complex amplitude of the electric field, and $\hat{\mathbf{x}}$ and $\hat{\mathbf{y}}$ are unit vectors of the Cartesian coordinate system. In this example in the following ones we assume that the high-density NA is made of Silicon, whose refractive index is extracted from Ref. [3].

To elaborate the essence of the interaction, we model the NA by induced electric $\mathbf{p}$ and magnetic $\mathbf{m}$ dipole moments and neglect the contributions from higher multipoles in the scattering. Such an approximate modeling is valid as long as the NA is optically small and has been widely used in metasurface design and analysis [4, 5]. The dipole moments are

related to the incident field $\mathbf{E}^{\mathrm{o}}_{\mathrm{inc}}$ and $\mathbf{H}^{\mathrm{o}}_{\mathrm{inc}}$ at the position of the NA through

$$\begin{aligned} \mathbf{p} &= \alpha_{\mathrm{ee}}\mathbf{E}^{\mathrm{o}}_{\mathrm{inc}}, \\ \mathbf{m} &= \alpha_{\mathrm{mm}}\mathbf{H}^{\mathrm{o}}_{\mathrm{inc}}. \end{aligned} \tag{5.1}$$

Here, α_{ee} and α_{mm} are electric and magnetic polarizabilities that are here evaluated using Mie theory. (For the sake of clarity, the magnetic dipole is defined here as $\mathbf{m} = \frac{1}{2}\int \mathbf{r} \times \mathbf{J}(\mathbf{r})dv$ where $\mathbf{J}(\mathbf{r})$ represents the displacement current density.) In Figure. 5.1 (b), we plot also the scattering cross section of a spherical NA with radius $a = 85$ nm calculated using only the induced electric and magnetic dipoles (continuous orange curve) showing that this representation leads to a good approximation. In what follows, without loss of generality we focus on a NA with radius $a = 85$ nm made of Silicon with the peak of scattering cross section σ_s occurring at wavelength $\lambda = 675$nm which is almost in the middle of the considered wavelength range.

The magnitudes of electric and magnetic dipole polarizabilities of a NA with radius $a = 85$ nm, and their phase difference $\Delta\varphi$ are calculated using the expressions from Mie theory and are plotted in Figure. 5.2. This figure shows that at $\lambda = 730$nm the electric and magnetic polarizabilities are approximately balanced, i.e., when $|\alpha_{\mathrm{ee}}|/\epsilon_0 = |\alpha_{\mathrm{mm}}|$ and their phase difference $\Delta\varphi$ is very close to zero, which means that the Kerker condition [6] is almost satisfied at that wavelength and hence the NA directs the scattered field in the forward direction (a source with zero back radiation is often referred to as Huygens source). The peak of α_{mm} at wavelength λ =675nm is often referred to as "magnetic resonance" of the NA.

This result indicates that an array composed of NAs with radius $a = 85$ nm (to be investigated later in this paper) would mainly transmit all the incident power at λ=730 nm which is advantageous when transmitted power is employed to detect chirality in accordance to

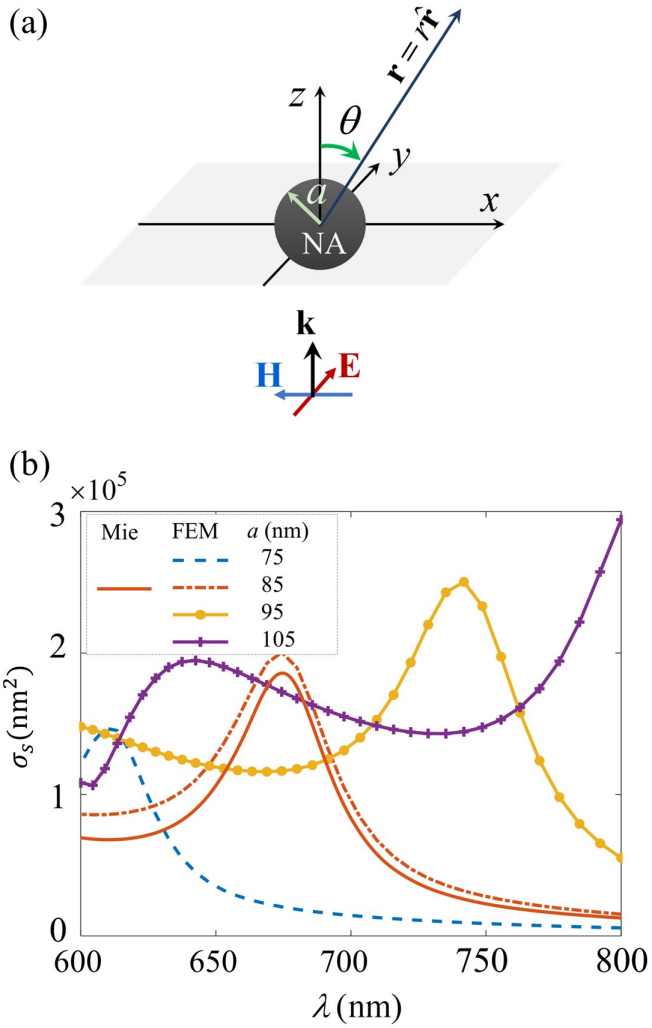

Figure 5.1: (a) High-density dielectric nanoantenna (NA) with radius a located at the origin of a coordinate system and illuminated by a plane wave. (b) Scattering cross section σ_s of the NA versus operating wavelength λ for four distinct sphere's radii. In this example and in all the following ones the NA is made of Silicon. As it will be clear in the next figure, the peaks represent magnetic resonances.

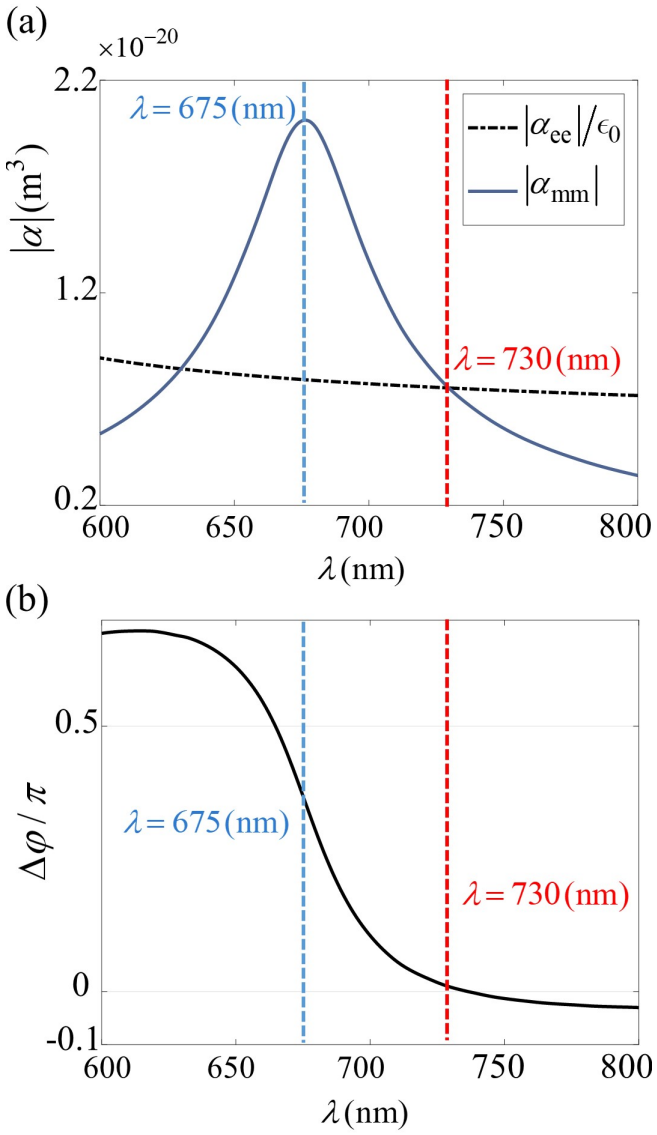

Figure 5.2: (a) Magnitude and (b) normalized phase difference between of the electric α_{ee} and magnetic α_{mm} dipole polarizabilities of a single NA with radius a=85 nm made of Silicon. At $\lambda = 730$nm, the Kerker condition [6] is approximately satisfied, i.e., the balanced polarizabilities very closely satisfy $|\alpha_{\text{ee}}|/\epsilon_0 = |\alpha_{\text{mm}}|$ and $\Delta\varphi = 0$.

standard circular dichroism experiments. However, coupling among the NAs (and a possible phase difference between incident and scattered fields) would cause a wavelength shift for maximum transmittance to occur.

Since the upper bound of helicity density is linearly linked to the energy density as was shown in Chapter 2 in this dissertation, to have optimally chiral nearfield with maximized helicity density, it is required to simultaneously enhance electric and magnetic energy densities. However, according to Eq. 5.1, the induced electric **p** and magnetic **m** dipole moments are, respectively, oriented along the y and x axes when the NA is illuminated by y-polarized (electric field) plane wave. Therefore, electric energy density is enhanced more effectively along the y axis while the maximum of magnetic energy density occurs along the x axis. In the following section, we analyze helicity density of the total nearfield of a NA illuminated by a plane wave with circular polarization.

5.1.1 Optimally Chiral Nearfield of an Array Element

We illuminate a single NA made of Si with radius a=85 nm by a left-handed circularly polarized plane wave with electric field $\mathbf{E}_{\text{inc}}$ represented as

$$\mathbf{E}_{\text{inc}} = E_0(\hat{\mathbf{x}} + i\hat{\mathbf{y}})e^{ik_0 z}/\sqrt{2}, \tag{5.2}$$

propagating along the $+z$ axis and magnetic field $\mathbf{H}_{\text{inc}} = (E_0/\eta_0)(\hat{\mathbf{y}} - i\hat{\mathbf{x}})e^{ik_0 z}/\sqrt{2}$ is obtained from Maxwell equation $\mathbf{H} = (i\omega\mu_0^{-1})\nabla \times \mathbf{E}$. The wavenumber in vacuum is denoted by $k_0 = \omega\sqrt{\epsilon_0\mu_0}$. Here and in the following a hat tags unit vectors. As we discussed in Chapter 3 in this dissertation, that helicity density h of the total field around a NA is the sum of the helicity density of the incident field h_{inc}, the helicity density of the scattered field h_{sca}, and

an interference helicity density h_{int}, i.e.,

$$h = h_{\text{inc}} + h_{\text{int}} + h_{\text{sca}}. \tag{5.3}$$

The sign of helicity density of the circularly polarized incident field is positive based on the definition in Eq. 5.2. Scattering helicity density h_{sca} at location $\mathbf{r} = r\hat{\mathbf{r}}$, generated by a NA in its surrounding, when the NA's scattering is represented by only dipole moments $\mathbf{p}$ and $\mathbf{m}$ is approximated by the expression

$$h_{\text{sca}} \approx \frac{\eta_0}{32\pi^2\omega r^6}\Im\left\{3(\hat{\mathbf{r}}\cdot\mathbf{p})(\hat{\mathbf{r}}\cdot\mathbf{m}^*) + \mathbf{p}\cdot\mathbf{m}^*\right\}, \tag{5.4}$$

after keeping only terms with dependence r^{-3} and ignoring those which depend on r^{-1} and r^{-2}. Introducing Eqs. 5.1 and 5.2 into Eq. 5.4 simplifies the expression of scattering helicity density h_{sca} to

$$h_{\text{sca}} \approx \frac{\epsilon_0|E_0|^2}{32\pi^2\omega r^6}\left(\frac{3}{2}\sin^2\theta + 1\right)^{\Re\mathfrak{e}\{\alpha_{\text{ee}}\alpha_{\text{mm}}^*\}/\epsilon_0}, \tag{5.5}$$

where θ is the polar angle in spherical coordinate system (r, θ, φ). Figure 5.3 shows the term $\Re\mathfrak{e}\{\alpha_{\text{ee}}\alpha_{\text{mm}}^*\}/\epsilon_0$ in Eq. 5.5 which relates the scattering helicity density to the electric and magnetic polarizabilities of the NA. Besides the slow varying $1/\omega$ term in Eq. 5.5, it is $\Re\mathfrak{e}\{\alpha_{\text{ee}}\alpha_{\text{mm}}^*\}/\epsilon_0$ that controls the maximum of the scattering helicity density. Note that helicity enhancement, i.e., normalized scattering helicity density h_{sca} to that of the incident field $h_{\text{inc}} = \epsilon_0|E_0|^2/(2\omega)$, is independent from amplitude and angular frequency of the excitation and

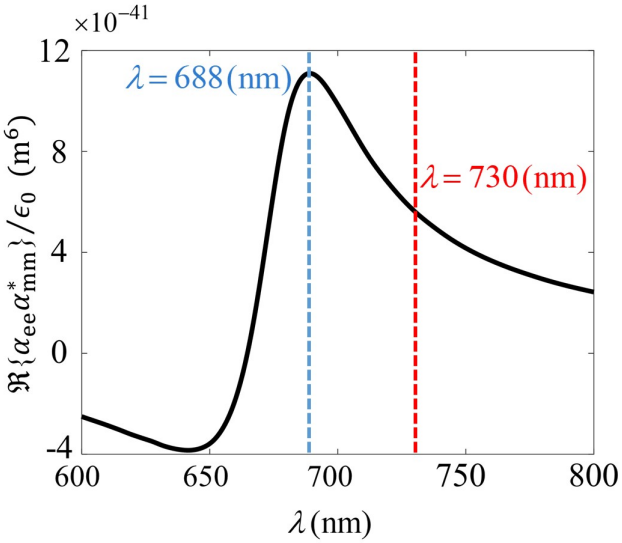

Figure 5.3: Term $\mathfrak{Re}\{\alpha_{\rm ee}\alpha^*_{\rm mm}\}/\epsilon_0$, which is proportional to $h_{\rm sca}/h_{\rm inc}$, for a single NA with radius a=85nm versus wavelength. This term takes its maximum around $\lambda = 688$nm, while it has a lower value at $\lambda = 730$ nm where polarizabilities are balanced.

is proportional to $h_{\rm sca}/h_{\rm inc} \propto {}^{\mathfrak{Re}\{\alpha_{\rm ee}\alpha^*_{\rm mm}\}}/_{\epsilon_0}$. Therefore, since this term, as depicted in Figure. 5.3, does not drop dramatically, the discussed NA provides enhanced helicity density over a wide wavelength range between 700 nm and 800 nm.

Figure 5.3 shows that the scattering helicity density generated by a NA illuminated by a plane wave with CP reaches its maximum around $\lambda = 688$nm while its value is smaller at $\lambda = 730$ nm where the two polarizabilities are balanced (when $\alpha_{\rm ee}/\epsilon_0 = \alpha_{\rm mm}$). In Chapter 3 in this dissertation, we proved that balanced polarizabilities (when $\alpha_{\rm ee}/\epsilon_0 = \alpha_{\rm mm}$) are required to generate optimally chiral field around a NA, when it is illuminated by an optimally chiral incident field satisfying condition $\mathbf{E} = \pm i\eta_0\mathbf{H}$ such as a plane wave with circular polarization. This means that the maximum of helicity density does not corresponds to the "optimal chiral condition". However, for applications which require optimally chiral fields, such as chirality characterization of nanoparticles, this condition is satisfied at expense of losing a portion of helicity enhancement. Note that as discussed earlier in this paper, balanced polarizabilities also correspond to satisfaction of Kerker condition which is advantageous for applications such as CD experiments where measuring the transmitted power through an

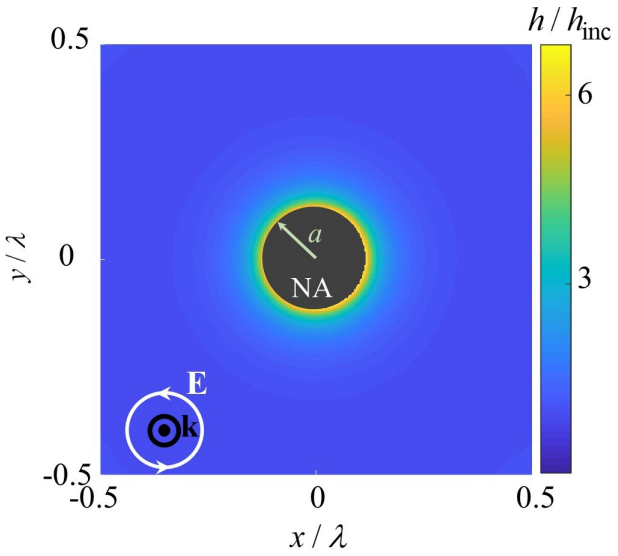

Figure 5.4: Normalized helicity density to that of the incident field around a single NA with radius a =85 nm, irradiated by a plane wave with circular polarization at λ = 730nm, in $x-y$ plane, i.e., at $\theta = \pi/2$. Since illumination has circular polarization the distribution is symmetric in the azimuthal plane.

array of discussed NAs is the goal.

Since the incident field has a left-handed circular polarization, the term h_{inc} has positive value. Therefore, incident and scattering helicity densities interfere constructively contributing to a higher total helicity density at wavelength where $^{\Re\{\alpha_{\text{ee}}\alpha^*_{\text{mm}}\}}/_{\epsilon_0}$ takes positive values. Figure 5.4 illustrates the distribution of total helicity density (of the total field), obtained from full wave simulations, normalized to that of incident field in the transverse $x-y$ plane, at λ=730 nm. According to Eq. 5.5, the helicity density of the scattered field h_{sca} drops fast with a factor of r^{-6} since it is mainly due to the nearfield. Moreover, as discussed in Chapter 2 in this dissertation, the interference helicity density h_{int}, i.e., the second term in Eq. 5.5, drops by a factor of r^{-3}. Therefore, the total helicity density enhancement defined as h/h_{inc} tends to unity as $1 + h_{\text{int}}/h_{\text{inc}} + h_{\text{sca}}/h_{\text{inc}}$ when moving away from the particle. Therefore, to provide optimally chiral nearfield with maximized helicity density over a broader area, we propose an array of NAs where the effective polarizability of each NA in the array approximately satisfies the Kerker condition in the presence of mutual

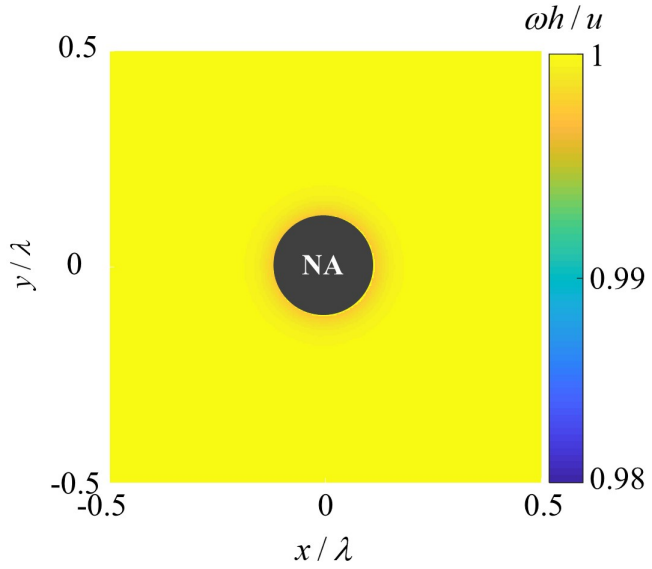

Figure 5.5: Plot of $\omega h/u$, i.e., of the product of the magnitude of helicity density and angular frequency normalized to the energy density, i.e., around a single NA with radius a=85 nm in the $x-y$ plane at wavelength $\lambda = 730$ nm. This quantity equals unity for optimally chiral fields and fields whose $\omega|h|/u$ values are close to unity are close to satisfying the required conditions to be optimally chiral.

couplings among the NAs.

5.2 Optimally Chiral Nearfield of a Planar Array of NAs

So far, we have shown that an individual achiral NA with balanced electric and magnetic polarizabilities $\alpha_{\text{ee}}/\epsilon_0 = \alpha_{\text{mm}}$ generates optimally chiral nearfield. In this section we extend this discussion to an array of NAs and determine the conditions required for an array to generate an optimally chiral nearfield over its surface. We investigate helicity density enhancement, maximization, and distribution over the surface of a planar array composed of NAs as in Figure 5.6, illuminated by a plane wave with circular polarization. Full wave simulations are carried out by using the frequency domain finite element method module in the software package CST Studio Suite by DS SIMULIA [2]. Floquet boundary conditions

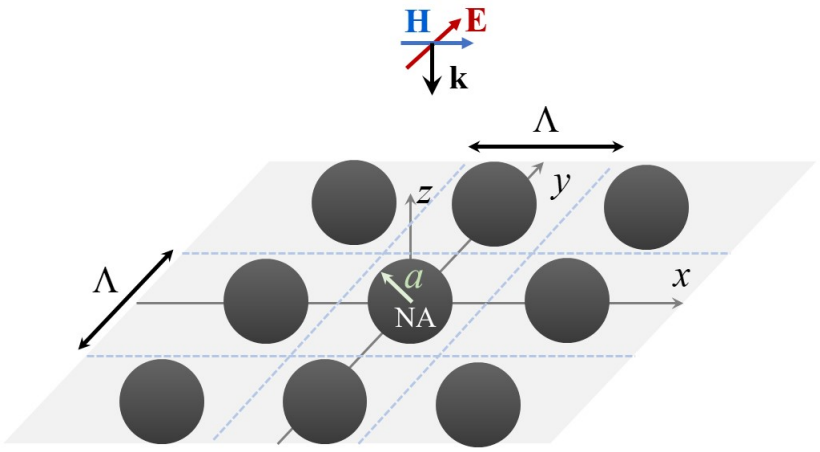

Figure 5.6: Array of NAs with radius a arranged in the $x-y$ plane with period Λ, illuminated by a plane wave, propagating along the negative z direction.

are imposed on $x-y$ boundaries of the array's unit cell and Floquet modes up to first order are considered above and below the array.

The properties of an array of NAs, located at $\mathbf{r}_{mn} = m\Lambda\hat{\mathbf{x}} + n\Lambda\hat{\mathbf{y}}$ with $m, n = 0, \pm1, \pm2, \ldots$ as that shown in Figure 5.6, are determined by the electric and magnetic polarizabilities of the NA (which are dictated by the NA's radius a) and the periodicity of the array Λ, which influences the interaction between array elements. Here we mainly examine arrays composed of NAs with radius a =85 nm considered in the previous section.

The total electric $\mathbf{E}$ and magnetic $\mathbf{H}$ fields in presence of the array of NAs are

$$\begin{aligned} \mathbf{E} &= \mathbf{E}_{\text{inc}} + \textstyle\sum_{m,n=-\infty}^{\infty} \mathbf{E}_{mn} \\ \mathbf{H} &= \mathbf{H}_{\text{inc}} + \textstyle\sum_{m,n=-\infty}^{\infty} \mathbf{H}_{mn}, \end{aligned} \tag{5.6}$$

where $\mathbf{E}_{mn}$ and $\mathbf{H}_{mn}$ are the scattered electric and magnetic fields by the NA with its center located at $\mathbf{r}_{mn}$ and they are obtained either by full wave simulations or by using dyadic Green's functions. To have an optimally chiral total nearfield in proximity of the array

plane, it is required to have: (i) an optimally chiral incident field i.e., $\mathbf{E}_{\text{inc}} = \pm i\eta_0 \mathbf{H}_{\text{inc}}$, and (ii) optimally chiral scattered field by each of array elements i.e., $\mathbf{E}_{\text{inc}} = \pm i\eta_0 \mathbf{H}_{\text{inc}}$. Indeed, under these conditions, the total electric $\mathbf{E}$ and magnetic $\mathbf{H}$ fields satisfy the relation

$$\mathbf{E} = \mathbf{E}_{\text{inc}} + \sum_{m,n=-\infty}^{\infty} \mathbf{E}_{mn} = \pm i\eta_0 \mathbf{H}_{\text{inc}} \pm \sum_{m,n=-\infty}^{\infty} i\eta_0 \mathbf{H}_{mn} = \pm i\eta_0 \mathbf{H}, \tag{5.7}$$

hence they are optimally chiral. For scattered electric and magnetic fields to satisfy $\mathbf{E}_{mn} = \pm i\eta_0 \mathbf{H}_{mn}$, it is required that electric $\mathbf{p}_{mn}$ and magnetic $\mathbf{m}_{mn}$ dipole moments induced in the mnth NA, satisfy condition

$$\mathbf{p}_{mn} = \pm \frac{i}{c_0} \mathbf{m}_{mn} \ , \quad \forall \ m, n. \tag{5.8}$$

Note that dipole moments in each NA are induced by the sum of the incident field and the scattered fields generated by all other array elements, it is possible to reduce condition 5.8 to

$$\alpha_{\text{ee}}^{\text{eff}} / \epsilon_0 = \alpha_{\text{mm}}^{\text{eff}} \tag{5.9}$$

when effective electric $\alpha_{\text{ee}}^{\text{eff}}$ and magnetic $\alpha_{\text{mm}}^{\text{eff}}$ polarizabilities are defined as

$$\begin{aligned} \mathbf{p}_{mn} &= \alpha_{\text{ee}}^{\text{eff}} \mathbf{E}_{\text{inc}}^{\text{o}} \\ \mathbf{m}_{mn} &= \alpha_{mm}^{\text{eff}} \mathbf{H}_{\text{inc}}^{\text{o}}. \end{aligned} \tag{5.10}$$

The two effective polarizabilities of each NA arranged in an array are here calculated by employing Green's functions [7, 8]. To calcualate the effective polarizabilities, we assume that electric $\mathbf{p}_{mn}$ and magnetic $\mathbf{m}_{mn}$ array dipole moments induced in the arrayed NAs with electric α_{ee} and magnetic α_{mm} polarizabilities located at $\mathbf{r}_{mn}$ are obtained as

$$\begin{aligned} \mathbf{p}_{mn} &= \alpha_{\mathrm{ee}} \mathbf{E}_{\mathrm{loc}}\left(\mathbf{r}_{mn}\right) \\ \mathbf{m}_{mn} &= \alpha_{\mathrm{mm}} \mathbf{H}_{\mathrm{loc}}\left(\mathbf{r}_{mn}\right), \end{aligned} \tag{5.11}$$

where $\mathbf{E}_{\mathrm{loc}}\left(\mathbf{r}_{mn}\right)$ and $\mathbf{H}_{\mathrm{loc}}\left(\mathbf{r}_{mn}\right)$ are local electric and magnetic fields at the location of the mnth NA. Since the array is illuminated by a normally incident field, the electric and magnetic dipole moments in the array elements are all equal. Let us consider the reference NA at the origin of the coordinate with the local electric and magnetic fields

$$\begin{aligned} \mathbf{E}_{\mathrm{loc}}\left(\mathbf{r}_{00}\right) &= \mathbf{E}_{\mathrm{inc}}^{\mathrm{o}} + \check{\underline{\mathbf{G}}}_{\mathrm{ee}}\left(\mathbf{r}_{00}, \mathbf{r}_{00}\right) \cdot \mathbf{p}_{00}, \\ \mathbf{H}_{\mathrm{loc}}\left(\mathbf{r}_{00}\right) &= \mathbf{H}_{\mathrm{inc}}^{\mathrm{o}} + \check{\underline{\mathbf{G}}}_{\mathrm{mm}}(\mathbf{r}_{00}, \mathbf{r}_{00}) \cdot \mathbf{m}_{00}, \end{aligned} \tag{5.12}$$

where $\check{\underline{\mathbf{G}}}_{\mathrm{ee}}\left(\mathbf{r}_{00}, \mathbf{r}_{00}\right)$ and $\check{\underline{\mathbf{G}}}_{\mathrm{mm}}(\mathbf{r}_{00}, \mathbf{r}_{00})$ are the "regularized" dyadic Green's function that accounts for the field contributions produced by all the NAs except the one located at $\mathbf{r}_{00}$ as explained in Refs. [7, 8]. Note that the electric and magnetic fields produced, respectively, by magnetic and electric dipole moments disappear due to the symmetry of the structure and its illumination. After substituting 5.12 into 5.11 and some algebraic manipulations, the induced dipole moments are obtained as

$$\begin{aligned} \mathbf{p}_{00} &= \alpha_{\mathrm{ee}} \left[\underline{\mathbf{I}} - \alpha_{\mathrm{ee}} \check{\underline{\mathbf{G}}}_{\mathrm{ee}}\left(\mathbf{r}_{00}, \mathbf{r}_{00}\right)\right]^{-1} \cdot \mathbf{E}_{\mathrm{inc}}^{\mathrm{o}} \\ \mathbf{m}_{00} &= \alpha_{\mathrm{mm}} \left[\underline{\mathbf{I}} - \alpha_{\mathrm{mm}} \check{\underline{\mathbf{G}}}_{\mathrm{mm}}\left(\mathbf{r}_{00}, \mathbf{r}_{00}\right)\right]^{-1} \cdot \mathbf{H}_{\mathrm{inc}}^{\mathrm{o}} \end{aligned} \tag{5.13}$$

where $\underline{\mathbf{I}}$ is the identity dyadic. Therefore, the effective polarizabilities are defined as

$$\begin{aligned}
\underline{\alpha}_{\mathrm{ee}}^{\mathrm{eff}} &= \alpha_{\mathrm{ee}} \left[\underline{\mathbf{I}} - \alpha_{\mathrm{ee}} \underline{\check{\mathbf{G}}}_{\mathrm{ee}} \left(\mathbf{r}_{00}, \mathbf{r}_{00}\right)\right]^{-1}, \\
\underline{\alpha}_{\mathrm{mm}}^{\mathrm{eff}} &= \alpha_{\mathrm{mm}} \left[\underline{\mathbf{I}} - \alpha_{\mathrm{mm}} \underline{\check{\mathbf{G}}}_{\mathrm{mm}} \left(\mathbf{r}_{00}, \mathbf{r}_{00}\right)\right]^{-1},
\end{aligned} \tag{5.14}$$

Since the planar array has a square lattice, i.e., its periodicity along x and y directions are equal, only the diagonal components $\check{G}_{\mathrm{ee},xx} = \check{G}_{\mathrm{ee},yy}$, $\check{G}_{\mathrm{mm},xx} = \check{G}_{\mathrm{mm},yy}$, $\check{G}_{\mathrm{ee},zz}$, and $\check{G}_{\mathrm{mm},zz}$of the Dyadic Green's functions shall be considered. Moreover, for a normally incident plane wave, only $\alpha_{\mathrm{ee,xx}}^{\mathrm{eff}}$, $\alpha_{\mathrm{ee,yy}}^{\mathrm{eff}}$, $\alpha_{\mathrm{mm,xx}}^{\mathrm{eff}}$, and $\alpha_{\mathrm{mm,yy}}^{\mathrm{eff}}$ are excited. Hence, the effective polarizabilities simplify to

$$\begin{aligned}
\underline{\alpha}_{\mathrm{ee}}^{\mathrm{eff}} &= \alpha_{\mathrm{ee}}^{\mathrm{eff}} (\hat{\mathbf{x}}\hat{\mathbf{x}} + \hat{\mathbf{y}}\hat{\mathbf{y}}), \\
\underline{\alpha}_{\mathrm{mm}}^{\mathrm{eff}} &= \alpha_{\mathrm{mm}}^{\mathrm{eff}} (\hat{\mathbf{x}}\hat{\mathbf{x}} + \hat{\mathbf{y}}\hat{\mathbf{y}}),
\end{aligned} \tag{5.15}$$

where $\alpha_{\mathrm{ee}}^{\mathrm{eff}} = \alpha_{\mathrm{ee}}/(1 - \alpha_{\mathrm{ee}}\check{G}_{\mathrm{ee},xx})$ and $\alpha_{\mathrm{mm}}^{\mathrm{eff}} = \alpha_{\mathrm{mm}}/(1 - \alpha_{\mathrm{mm}}\check{G}_{\mathrm{mm},xx})$. Note that due to the symmetry of the structure and to normally incident excitation, the in-plane effective polarizabilities of the square array of Si spheres are isotropic. Since here we deal only with normal incidence we then consider the two polarizabilities as scalars. Because of what demonstrated in 5.7 and referring to condition 5.9 as the effective Kerker condition for an array of NAs we now investigate if this condition is satisfied for an array of Si nanospheres. We first check the occurrence of the effective Kerker condition by checking the vanishing of reflectivity when the array is illuminated by a plane wave with linear polarization and normal incidence. Once this is established, we will observe how the effective Kerker condition for the array illuminated by circular polarization will lead to almost optimal helicity density.

The power reflectivity r and transmittivity t coefficients of the array of NAs with radius a

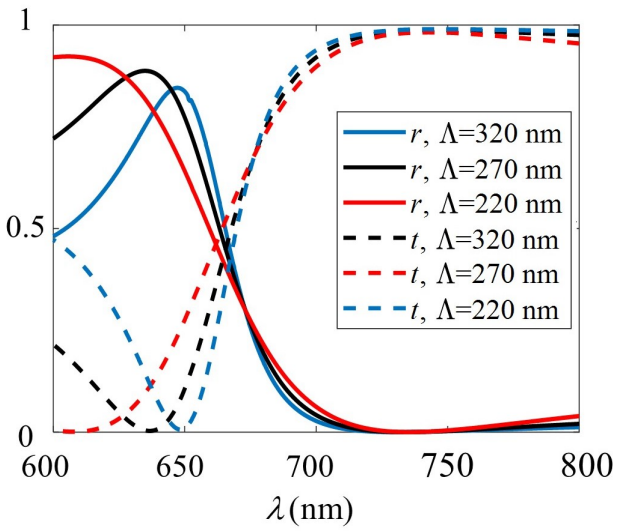

Figure 5.7

= 85 nm when the array is irradiated by a plane wave with linear polarization propagating along the negative z direction, calculated by using full-wave simulations, for three distinct periodicity parameters Λ is depicted in Figure5.7. This figure shows that the array has almost total transmittivity at the wavelength where the effective Kerker condition is satisfied [6]. This does not occur at the wavelength at which the scattering cross section σ_s of a single NA takes its maximum (see Figure 5.1), though it is not far from that.

As it is clear from this figure, the null in the reflectivity r does not dramatically change with period length Λ and it approximately (note a small shift in the wavelength of the null) occurs around a wavelength λ=730 nm, where the Kerker condition [6] is satisfied for an individual NA with radius a=85 nm. Indeed, our calculations show that effective polarizabilities of Si NA with radius a=85 nm arranged in an array are slightly perturbed with respect to those of individual Si NA shown in Figure 5.2 and therefore changing periodicity slightly affects the wavelength at which the null in reflectivity occurs. Moreover, a zero transmission occurs at wavelengths in the range 600nm $< \lambda <$ 650nm for the cases considered which shows that the second Kerker condition is almost satisfied.

5.2.1 Helicity Density of an Array of NAs Illuminated by a Plane Wave with Circular Polarization

As an illustrative example, the effective electric and magnetic polarizabilities of spherical Si NAs in an array with periodicity $\Lambda = 220$nm are depicted in Figure 5.8(a). This figure shows the effective polarizabilities of Si NA deviates from the optimal chirality relation $\alpha_{\text{ee}}^{\text{eff}}/\epsilon_0 = \alpha_{\text{mm}}^{\text{eff}}$ since the phase difference $\Delta\varphi$ between effective polarizabilities does not vanish completely at the wavelength of 752 nm where the magnitudes of effective polarizabilities satisfy $\left|\alpha_{\text{ee}}^{\text{eff}}/\epsilon_0\right| = \left|\alpha_{\text{mm}}^{\text{eff}}\right|$.

To investigate the closeness to the optimal chirality condition in nearfield of this array, we illuminate the array with a left-handed circular polarized plane wave, and we plot in Figure 5.8 (b) the quantity $\omega h/u$ at the surface $z = 0$, at three different wavelengths: (i) at $\lambda = 704$nm where $\Delta\varphi$ goes to zero; (ii) at $\lambda = 735$nm, where the minimum reflection from the array with periodicity $\Lambda = 220$nm occurs as shown in Figure 5.7; and (iii) at $\lambda = 752$nm where relation $\left|\alpha_{\text{ee}}^{\text{eff}}/\epsilon_0\right| = \left|\alpha_{\text{mm}}^{\text{eff}}\right|$ is satisfied.

Among the three cases the relation $\omega\left|h\right|/u = 1$ is most nearly satisfied at $\lambda = 735$nm. Therefore this figure shows that the nearfield of the array is closest to satisfying optimally chiral condition where the minimum reflection occurs, which is between the two wavelengths where the magnitudes and phase difference of the effective polarizabilities satisfy the Kerker condition 5.9. Note that lattice resonances, i.e., modes of the array, occur when the denominator of the effective polarizabilities vanishes. This condition will be analyzed in a future investigation; however, we expect strong field and helicity enhancement close to these lattice resonances.

Next, we further analyze helicity density of the field in between the arrayed NAs at the specific wavelength corresponding to almost full transmission. As discussed earlier, when the Kerker condition (for a single NA) is satisfied, the reflectivity r and transmittivity t of

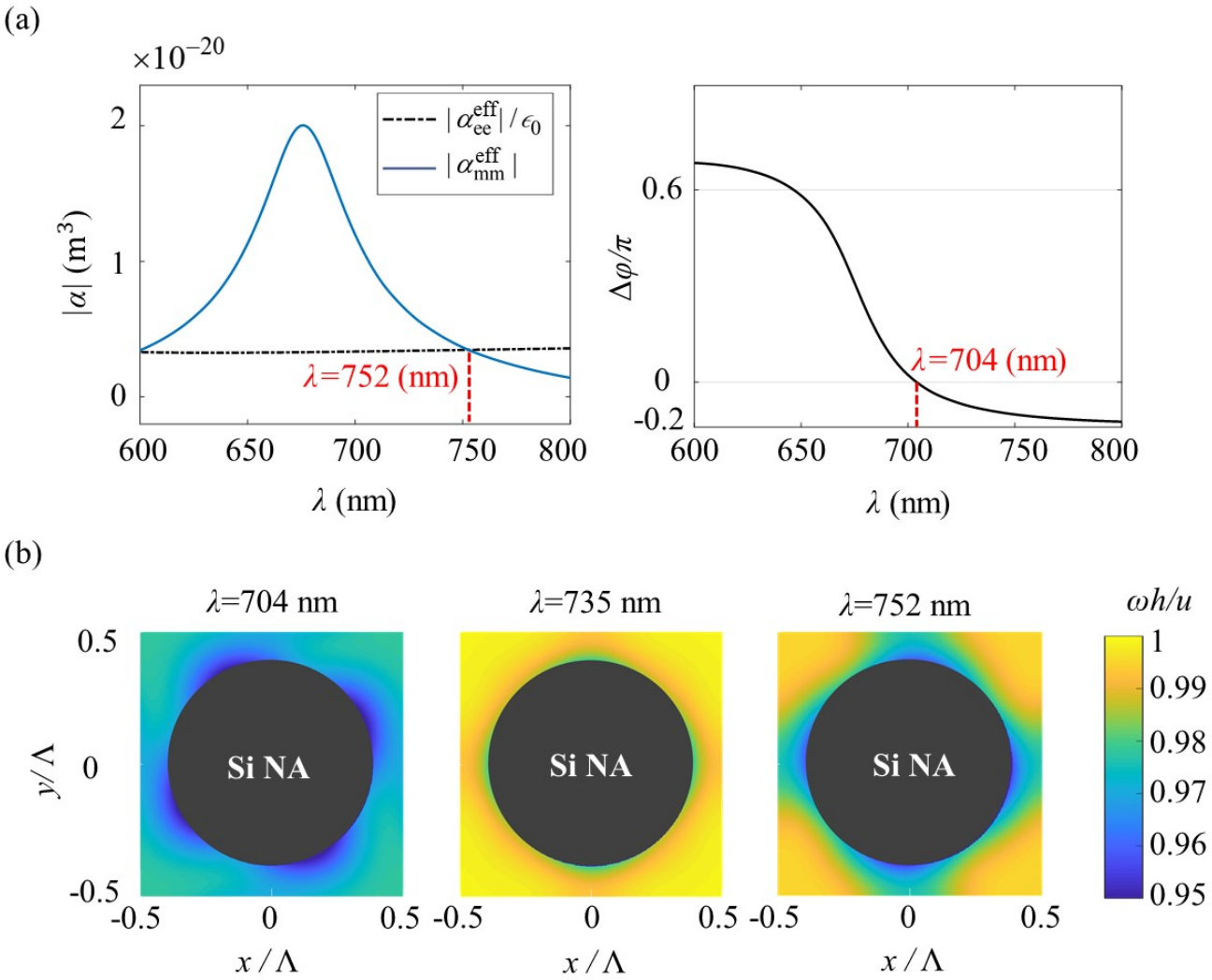

Figure 5.8: (a) Effective polarizabilities of an array of spherical Si NAs with radius 85 nm and periodicity $\Lambda = 220$ nm deviate form optimally chiral condition $\alpha_{ee}^{eff}/\epsilon_0 = \alpha_{mm}^{eff}$. (b) The quantity $h\backslash omega/u$ in nearfield of the array illuminated by a left-handed circularly polarized plane wave at three different wavelengths: (i) at $\lambda = 704$ nm where $\Delta\varphi$ goes to zero; (ii), and at $\lambda = 735$ nm, where the minimum reflection from the array with periodicity $\Lambda = 220$ nm occurs; (iii) at $\lambda = 752$ nm where the relation $|\alpha_{ee}^{eff}|/\epsilon_0 = |\alpha_{mm}^{eff}|$ is satisfied. The relation $|h|\omega/u = 1$ is most nearly satisfied at $\lambda = 735$ nm.

the array are chiefly affected by the radius of the NAs, whereas the periodicity parameter Λ does not significantly shift the maximum transmittivity's wavelength. However, when the periodicity parameter Λ is reduced, the distance between NAs decreases. Therefore, energy density is localized in hot spots formed in spaces between NAs and the upper bound of helicity density which is linearly linked to energy density also increases.

In Figure 5.9, we show the total helicity density at the surface $z = 0$, normalized to that of the incident circularly polarized field, for two distinct array periods of $\Lambda = 220$nm and $\Lambda = 190$nm. This figure shows that the array with smaller periodicity parameter Λ offers higher helicity enhancement in the hot spots formed between NAs. In particular, one can observe that for arrays with periodicity $\Lambda = 220$nm and $\Lambda = 190$nm such enhancement drops, respectively, to 80 and 90 percent of their values on the surface of the NA at a distance approximately equal to 0.015λ away from the surface of the NA. Note that helicity enhancement around a single NA that was depicted in Figure 5.4 drops approximately to 75 and 50 percent of its value on the surface of the NA, respectively, at a distance equal to 0.015λ and 0.03λ away from the surface of the NA.

To further clarify this point, in Figure 5.10, helicity enhancement is plotted varying position along the x axis and along the diagonal line of a unit cell, for the array with periodicity $\Lambda = 190$nm. This shows that an array of Si NA provides a helicity enhancement almost similar to that around a single NA, but with better uniform distribution. Indeed, the array arrangement of NAs spatially extends the enhanced helicity density over a large surface which is advantageous in some applications. Note that the helicity densities illustrated in Figure 5.9 possess the same sign over the whole $z = 0$ surface and also off the $z = 0$ surface. Moreover, it is particularly important to have fields close to satisfying the optimally chiral condition $\omega |h| / u = 1$ which maximizes helicity density at a given energy density. As discussed earlier, the field around a single NA with radius a=85 nm at wavelength $\lambda = 730$nm, are very close to be optimally chiral when helicity and energy densities satisfy $h = \pm u/\omega$.

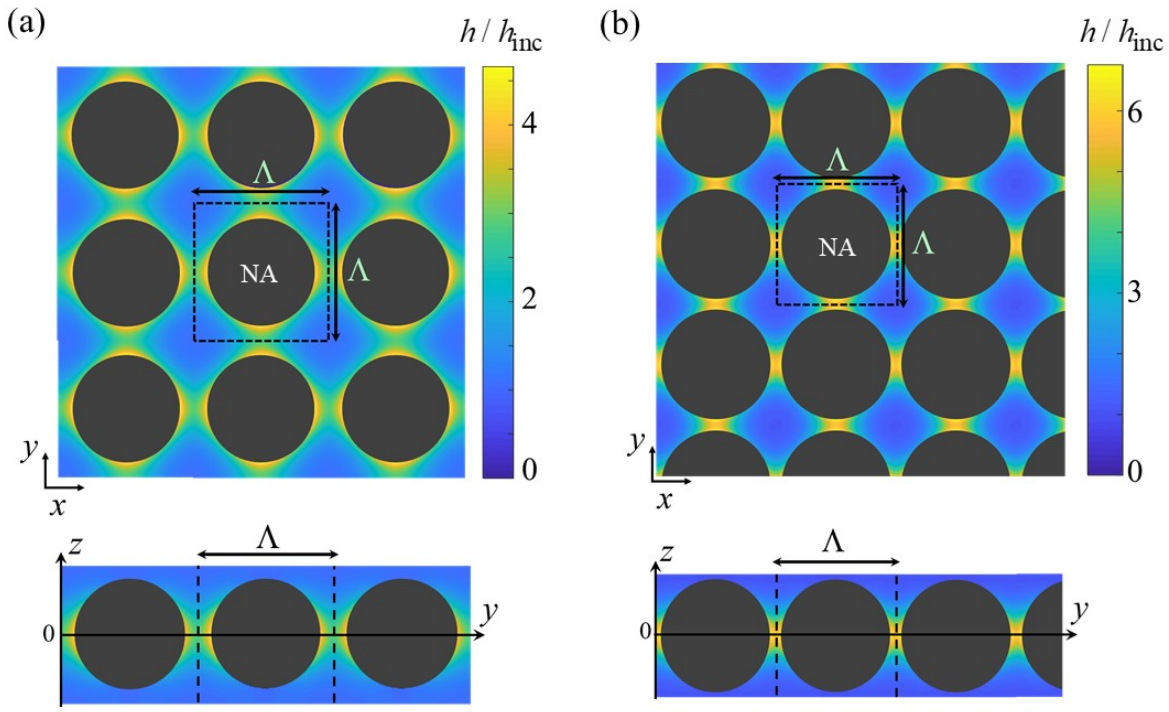

Figure 5.9: Helicity enhancement, i.e., helicity density of an array of high-density NAs, with radius $a = 85$nm made of Si, normalized to that of the incident left-handed circularly polarized field at wavelength $\lambda = 735$ nm., evaluated at $z = 0$, and on the $y - z$ plane, respectively. Two arrays are considered with period of (a) $\Lambda = 220$nm, and (b) $\Lambda = 190$nm. Note the different scale, and the higher helicity for the case with period $\Lambda = 190$nm.

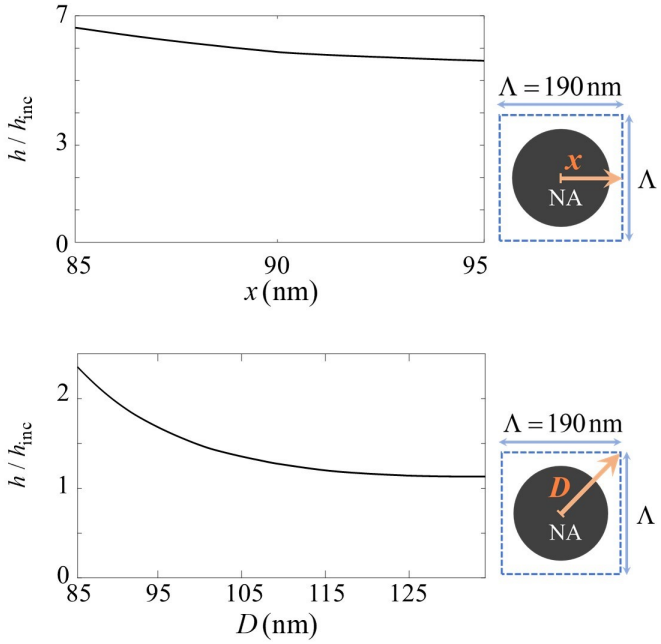

Figure 5.10: Helicity enhancement along the x axis and the diagonal line in a unit cell of an array of Si spheres with radius 85 nm and periodicity parameter $\Lambda = 190$nm, at the array plane $z = 0$.

In Figure 5.11 we show the product of helicity density and angular frequency normalized to energy density, i.e., we show $\omega h/u$ (which equals unity for optimally chiral fields) at the surface z=0 of a unit cell of the array, in the $x-y$ plane. Figure 5.11 shows that field over the surface of the array is very close to be optimally chiral, however, when the periodicity of the array decreases, the field deviates from the required condition $\mathbf{E} = \pm i\eta_0\mathbf{H}$ by approximately 5 per cent, so it is less optimally chiral.

5.2.2 Effect of a Substrate on Helicity Density Generated by an Array of Si NA

We examine here the impact of adding a glass substrate on the functionality of an array of high-density NAs. As an example, we consider an array of Si NAs with radius $a = 85$ nm and periodicity $\Lambda = 270$nm located on top of a glass substrate with refractive index $n = 1.5$

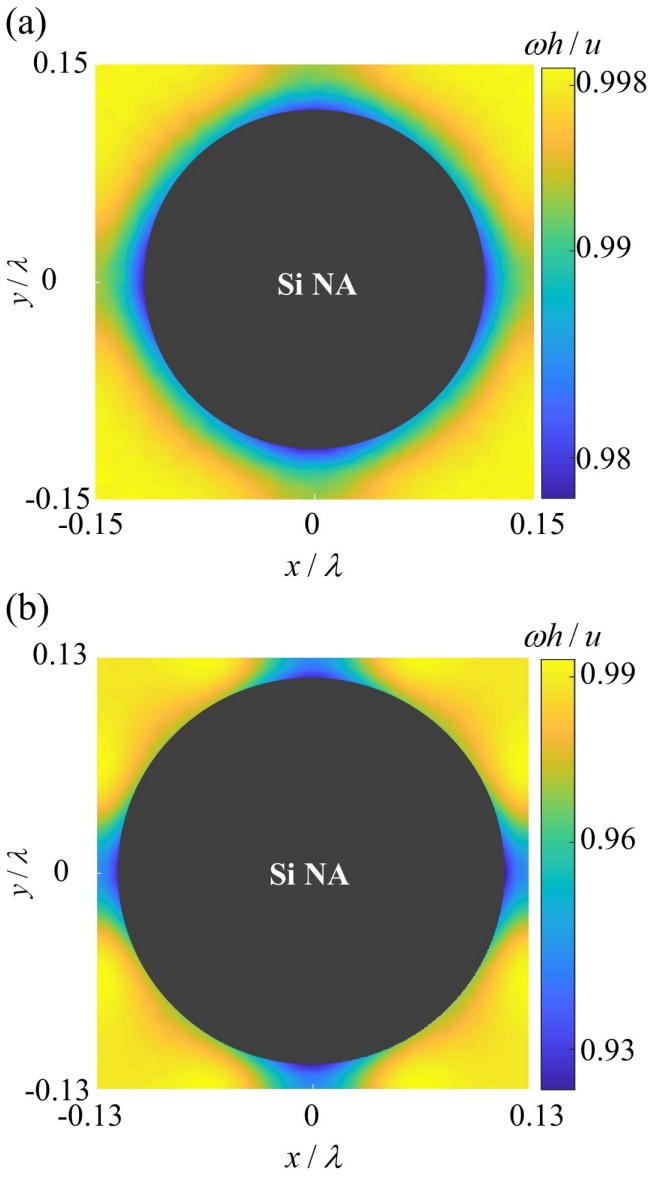

Figure 5.11: Plot of $\omega h/u$, i.e., the product of helicity density and angular frequency normalized to the energy density, generated by an array of high-density NAs with radius a=85 nm illuminated by a left-handed circularly polarized plane wave. We show such quantity in the $x-y$ plane (at $z=0$) over a unit cell of the array with period (a) $\Lambda = 220$ nm, and (b)$\Lambda = 190$ nm. Note that $\omega\left|h\right|/u = 1$ for optimally chiral fields, and this plot shows that the field in the NA array is close to that limit.

and thickness d depicted in Figure 5.12 (a). The substrate interface is at $z = a$. We calculate the power reflectivity and transmittivity of this array for two cases: (a) when the substrate has an infinite thickness d (it occupies the region $z < a$) and (b) when the thickness is $d = 980$nm. Figure 5.12 (b) represents the reflectivity r and transmittivity t of the array illuminated by a plane wave with circular polarization propagating along the negative z direction. Note that the substrate with thickness $d = 980$nm fully transmits a normally incident plane wave at $\lambda = 735$nm where the exact null of reflectivity r of such an array of Si NAs occurs. This figure shows that when the substrate has a thickness $d = 980$nm, the wavelength at which the null of reflectivity r occurs has changed very slightly (about 1 nm) with respect to the case when the substrate is not present at all (compare with Figure 5.7). However, for a substrate with an infinite thickness the reflectivity r never approaches zero and takes a value approximately equal to 0.04 at $\lambda = 735$nm.

Moreover, to investigate how the optimal chirality of the nearfield of the array is affected by the presence of the substrate, in Figure 5.13 we plot $\omega h/u$ over the $x - y$ plane (at $z = 0$) in a unit cell of the array at wavelength $\lambda = 735$nm. This figure illustrates that the nearfield over the surface of the array is very close to satisfying optimal chirality condition $\omega |h| / u = 1$ in the presence of the substrate with thickness $d = 980$nm. However, for a substrate with an infinite thickness this quantity decreases by 10 percent at wavelength $\lambda = 735$nm which emphasizes the importance of optimizing the thickness of the substrate. Therefore, the chiral operation of the array is weakly affected by the presence of the glass substrate when its thickness is optimized to transmit the total incident power. The small effect of the substrate for the optimized substrate thickness is because the NAs are mainly in air (above the substrate) and the contrast between the glass substrate and the air is not very high and hence the scattered nearfield by the NAs remains quite similar to the case without substrate.

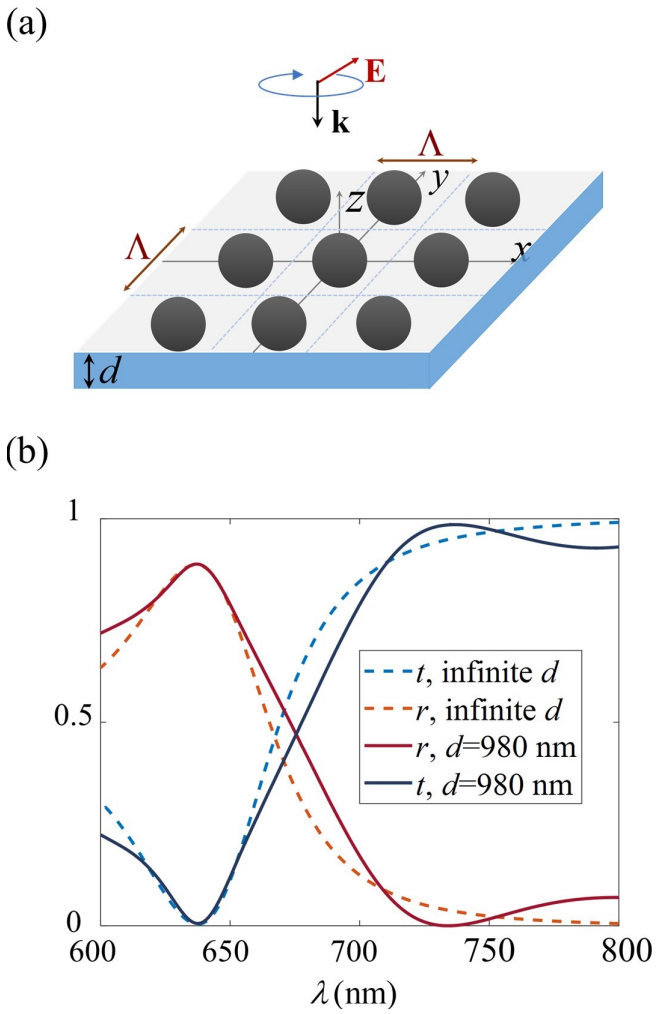

Figure 5.12: (a) An array of high-density NAs with radius a =85 nm with periodicity Λ=270 nm located on a glass substrate with refractive index n =1.5 illuminated by left-handed circularly polarized plane wave propagating along the negative z direction, and (b) reflectivity r and transmittivity t of this array when the substrate has a finite thickness d=980 nm and also for the semi-infinite case when it occupies the region $z < a$.

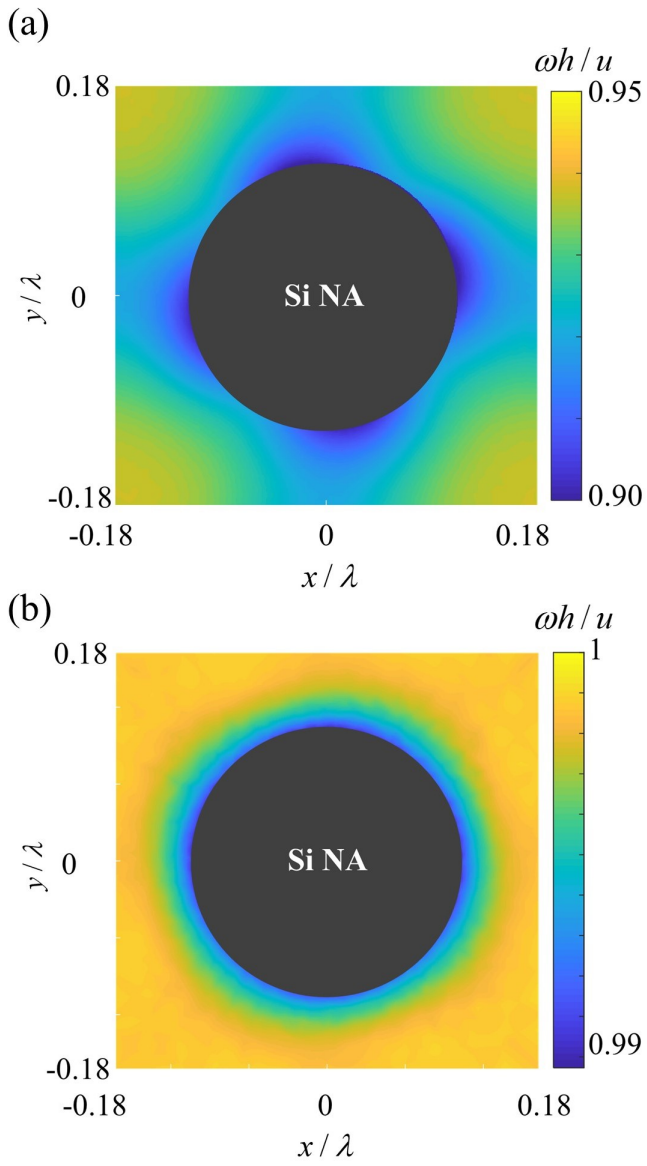

Figure 5.13: Plot of $\omega h/u$, i.e., the product of helicity density and angular frequency normalized to the energy density, generated by an array of high-density NAs with radius a=85 nm and periodicity Λ=270 nm located on a glass substrate with refractive index n =1.5 illuminated by a left-handed circularly wave at wavelength λ = 735nm when (a) the substrate has an infinite thickness and it occupies the region z < a and (b) when it has a thickness d=980 nm.

5.3 conclusion

We have shown that an array composed of spherical high-density dielectric nanoantennas illuminated by a plane wave with circular polarization generates near-field very close to satisfying optimal chirality condition with enhanced helicity density. First, we have investigated helicity density in the nearfield of a single NA with balanced electric and magnetic polarizabilities, irradiated by a plane wave with circular polarization and discussed how the NA's scattered field is optimally chiral. Helicity density is enhanced with a factor of 6.3 in vicinity of a single NA, symmetrically in the plane transverse to the propagation direction of the incident field. However, helicity density of the scattered fields drops quickly moving away from the surface of a single NA. Therefore, in the second part of the paper we have shown how helicity is enhanced over a surface of an array of NAs. We also show how the optimal chiral condition is related to the effective Kerker condition of the effective polarizabilities of the array particles and this is affected by the array period. Moreover, we investigated how the chiral operation of the array is affected in the presence of a glass substrate. The array nearfield slightly deviates from the optimal chiral condition when the inter-particle distances decreases but it generates a helicity enhancement over the whole array surface. This may present significant advantages in the detection of chirality of substances at surface level instead of in the bulk.

Bibliography

[1] C. F. Bohren and D. R. Huffman, *Absorption and Scattering of Light by Small Particles*. 1998.

[2] "CST studio suite, 2019." `https://caelynx.com/product/cst-studio-suite/`.

[3] D. E. Aspnes and A. A. Studna, "Dielectric functions and optical parameters of si, ge, gap, gaas, gasb, inp, inas, and insb from 1.5 to 6.0 ev," *Phys. Rev. B*, vol. 27, pp. 985–1009, Jan 1983.

[4] T. Niemi, A. O. Karilainen, and S. A. Tretyakov, "Synthesis of polarization transformers," *IEEE Transactions on Antennas and Propagation*, vol. 61, pp. 3102–3111, June 2013.

[5] M. Albooyeh, S. Tretyakov, and C. Simovski, "Electromagnetic characterization of bianisotropic metasurfaces on refractive substrates: General theoretical framework," *Annalen der Physik*, vol. 528, no. 9-10, pp. 721–737, 2016.

[6] M. Kerker, D.-S. Wang, and C. L. Giles, "Electromagnetic scattering by magnetic spheres," *J. Opt. Soc. Am.*, vol. 73, pp. 765–767, Jun 1983.

[7] S. Campione, F. Capolino, and F. Mesa, "Magnetoinductive waves in 2d periodic arrays of split ring resonators," in *Proceedings of the 2012 IEEE International Symposium on Antennas and Propagation*, pp. 1–2, July 2012.

[8] A. L. Fructos, S. Campione, F. Capolino, and F. Mesa, "Characterization of complex

plasmonic modes in two-dimensional periodic arrays of metal nanospheres," *J. Opt. Soc. Am. B*, vol. 28, pp. 1446–1458, Jun 2011.

Chapter 6

Rayleigh Anomaly in Surface Enhanced Raman Spectroscopy

Surface enhanced Raman spectroscopy (SERS)[1, 2, 3] unites plasmonic and nearfield optics[4] and Raman spectroscopy to offer high sensitivity in detection of molecules and bio-molecules. Surface Enhanced Raman Spectroscopy has a broad range of applications in biotechnology and biology[5, 6], analytical chemistry[7, 8], pharmaceutical field [9, 10], and forensic sciences [11]. A higher enhancement in electric field in an assembly of plasmonic nanoparticles (NP) [12, 13, 14] boosts the sensitivity of SERS in detection of chemical compounds and this has resulted in the rich literature on this topic[15, 16, 17, 18, 19]. It has been shown that a combination of Rayleigh anomaly [20, 21, 22] and colloidal Plasmonic resonances boosts the field enhancement in SERS spectroscopy [23]. In this chapter, we investigate how a combination of Rayleigh anomaly and resonance modes in a pearl chain of gold spherical NPs aligned perpendicular to the array of plasmonic rods, as illustrated in Figure 6.1, leads to enhancement in electric field in the hot spots between the NPs. This structure is faricated by using nanorods as electrodes to apply an electric field polarized in the direction perpendicular to the rods which exerts force on NPs in a suspensionpolar and

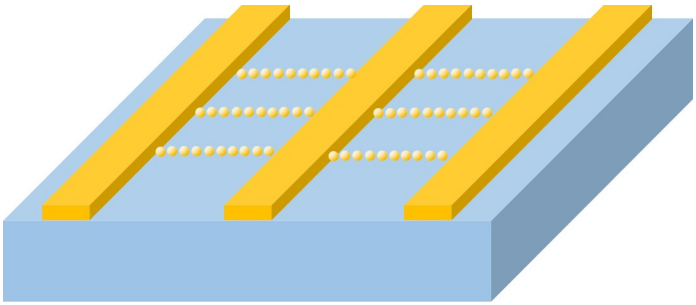

Figure 6.1: An array of infinite plasmonic rods and chains of gold NPs aligned perpendicular to the orientation of the rods located on a glass substrate may be fabricated by using dielectrophoresis.

guides their electrokinetic motion, referred to as dielectrophoresis, inorder to assemble them in a chain[24, 25, 26].

6.1 Rayleigh Anomaly in an Array of Plasmonic Rods

Rayleigh anomaly refers to the change in the transmission spectrum of a periodic structure due to the existence of grazing diffraction orders and excitation of surface waves [20, 21, 22]. Here, we consider an array of infinite rectangular rods with height H, width W, and periodicity parameter L_y in y direction, lying parallel to the x axis as it is illustrated in Figure 6.2(a). The array is placed on an isotropic homogeneous semi-infinite substrate with refractive index n_s and is covered by a semi-infinite superstrate with refractive index n. First, we consider the case where the substrate is absent and the array is immersed in a homogeneous medium with refractive index index n and wave number $k_h = k_0 n$. According to the Floquet theorem [27], when the array is illuminated by a plane wave with wave vector $\mathrm{k}^{\mathrm{inc}} = k_{x0}\hat{\boldsymbol{x}} + k_{y0}\hat{\boldsymbol{y}} + k_{z0}\hat{\boldsymbol{z}}$, electromagnetic field in the space below and above the array may

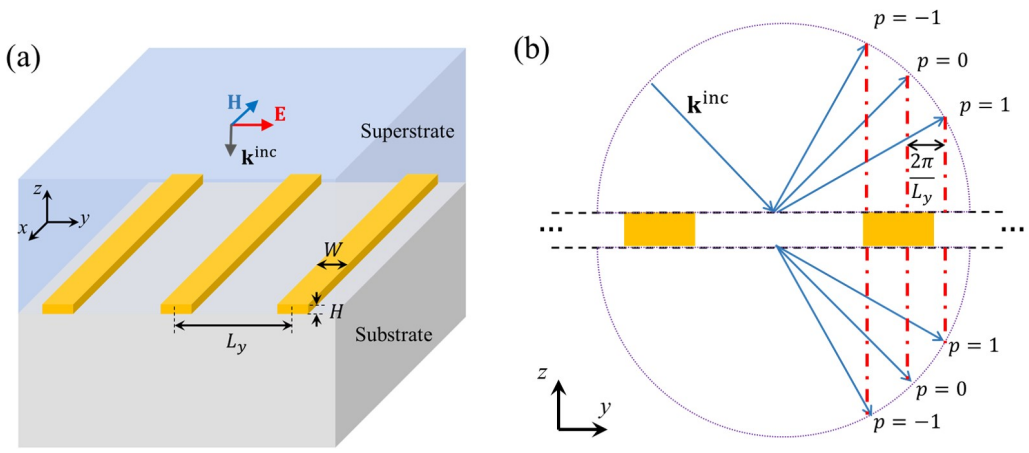

Figure 6.2: (a) An array of rectangular plasmonic rods oriented parallel to the x axis, placed on top of a substrate and covered by a superstrate, is illuminated by a plane wane propagating anolg the $-z$ direction and polarized along the y axis. (b) Electromagnetic fields in the space below and above the array may be expanded into Floquet harmonics propagating along a discret set of directions.

be expanded into a discrete set of plane waves with wave vector

$$\mathrm{k}_p = k_x\hat{\boldsymbol{x}} + k_y\hat{\boldsymbol{y}} + k_z\hat{\boldsymbol{z}} = k_{x0}\hat{\boldsymbol{x}} + \left(k_{y0} + \frac{2\pi}{L_y}p\right)\hat{\boldsymbol{y}} + k_{z,p}\hat{\boldsymbol{z}}, \tag{6.1}$$

where $p = 0, \pm1, \pm2, \ldots$ denotes the p^{th} diffraction order with $k_{z,p} = \pm\sqrt{k_h^2 - k_x^2 - k_y^2} = \pm\sqrt{k_h^2 - \left(k_{y0} + \frac{2\pi}{L_y}p\right)^2 - k_{x0}^2}$. Diffraction of electromagnetic filed when $k_{x0} = 0$ is qualitatively illustrated in Figure 6.2(b).

Rayleigh anomaly occurs when the normal component of the wave vector of a diffraction order, i.e., $k_{z,p}$ vanishes. In this chapter, we assume that the incident plane wave is propagating along the $-z$ direction and $k_{x0} = k_{y0} = 0$ which simplifies $k_{z,p}$ to

$$k_{z,p} = \pm\sqrt{k_h^2 - \left(\frac{2\pi}{L_y}p\right)^2} \tag{6.2}$$

and Rayleigh anomaly related to the diffraction order p occurs at the wavelength λ_p when $k_{z,p} = 0$ i.e.,

$$\lambda_p = \frac{L_y n}{|p|}\, p \neq 0, \tag{6.3}$$

where coherent interaction between multiple diffraction orders generates an enhancement in the magnitude of the electric field [23]. Here, we aim at employing the first Rayleigh anomaly i.e., $p = \pm 1$ to boost the electric field at wavelengths ranging from 780 to 850 nm and the rods are immersed in water with refractive index $n = 1.33$ [28]. Moreover, the incident electric field is assumed to be polarized along the y axis and the refractive index of gold is taken from Ref. [29]. Furthermore, we define two field enhancement factors: one, denoted by FE_y, is defined as the magnitude of the y component of the electric field normalized to that of field in the absence of plasmonic rods and NPs, and one, denoted by FE, is defined as the magnitude of the total field normalized to that of the electric field in the absence of plasmonic rods and NPs. To obtain the maximum field enhancement, we calculated the mean value of field enhancement in the wavelength range from 780 to 850 nm at locations of the probes P_1 to P_9, shown in Figure 6.3(a), for various design parameters height H, width W, and periodicity L_y. The structure with periodicity $L_y = 500$nm, $H = W = 100$nm offers the maximum mean value of field enhancement in the desired wavelength range (see Appendix B for more detail) and is referred to as the optimized array in the rest of this chapter. In what follows we focus on the field enhancement in the optimized array.

The enhancement of the magnitude and of the y component of the electric field versus wavelength calculated at locations of the probes P_1 to P_9 in the optimized array are depicted in Figure 6.4. The first Rayleigh anomaly occurs at $\lambda_{\pm 1} = 1.33 \times L_y = 665$nm where a change in the magnitude and y component of the electric field shown, respectively, in Figure 6.4

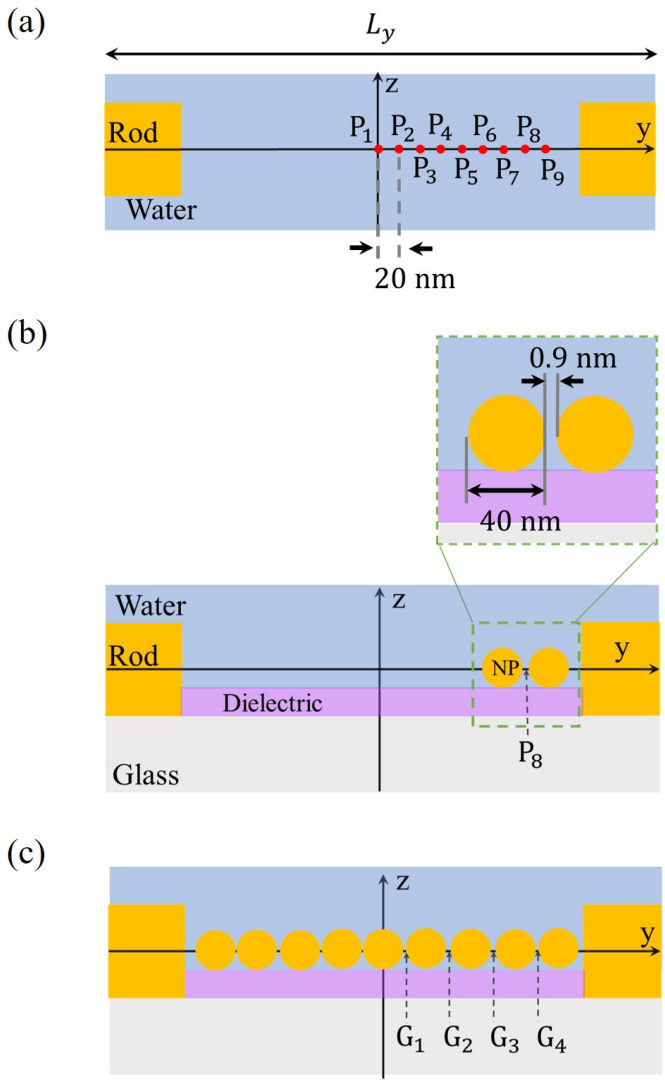

Figure 6.3: (a) Nine probes $P_1, ..., P_9$ are located along the y axis in the $x-z$ plane of the optimized array to monitor the field enhancement. (b) A dimer is located in proximity of the plasmonic rod such that the middle of its gap is placed at the probe P_8.(c) A chain of nine NPs are arranged along the y axis and four probes $G_1, .., G_4$ are used to monitor the field enhancement in the Chain's hot spots.

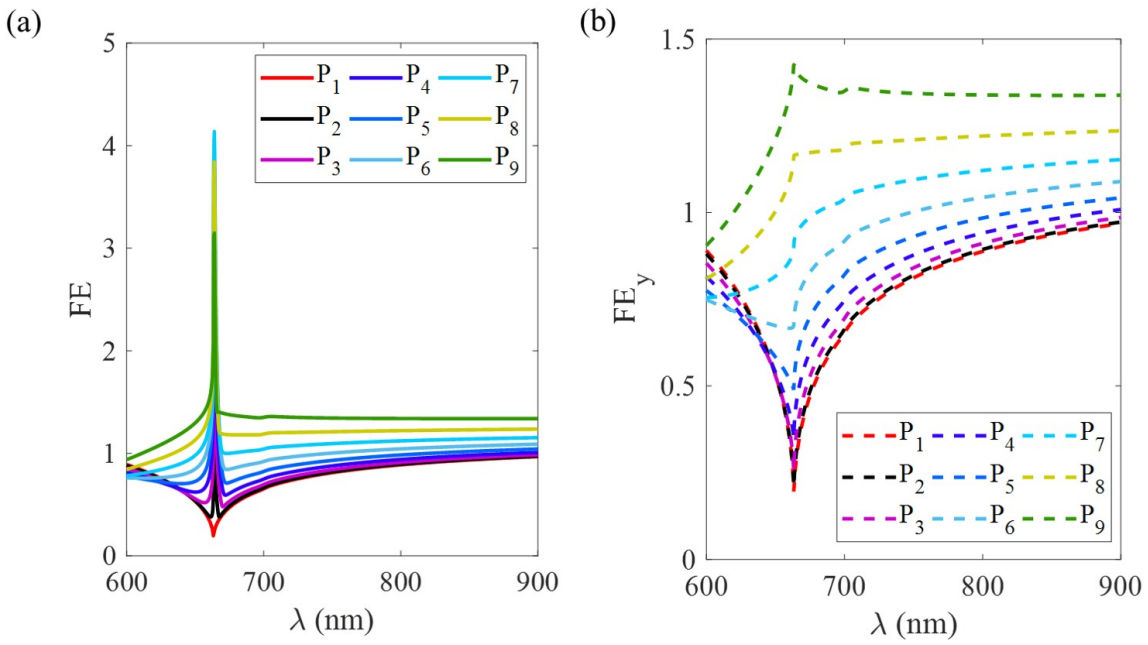

Figure 6.4: The enhancement (a) in the magnitude FE and (b) in the y component FE_y of the electric field at probes $\mathrm{P}_1, ..., \mathrm{P}_9$ in the optimized array with periodicity $L_y = 500$nm, $H = W = 100$nm.

(a) and (b), is observed. In the middle of the space between the rods, i.e., at probe P_1, the electric field is attenuated with respect to the incident electric field, however, an enhancement is observed for probes closer to the plasmonic rods. This is in contrast with field enhancement in the same array when the incident electric field is polarized along the x axis and parallel to the rods where the field magnitude takes its maximum value at P_1, and vanishes at the probes close to the rods. The field enhancement in an array of plasmonic rods illuminated by a x-polarized electric field is discussed in detail in Ref. [23] and is beyond the scope of this work.

In real world applications, the array is placed on a substrate. Here, we consider a semi-infinite substrate extending from the bottom of the rods to infinity in $-z$ direction and made of glass with a refractive index $n_s = 1.5$. The glass substrate is convenient since the small difference between the refractive indices of the substrate and the superstarte prevents a high reflection of the incident field at their interface which ruins the field enhancement. In the presence

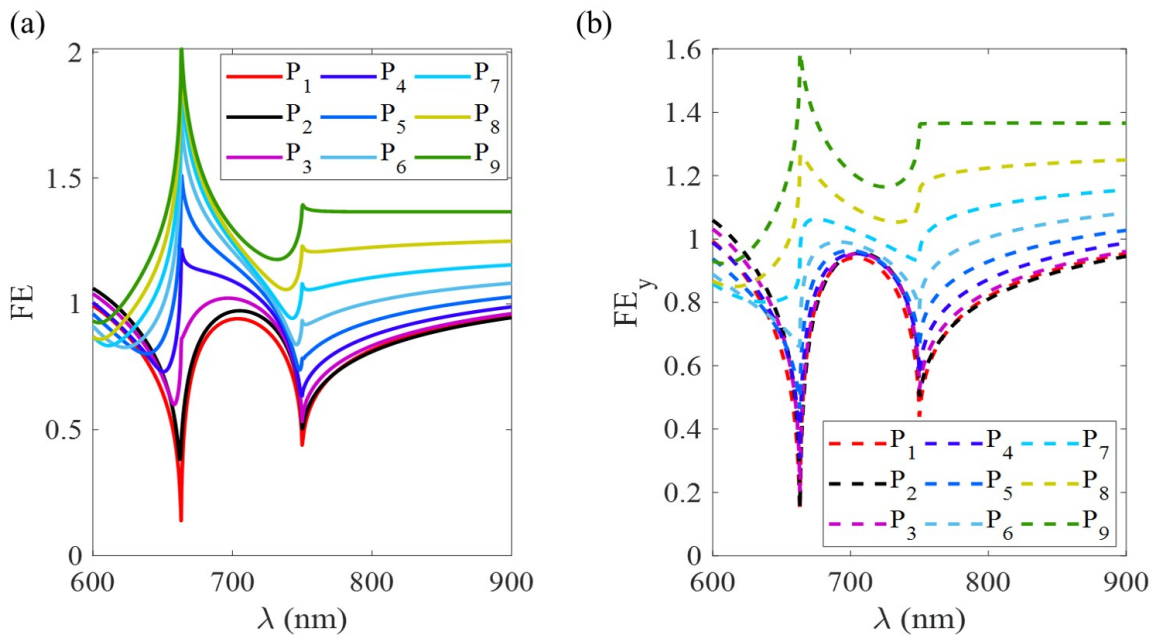

Figure 6.5: The enhancement (a) in the magnitude FE and (b) in the y componnet $FE_y$of the electric field at probes in the optimized array with parameters $L_y = 500$nm, $H = W = 100$nm and a semi-infinite glass substrate.

of the substrate, we define the field enhancements as the magnitude of the y component or the total field, normalized to the magnitude of the incident field when the rods are absent denoted, respectively, by FE_y and FE. In Figure 6.5, FE_y and FE of the optimized structure with a glass substrate is illustrated. This figure shows that when the substrate is introduced, we observe two anomalies: one at the wavelength $\lambda_{\pm 1,water} = 1.33L_y = 665$nm and one at $\lambda_{\pm 1,glass} = 1.5L_y = 750$ nm, and the interference between these two determines the overall field enhancement. Moreover, the optimized structure offers a uniform field enhancement with a maximum value of 1.4 at the probe P_9 in the desired wavelength range $780 - 850$nm. Note that a SERS signal is proportional to the fourth power of the magnitude of the electric field [30] and a field enhancement equal to 1.4 approximately results in a 4-fold enhancement in the SERS signal. Next, we place a chain of gold NPs to examine the field enhancement in its hot spots.

6.2 Field Enhancement in an Assembly of gold NPs and Plamnonic Array of Rods

So far we have discussed how the interference between the diffraction orders in a periodic array of plasmonic rods enhances the electric field in its vicinity. In this section, we investigate the field enhancement in the hot spots of closely spaced NPs placed in vicinity of the optimized structure with periodicity $L_y = 500$nm and $H = W = 100$nm. Moreover, a layer of dielectric material with a refractive index n_d and a thickness equal to 30 nm is placed on top of the substrate[13]. First, we investigate the field enhancement by a dimer of spherical gold NPs with radii equal to $a = 20$nm and their centers located at $y = 140\text{nm} \pm (a + g/2)$, illustrated in Figure 6.3(b), where $g = 0.9$ nm is the gap between their surfaces along the y axis[23, 18, 15]. Indeed, the center of the gap between the NPs coincides with the location of the probe P_8 where the field enhancement is calculated. Figure 6.6 depicts the field enhancement at the probe P_8 in the gap of the dimer in the absence and presence of the array of rods. This figure shows that the magnitude of the electric field is boosted with respect to that in the strcuture without the array, in the wavelengths range from 780 to 850 nm starting from 1.6 at 780 nm and decreasing uniformly to 1.35 at 850 nm. Note that due to the Rayleigh anomaly in the substrate, we observe a deep valley in the field enhancement around the wavelength 750 nm and this shows the importance of the proper choice of the periodicity parameter L_y which prevents the valley to occur in the desired wavelength range.

Now, let us consider a chain of nine gold NPs with same radii arranged along the y axis Figure 6.3(c). The chain is symmetric with respect to $x - z$ and $y - z$ planes and the center of the middle NP is placed at $y = 0$. Field enhancement is calculated at the center of the gaps, marked as $G_1, ..., G_4$ shown in Figure 6.3(c), in the absence and presence of the rods and the results are depicted in Figure 6.7. This figure shows that in the absence of the array of rods, the maximum field enhancement in the chain occurs at G_1 and decreases

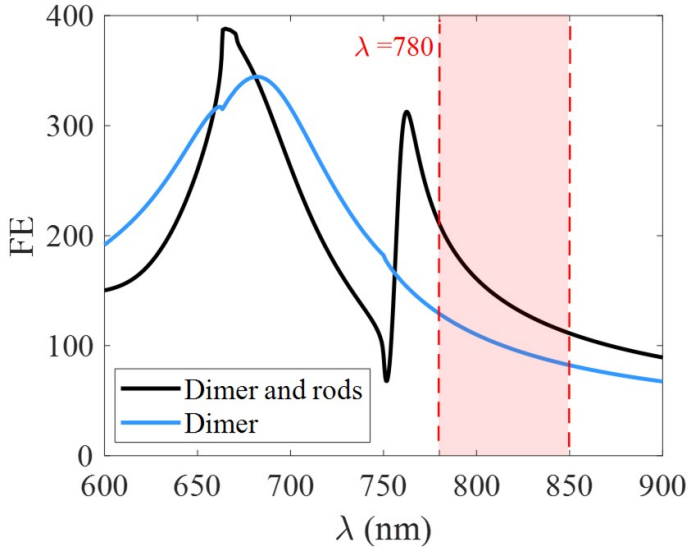

Figure 6.6: The field enhancement FE at probe P_1 in the middle of the gap of a dimer depicted in Figure 6.3(b) in the absence, marked as "Dimer", and presence, marked as "Dimer and rods", of the array of rods. Rods further enhance the electric field in the wavelength range from 780 to 850 nm marked by a red box.

uniformly in the gaps further from the center. This is in contrast to the spatial distribution of the field enhancement in the array of rods where we observe the maximum enhancement at locations closer to the rods. Moreover, the peak of the field enhancement has shifted to longer wavelength with respect to that of a dimer. This shows that the chain provides a considerably higher enhancement at the desired wavelength range from 780 to 850 nm with respect to the dimer. By adding thearray of rods, the field enhancements at probes G_1 and G_2 slightly decrease, however, an increase in the enhancement is observed at probes probes G_3 and G_4.

6.3 Conclusion

In this chapter, field enhancement in a substrate for SERS fabricated by dielectrophoresis[24, 25, 26] has been investigated. The designed SERS substrate consists of a chain of gold NPs perpendicularly placed in the space between an array of plasmonic rods on a glass slab.

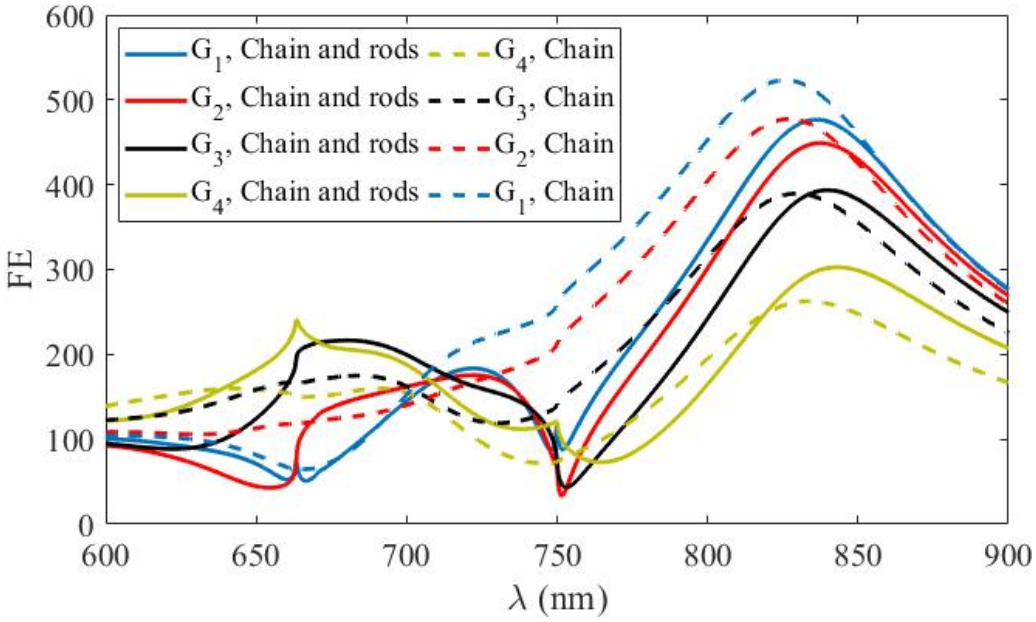

Figure 6.7: The field enhancement FE at probes $G_1, ..., G_4$ in the hot spots of a chain depicted in Figure 6.3(c) in the absence, marked as "Chain", and presence, marked as "Chain and rods", of the array of rods.

Our analysis shows that this structure offers 500-fold enhancement in the magnitude of the electric field at the hot spots formed in the gap between the NPs in the wavelength range from 780 to 850nm.

Bibliography

[1] J. A. Dieringer, A. D. McFarland, N. C. Shah, D. A. Stuart, A. V. Whitney, C. R. Yonzon, M. A. Young, X. Zhang, and R. P. Van Duyne, "Introductory lecture surface enhanced raman spectroscopy: new materials, concepts, characterization tools, and applications," *Faraday Discuss.*, vol. 132, pp. 9–26, 2006.

[2] E. Le Ru and P. Etchegoin, *Principles of Surface-Enhanced Raman Spectroscopy*. Elsevier Science, 2008.

[3] K. Kneipp, M. Moskovits, and H. Kneipp, *Surface-Enhanced Raman Scattering, Physics and Applications*. Springer-Verlag Berlin Heidelberg, 2006.

[4] B. E. A. Saleh and M. C. Teich, *Fundamentals of photonics*. Wiley, New York, NY, 1991.

[5] T. M. Cotton, J.-H. Kim, and G. D. Chumanov, "Application of surface-enhanced raman spectroscopy to biological systems," *Journal of Raman Spectroscopy*, vol. 22, no. 12, pp. 729–742, 1991.

[6] D. Cialla-May, X. S. Zheng, K. Weber, and J. Popp, "Recent progress in surface-enhanced raman spectroscopy for biological and biomedical applications: from cells to clinics," *The Royal Society of Chemistry*, vol. 46, pp. 3945–3961, 2017.

[7] G. McNay, D. Eustace, W. E. Smith, K. Faulds, and D. Graham, "Surface-enhanced

raman scattering (sers) and surface-enhanced resonance raman scattering (serrs): A review of applications," *Appl. Spectrosc.*, vol. 65, pp. 825–837, Aug 2011.

[8] S. Schlücker, "Surface-enhanced raman spectroscopy: Concepts and chemical applications," *Angewandte Chemie International Edition*, vol. 53, no. 19, pp. 4756–4795, 2014.

[9] J. Cailletaud, C. De Bleye, E. Dumont, P.-Y. Sacré, L. Netchacovitch, Y. Gut, M. Boiret, Y.-M. Ginot, P. Hubert, and E. Ziemons, "Critical review of surface-enhanced raman spectroscopy applications in the pharmaceutical field," *Journal of Pharmaceutical and Biomedical Analysis*, vol. 147, pp. 458–472, 2018. Review issue 2017.

[10] M. T. Alula, Z. T. Mengesha, and E. Mwenesongole, "Advances in surface-enhanced raman spectroscopy for analysis of pharmaceuticals: A review," *Vibrational Spectroscopy*, vol. 98, pp. 50–63, 2018.

[11] C. Muehlethaler, M. Leona, and J. R. Lombardi, "Review of surface enhanced raman scattering applications in forensic science," *Analytical Chemistry*, vol. 88, no. 1, pp. 152–169, 2016. PMID: 26638887.

[12] A. Vallecchi, S. Campione, and F. Capolino, "Symmetric and antisymmetric resonances in a pair of metal-dielectric nanoshells: tunability and closed-form formulas," *Journal of Nanophotonics*, vol. 4, no. 1, pp. 1 – 14, 2010.

[13] M. Darvishzadeh-Varcheie, C. Guclu, R. Ragan, O. Boyraz, and F. Capolino, "Electric field enhancement with plasmonic colloidal nanoantennas excited by a silicon nitride waveguide," *Opt. Express*, vol. 24, pp. 28337–28352, Dec 2016.

[14] J. Gargiulo, R. Berté, Y. Li, S. A. Maier, and E. Cortés, "From optical to chemical hot spots in plasmonics," *Accounts of Chemical Research*, vol. 52, no. 9, pp. 2525–2535, 2019. PMID: 31430119.

[15] C. Q. Nguyen, W. J. Thrift, A. Bhattacharjee, S. Ranjbar, T. Gallagher, M. Darvishzadeh-Varcheie, R. N. Sanderson, F. Capolino, K. Whiteson, P. Baldi, A. I. Hochbaum, and R. Ragan, "Longitudinal monitoring of biofilm formation via robust surface-enhanced raman scattering quantification of pseudomonas aeruginosa-produced metabolites," *ACS Applied Materials & Interfaces*, vol. 10, no. 15, pp. 12364–12373, 2018. PMID: 29589446.

[16] S. M. Adams, S. Campione, J. D. Caldwell, F. J. Bezares, J. C. Culbertson, F. Capolino, and R. Ragan, "Non-lithographic sers substrates: Tailoring surface chemistry for au nanoparticle cluster assembly," *Small*, vol. 8, no. 14, pp. 2239–2249, 2012.

[17] S. M. Adams, S. Campione, F. Capolino, and R. Ragan, "Directing cluster formation of au nanoparticles from colloidal solution," *Langmuir*, vol. 29, no. 13, pp. 4242–4251, 2013. PMID: 23472803.

[18] W. J. Thrift, C. Q. Nguyen, M. Darvishzadeh-Varcheie, S. Zare, N. Sharac, R. N. Sanderson, T. J. Dupper, A. I. Hochbaum, F. Capolino, M. J. Abdolhosseini Qomi, and R. Ragan, "Driving chemical reactions in plasmonic nanogaps with electrohydrodynamic flow," *ACS Nano*, vol. 11, no. 11, pp. 11317–11329, 2017. PMID: 29053246.

[19] D. Radziuk and H. Moehwald, "Prospects for plasmonic hot spots in single molecule sers towards the chemical imaging of live cells," *Phys. Chem. Chem. Phys.*, vol. 17, pp. 21072–21093, 2015.

[20] R. W. Wood, "On a remarkable case of uneven distribution of light in a diffraction grating spectrum," *Proceedings of the Physical Society of London*, vol. 18, pp. 269–275, jun 1902.

[21] U. Fano, "The theory of anomalous diffraction gratings and of quasi-stationary waves on metallic surfaces (sommerfeld's waves)," *J. Opt. Soc. Am.*, vol. 31, pp. 213–222, Mar 1941.

[22] A. Hessel and A. A. Oliner, "A new theory of wood's anomalies on optical gratings," *Appl. Opt.*, vol. 4, pp. 1275–1297, Oct 1965.

[23] M. Darvishzadeh-Varcheie, W. J. Thrift, M. Kamandi, R. Ragan, and F. Capolino, "Two-scale structure for giant field enhancement: Combination of rayleigh anomaly and colloidal plasmonic resonance," *Phys. Rev. Applied*, vol. 11, p. 054057, May 2019.

[24] R. Kretschmer and W. Fritzsche, "Pearl chain formation of nanoparticles in microelectrode gaps by dielectrophoresis," *Langmuir*, vol. 20, no. 26, pp. 11797–11801, 2004. PMID: 15595813.

[25] B. C. Gierhart, D. G. Howitt, S. J. Chen, R. L. Smith, and S. D. Collins, "Frequency dependence of gold nanoparticle superassembly by dielectrophoresis," *Langmuir*, vol. 23, no. 24, pp. 12450–12456, 2007. PMID: 17963407.

[26] J. Lee, S. Mubeen, C. M. Hangarter, A. Mulchandani, W. Chen, and N. V. Myung, "Selective and rapid room temperature detection of h2s using gold nanoparticle chain arrays," *Electroanalysis*, vol. 23, no. 11, pp. 2623–2628, 2011.

[27] S. Enoch and N. Bonod, *Plasmonics, From Basics to Advanced Topics*. Springer-Verlag Berlin Heidelberg, 2012.

[28] G. M. Hale and M. R. Querry, "Optical constants of water in the 200-nm to 200-μm wavelength region," *Appl. Opt.*, vol. 12, pp. 555–563, Mar 1973.

[29] E. D. Palik, ed., *Handbook of Optical Constants of Solids*. Boston: Academic Press, 1998.

[30] S.-Y. Ding, E.-M. You, Z.-Q. Tian, and M. Moskovits, "Electromagnetic theories of surface-enhanced raman spectroscopy," *Chem. Soc. Rev.*, vol. 46, pp. 4042–4076, 2017.

Appendix A

Polarizabilities of a Chiral Spherical Particle

Without loss of generality, we assume a linearly polarized plane wave:

$$\mathbf{E}^{\text{inc}} = E_0\, e^{ikz}\hat{\mathbf{x}}, \mathbf{H}^{\text{inc}} = \frac{E_0}{\eta_0}\, e^{ikz}\hat{\mathbf{y}}, \tag{A.1}$$

illuminating a particle, located at the origin of the coodinate $(0, 0, 0)$, where $E_0$is the complex amplitude of the field, $\eta_0$is the intrinsic impedance of vacuum, and k is the wavenumber. Moreover, $\hat{\mathbf{x}}$and $\hat{\mathbf{y}}$are the unit vectors of Cartesian coordinate system. The induced electric $\mathbf{p}$ and magnetic $\mathbf{m}$ dipole moments in the particle reads

$$\begin{aligned} \mathbf{p} = \alpha_{\text{ee}}\mathbf{E}^{\text{inc}} + \alpha_{\text{em}}\mathbf{H}^{\text{inc}} &= E_0 \left(\alpha_{\text{ee}}\hat{\mathbf{x}} + \tfrac{\alpha_{\mathbf{em}}}{\eta_0}\hat{\mathbf{y}}\right) \\ \mathbf{m} = \alpha_{\text{mm}}\mathbf{H}^{\text{inc}} + \alpha_{\text{me}}\mathbf{E}^{\text{inc}} &= E_0 \left(\alpha_{\text{me}}\hat{\mathbf{x}} + \tfrac{\alpha_{\mathbf{mm}}}{\eta_0}\hat{\mathbf{y}}\right). \end{aligned} \tag{A.2}$$

where $\alpha_{\rm ee}$, $\alpha_{\rm em}$, $\alpha_{\rm mm}$, and $\alpha_{\rm me}$are, respectively, the electric, electromagnetic, magnetic, and magnetoelectric polarizabilities of the particle. The scattered electric field by the particle reads

$$\begin{aligned}\mathbf{E}^{\rm sca} &= \Big((\hat{\mathbf{r}}\times\mathbf{p})\times\hat{\mathbf{r}} - \tfrac{1}{c_0}\hat{\mathbf{r}}\times\mathbf{m}\Big)\tfrac{k^2 e^{ikr}}{4\pi\epsilon_0 r}\\ E_0\tfrac{k^2\,e^{ikr}}{4\pi\epsilon_0 r}\Bigg\{&\alpha_{\rm ee}\left(\cos\theta\cos\phi\hat{\theta}-\sin\phi\hat{\phi}\right)-\epsilon_0\alpha_{\rm mm}\left(\cos\theta\sin\phi\hat{\phi}-\cos\phi\hat{\theta}\right)\\ &+\tfrac{\alpha_{\rm em}}{\eta_0}\left(\cos\theta\sin\phi\hat{\theta}+\cos\phi\hat{\phi}\right)-\tfrac{\alpha_{\rm me}}{c_0}\left(\cos\theta\cos\phi\hat{\phi}+\sin\phi\hat{\theta}\right)\Bigg\}.\end{aligned} \tag{A.3}$$

in the spherical Coordinate system (r,θ,φ). The scattered field of a small particle may also be expressed as [1]

$$\mathbf{E}^{\rm sca} = \frac{3}{2}iE_0\left[a_1\mathbf{M}_{\rm o1} - ib_1\mathbf{N}_{\rm e1} + c_1\mathbf{M}_{\rm e1} - id_1\mathbf{N}_{\rm o1}\right], \tag{A.4}$$

where [2]

$$\begin{aligned}\mathbf{M}_{\rm o1} &= \left(-\cos\theta\sin\phi\hat{\phi}+\cos\phi\hat{\theta}\right)h^{(1)}(\rho)\\ \mathbf{M}_{\rm e1} &= \left(-\cos\theta\cos\phi\hat{\phi}-\sin\phi\hat{\theta}\right)h^{(1)}(\rho)\\ \mathbf{N}_{\rm e1} &= \left(\cos\theta\cos\phi\hat{\theta}-\sin\phi\hat{\phi}\right)\tfrac{1}{\rho}\tfrac{d\left(\rho h^{(1)}(\rho)\right)}{d\rho}\\ \mathbf{N}_{\rm o1} &= \left(\cos\theta\sin\phi\hat{\theta}+\cos\phi\hat{\phi}\right)\tfrac{1}{\rho}\tfrac{d\left(\rho h^{(1)}(\rho)\right)}{d\rho},\end{aligned} \tag{A.5}$$

where $\rho = kr$ and $h^{(1)}$is the spherical hankel function of the first kind and first order. Considering that

$$\begin{array}{c} h^{(1)}(\rho) \sim \frac{-e^{i\rho}}{\rho} \\ \frac{1}{\rho}\frac{d\left(\rho h^{(1)}(\rho)\right)}{d\rho} \sim \frac{-ie^{i\rho}}{\rho} \end{array} \tag{A.6}$$

for large ρ, we have:

$$\begin{aligned} \mathbf{M}_{\mathrm{o1}} &\sim \left(-\cos\theta\sin\phi\hat{\phi} + \cos\phi\hat{\theta}\right)\frac{-e^{i\rho}}{\rho} \\ \mathbf{M}_{\mathrm{e1}} &\sim \left(-\cos\theta\cos\phi\hat{\phi} - \sin\phi\hat{\theta}\right)\frac{-e^{i\rho}}{\rho} \\ \mathbf{N}_{\mathrm{e1}} &\sim \left(\cos\theta\cos\phi\hat{\theta} - \sin\phi\hat{\phi}\right)\frac{-ie^{i\rho}}{\rho} \\ \mathbf{N}_{\mathrm{o1}} &\sim \left(\cos\theta\sin\phi\hat{\theta} + \cos\phi\hat{\phi}\right)\frac{-ie^{i\rho}}{\rho}, \end{aligned} \tag{A.7}$$

and therefore, scattered field reads

$$\begin{aligned} \mathbf{E}^{\mathrm{sca}} \sim \frac{3}{2}iE_0\frac{e^{ikr}}{kr}\Bigg\{ & a_1\left(-\cos\theta\sin\phi\hat{\phi} + \cos\phi\hat{\theta}\right) + \\ & -b_1\left(\cos\theta\cos\phi\hat{\theta} - \sin\phi\hat{\phi}\right) + \\ & +c_1\left(-\cos\theta\cos\phi\hat{\phi} - \sin\phi\hat{\theta}\right) + \\ & +d_1\left(\cos\theta\sin\phi\hat{\theta} + \cos\phi\hat{\phi}\right)\Bigg\}. \end{aligned} \tag{A.8}$$

Comparing Eqs. A.3 and A.8 leads to

$$\begin{aligned}
\alpha_{\mathrm{ee}} &= -\frac{\frac{3}{2}iE_0\frac{e^{ikr}}{kr}}{E_0\frac{k^2e^{ikr}}{4\pi\epsilon_0 r}}b_1 = -\frac{6\pi i\epsilon_0}{k^3}b_1 \\
\alpha_{\mathrm{mm}} &= \frac{\frac{3}{2}iE_0\frac{e^{ikr}}{kr}}{E_0\frac{k^2e^{ikr}}{4\pi\epsilon_0 r}}\frac{a_1}{-\epsilon_0} = -\frac{6\pi i\epsilon_0}{k^3}\frac{a_1}{\epsilon_0} = -\frac{6\pi i}{k^3}a_1 \\
\alpha_{\mathrm{me}} &= \frac{\frac{3}{2}iE_0\frac{e^{ikr}}{kr}}{E_0\frac{k^2e^{ikr}}{4\pi\epsilon_0 r}}\frac{c_1}{-\frac{1}{c_0}} = \frac{6\pi i\epsilon_0}{k^3}\left(-c_0c_1\right) = -\frac{6\pi i}{k^3}\frac{1}{\eta_0}c_1 \\
\alpha_{\mathrm{em}} &= \frac{\frac{3}{2}iE_0\frac{e^{ikr}}{kr}}{E_0\frac{k^2e^{ikr}}{4\pi\epsilon_0 r}}\frac{-id_1}{\frac{1}{\eta_0}} = \frac{6\pi i\epsilon_0}{k^3}\left(-\eta_0 d_1\right) = \frac{-6\pi i}{k^3}\frac{1}{c_0}d_1,
\end{aligned} \tag{A.9}$$

where the coefficients a_1, b_1, c_1,and $d_1$are defined in Bohren's thesis pages 14-16 [1].

Appendix B

Field Enhancement in an Array of Plasmonic Rods

In this study, we use CST Studio suite Finite Elemenet analysis to analyze the electric field enhancement when an array of plasmonic rods is excited by a normally incident plane wave propagating along the $-z$ direction. The unit cell of the structure is modeled as a rectangular waveguide with its walls being at planes $x = \pm L_y$ and $y = \pm L_y/2$, which are, respectively, modeled as perfect electric and perfect magnetic boundary conditions. The dominant mode of this waveguide is the TEM mode with its electric and magnetic fields, respectively, polarized along y and x directions. Two waveports are used at planes $z = \pm 1000$nm to excite the structure by the dominant TEM mode. This setup is devised to overcome the difficulties in simulation of Rayleigh anomaly where grazing diffraction orders which are not absorbed by the Floquet ports are present in the structure. The field enhancement for the design parameters $W = 50, 100, 150$nm, $H = 100, 150, 200$nm, and $L_y = 500, 525, 550, 575, 600$nm is calculated at the probe point P_8 and is averaged over the wavelength range $780 - 850$nm is illustrated in the figure below.

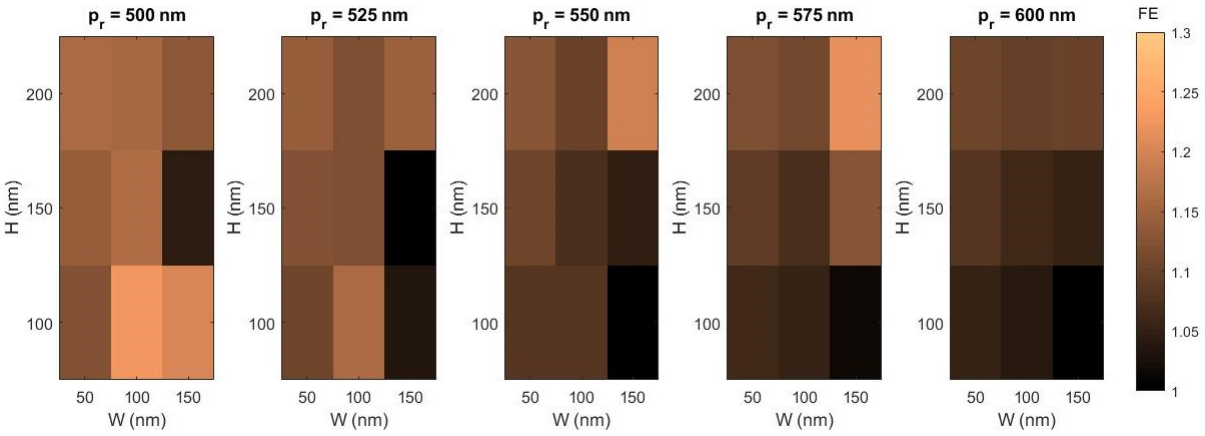

Figure B.1: The field enhancement for various values of design parameters W (nm), H (nm), and L_y (nm) calculated at the probe point P_8 and averaged over the wavelength range from 780 to 850 nm.

Bibliography

[1] C. F. Bohren. *Light Scattering by Optically Active Particles.* PhD thesis, THE UNIVERSITY OF ARIZONA., Aug. 1975.

[2] C. F. Bohren and D. R. Huffman. *Absorption and Scattering of Light by Small Particles.* 1998.